Nanopore-based sensors for DNA sequencing

a review

Wei, Jiangtao; Hong, Hao; Wang, Xing; Lei, Xin; Ye, Minjie; Liu, Zewen

DOI
10.1039/d4nr01325e

Publication date
2024

Document Version
Final published version

Published in
Nanoscale

Nanoscale

REVIEW

View Article Online
View Journal

Cite this: DOI: 10.1039/d4nr01325e

Nanopore-based sensors for DNA sequencing: a review

Jiangtao Wei, [a] Hao Hong,[a,b] Xing Wang,[a] Xin Lei,[c] Minjie Ye[d] and Zewen Liu*[a]

Nanopore sensors, owing to their distinctive structural properties, can be used to detect biomolecular translocation events. These sensors operate by monitoring variations in electric current amplitude and duration, thereby enabling the calibration and distinction of various biomolecules. As a result, nanopores emerge as a potentially powerful tool in the field of deoxyribonucleic acid (DNA) sequencing. However, the interplay between testing bandwidth and noise often leads to the loss of part of the critical translocation signals, presenting a substantial challenge for the precise measurement of biomolecules. In this context, innovative detection mechanisms have been developed, including optical detection, tunneling current detection, and nanopore field-effect transistor (FET) detection. These novel detection methods are based on but beyond traditional nanopore techniques and each of them has unique advantages. Notably, nanopore FET sensors stand out for their high signal-to-noise ratio (SNR) and high bandwidth measurement capabilities, overcoming the limitations typically associated with traditional solid-state nanopore (SSN) technologies and thus paving the way for new avenues to biomolecule detection. This review begins by elucidating the fundamental detection principles, development history, applications, and fabrication methods for traditional SSNs. It then introduces three novel detection mechanisms, with a particular emphasis on nanopore FET detection. Finally, a comprehensive analysis of the advantages and challenges associated with both SSNs and nanopore FET sensors is performed, and then insights into the future development trajectories for nanopore FET sensors in DNA sequencing are provided. This review has two main purposes: firstly, to provide researchers with a preliminary understanding of advancements in the nanopore field, and secondly, to offer a comprehensive analysis of the fabrication techniques, transverse current detection principles, challenges, and future development trends in the field of nanopore FET sensors. This comprehensive analysis aims to help give researchers in-depth insights into cutting-edge advancements in the field of nanopore FET sensors.

Received 26th March 2024,
Accepted 7th August 2024

DOI: 10.1039/d4nr01325e

rsc.li/nanoscale

1. Introduction

Since 1949, when nanopores were first used to count red blood cells,[1] nanopore detection technology has received considerable attention.[2–18] From its initial use in single molecule counting, the technology has expanded towards a wide range of applications in various fields including physics, biomolecule detection (such as proteins, viruses, DNA, insulin, *etc.*), water purification, power generation, data storage, and inter-discipline application.[19–23] Over the past 20 years, SSNs have undergone significant changes with respect to several aspects, including fabrication materials,[24–31] methods,[32–38] detection principles,[39–42] and applications.[43–52] Nanopore technology is experiencing rapid developments. Nanopore sensors, due to their unique structures, can serve as a powerful sensing platform. During the experimental process, the membrane with a nanopore divides the solution into two compartments, with the nanopore acting as the only passage. Under an applied voltage, the translocation of biomolecules inside the nanopore can be monitored in real-time by observing changes to the ionic current of the nanopore system.[53–56] Small changes can lead to a large current modulation in the nanopore system. The recorded ionic current includes information about the duration and amplitude of current changes during translocation events, enabling the distinction of various translocating molecules, achieving single entity sensitivity.[57–63]

Nanopores could potentially be used to perform single-molecule DNA sequencing at low-cost with high throughput.[64–66] Nanopore sequencing has the advantage of requiring no amplification during sample preparation and enables direct detection,[67] which can further facilitate the per-

[a]*School of Integrated Circuits, Tsinghua University, Beijing 100084, China. E-mail: liuzw@tsinghua.edu.cn*
[b]*Department of Microelectronics, Delft University of Technology, 2628 CD Delft, The Netherlands*
[c]*School of Chemistry, Beihang University, Beijing, 100084, China*
[d]*Department of Engineering Physics, Tsinghua University, Beijing 100084, China*

sonalization of DNA sequencing. Currently, only protein nanopores have been successful for DNA sequencing.[68,69] However, protein nanopores are quite sensitive to external environmental factors, such as temperature, applied bias, pH, solution concentration, *etc.*, due to the lipid bilayer. These factors severely restrict the large-scale and widespread application of biological nanopores. However, SSNs can overcome these extreme factors and be reused, so ample attention is paid to SSNs. Researchers believe that SSNs could eventually be used to achieve DNA sequencing. Unluckily, at present, DNA sequencing using SSNs still faces huge challenges, such as fast translocation speeds, poor repeatability, and low signal-to-noise ratios (SNRs).[70–74] To achieve DNA sequencing based on SSNs, researchers have made innovations in terms of new materials and new detection mechanisms.[75–82] Currently, the main principles of SSN testing include traditional ionic current blockade detection, tunneling current detection, optoelectronic sensing detection, transverse current detection (combination of nanopores and FET sensors).

Here, we begin with a brief introduction to the basic detection principles, historical development, applications, and fabrication methods for traditional SSNs. Then, we separately introduce new detection mechanisms. After that, we provide a detailed overview of the development of nanopore FET sensors and the challenges faced in experiments and tests. Finally, we discuss the merits and issues associated with SSNs and nanopore FET sensors, and the future development directions for nanopore FET sensors in DNA sequencing. The purpose of this review is to provide comprehensive coverage of traditional SSNs and FET nanopore sensors. Some representative examples have been selected that highlight the incredible progress made in SSNs and nanopore FET sensors. We believe this review can provide some assistance and insights for researchers interested in the field of nanopores.

2. Traditional solid-state nanopores

2.1 The development of solid-state nanopores

In 1949, Wallace H. Coulter discovered a new method to count red blood cells suspended in a fluid medium. Then Coulter patented his counting method in 1953,[2,3] later named resistive pulse sensing. After that, nanopore sensor platforms have been extensively developed and attracted wide attention in various domains,[49,52,83–93] mainly because researchers have found ways to reduce the orifice size from millimeters and micrometers to nanometers.[24,32,33,35,38,94–100] In 1996, Kasianowicz *et al.* showed the first DNA translocation experiments through a biological nanopore, and the sensing device was prepared through the insertion of the natural α-hemolysin protein pore into the phospholipid bilayer.[101] Since the first use, biological protein nanopores have attracted more and more attention in the field of biomolecular detection.[102,103] As natural proteins, biological nanopores have short and narrow channels, intrinsic reproducibility in terms of geometry, low noise and a high SNR, and can be applied to high-bandwidth testing and DNA sequencing. However, due to poor mechanical stability, limited pore sizes, and sensitivity to external testing environments (such as voltage, pH conditions, temperature, extreme salt concentrations), these factors severely restrict the widespread application and mass production of biological nanopores.[103–105]

SSNs show excellent stability under non-physiological conditions and can be mass produced,[106] therefore, SSNs are a remarkable alternative for overcoming some shortcomings of biological nanopores. Especially, SSNs can also be integrated into devices based on advanced micro- and nanofabrication techniques, therefore more attention has been paid to SSNs. With the continuous development and maturation of semiconductor processing technology, researchers are able to fabricate controllable SSNs through different methods, including sizes, shapes, and surface properties.[107–115] In 2001, the first SSN down to 5 nm in diameter was successfully fabricated by Li *et al.* using ion-beam sculpting of a suspended silicon nitride (SiN_x) membrane, allowing the detection of DNA;[94] this research initiated the non-biological nanopore field. Afterward, a variety of fabrication methods were developed for SSNs, such as a focused ion/electron beam (FI/EB),[64] chemical etching,[38] dielectric breakdown,[98] a focused laser beam,[99] atomic force microscopy (AFM),[37] electron beam lithography (EBL),[100] scanning transmission electron microscopy (S/TEM),[116] ion current feedback chemical etching,[117] laser pulling,[118] imprint lithography,[119] and single swift heavy ions.[25] Meanwhile, the membrane materials have also been greatly expanded. In 2023, Liyuan Liang *et al.* made a detailed classification,[53] for example, organic/inorganic materials, metallic/metal oxide materials and hybrid materials. The organic materials encompass a diverse range, including polymers, chemically synthesized barrel-shaped molecules, covalent organic frameworks (COFs) and helical self-assembled molecules.[120,121] The inorganic materials are more abundant and varied. Typical examples are silicon-based materials (Si, SiN_x, SiO_2 and SiC), two-dimensional (2D) materials (MoS_2, WS_2, SnS_2, h-BN, graphene, silicene, phosphorene, graphene, graphyne, diamond, carbon film, carbon nanotubes, graphene/h-BN heterostructure, borophene, C_3N_4),[29,122–124] metal-based materials (Au, Ag, Al_2O_3, HfO_2, TiO_2, ZnO, MOFs, MXenes) as well as hybrid materials. Rapid and low-cost DNA sequencing is the main driving force for the field of nanopores, leading to the continuous advancement of the nanopore field.

2.2 The detection principle and applications of solid-state nanopores

SSNs have undergone vigorous development due to the continuous maturation of semiconductor processing technology. SSNs are man-made, nano-sized openings in membranes separating two chambers containing an electrolyte solution (*cis*- and *trans*-side); one of the chambers contains biomolecules to be detected, as shown in Fig. 1 (left panel). When an electric field is applied across the membrane through a pair of non-polarizable electrodes (Ag/AgCl electrode) on each side, the

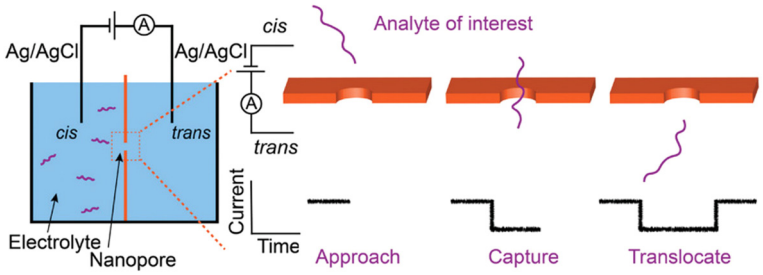

Fig. 1 Schematic of a nanopore sensor mechanism and ionic current trace detection. Reprinted with permission from ref. 127. Copyright 2022, Royal Society of Chemistry.

nanopore provides the only channel for mobile ions and biomolecules to pass from one chamber to the other. Before the analyte enters the nanopore, a constant ionic current is recorded through the nanopore, which is usually named the open pore current. The trace of the open pore ion current is highly dependent on the pore size, pore shape, membrane thickness, and surface charge. Combining everything described above yields the following equation for the total conductance through a nanopore:[125]

$$G = k_b\left[\frac{4l}{\pi d^2} + \frac{1}{1+4\frac{l_{Du}}{d}} + \frac{2}{\alpha d + \beta l_{Du}}\right]^{-1} \quad (1)$$

Here, k_b is the bulk conductivity of the electrolyte, l_{Du} is the Dukhin length and α, β are geometrical factors (usually defined as $\alpha = \beta = 2$). The Dukhin length, l_{Du}, is defined as the ratio of surface conductance to bulk conductance, *i.e.* $l_{Du} = \frac{k_s}{k_b}$, which denotes the relative importance of surface conduction compared to bulk conduction. When the analytes diffused near the nanopore, they were captured by the nanopore due to electrophoretic and electroosmotic effects,[126] then analyte molecules began to translocate. When analytes are driven to thread through the nanopore, a transient change in conductivity will happen, due to a partial blockage of the nanopore by the analyte, and when the analyte translocation process ends, the ionic current returns to its original level; this phenomenon is completely reflected in the current trace, as shown in Fig. 1 (right panel).[127] The recorded resistive pulse spikes by the patch clamp amplifiers are associated with the geometry, charge status, polarity and dipole of the analytes.[53] The thickness-to-diameter aspect ratio, geometry, and surface charges of the SSN can significantly influence the experimental performance, including the capture efficiency of analytes by the pore and the duration and signal-to-noise ratio (SNR) of translocation events. According to the detection mechanism for a nanopore resistance pulse, when the nanopore's size is only slightly larger than the analyte molecule, the most significant change in conductance for translocation of an analyte will be obtained.[66]

Nanopores have been applied to various fields since they were discovered, from initial biological nanopore sequencing, to artificially prepared SSNs for electro-osmotic trap devices,[83] nanoparticle synthesis,[128] proteins,[129] gene synthesis reactions,[130] single-molecule thermoscopy,[131] ion screening,[132] ionic-current rectification,[133] single nucleotide mutation detection,[84] Au nanoparticle recognition,[134] ionic memcapacitive effects,[135] memory,[136] gas mixture separation,[137] high power density generators,[51] water desalination,[138] synapses,[92] nanopore rotary motors,[49] data storage,[139] *etc*. Fig. 2 shows the applications of SSNs in various fields. Of course, the ultimate goal of SSNs is to achieve DNA sequencing quickly and cheaply for personal use, and a lot of effort has been made to achieve this goal, such as the diversification of nanopore detection principles,[121] the continuous innovation of nanopore preparation methods,[122] the surface modification of nanopores,[140] new-materials-based nanopores,[141] and hybrid nanopores.[142] Although SSNs are applied to various fields and have experienced a boom in development, a considerable portion of studies are still based on single nanopores, which are not conducive to multiplexed detection by nanopores.[143–147]

2.3 The fabrication of solid-state nanopores

The most important element of a nanopore sensor is the nanoscale pore. To resolve interesting molecular structures precisely, the nanopore dimensions must be small enough to avoid averaging over continuous single-molecule configurations induced by thermal fluctuations and large enough to pass the smallest dimensions of the molecule to be detected, so intense attention is paid to the preparation of nanopores. Since 2001, the fabrication methods for nanopores, the shape of the nanopore, the surface properties of the nanopore and the reproducibility of nanopores have been sufficiently investigated and developed. To date, SSNs can be made by various methods, including ion- and electron-beam sculpting methods,[94] the track-etching technique,[148] transmission electron microscope drilling,[33] laser-assisted pulling,[118] ionic current-monitored wet etching,[106] controlled dielectric breakdown,[149] electrochemical reactions,[150] and EBL.[151] The sizes and geometries of nanopores prepared by different methods are varied, which is an unavoidable fact in the preparation of SSNs. Compared with biological nanopores, the pore sizes of SSNs cannot be as precisely engineered as biological nanopores, or as reproducibly, so more efforts need to be made in future. Fig. 3 shows schematics of typical pore morphologies of SSNs.

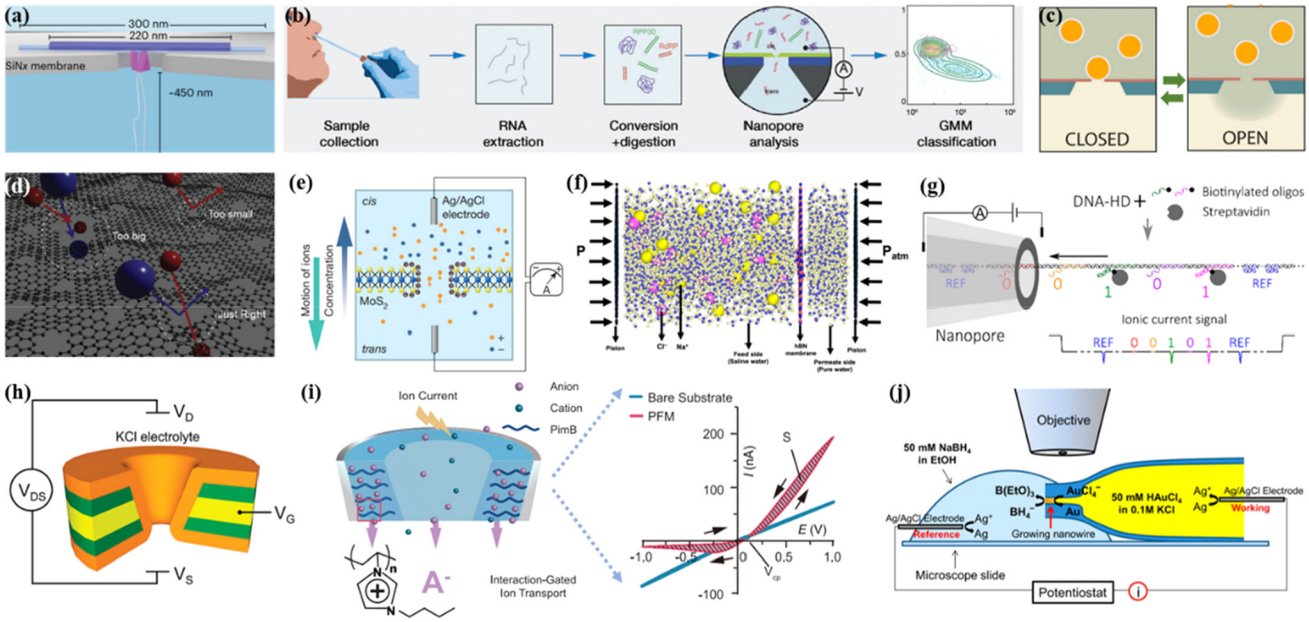

Fig. 2 Applications of solid state nanopores in various fields. (a) DNA turbine. Reprinted with permission from ref. 143. Copyright 2023, Springer Nature. (b) Label-free quantification of SARS-CoV-2 RNA. Reprinted with permission from ref. 89. Copyright 2022, Royal Society of Chemistry. (c) Volatile or nonvolatile memory. Reprinted with permission from ref. 136. Copyright 2022, National Academy of Sciences. (d) Gas separation. Reprinted with permission from ref. 27. Copyright 2022, American Chemical Society. (e) Nano-power generators. Reprinted with permission from ref. 144. Copyright 2016, Nature Research. (f) Water desalination. Reprinted with permission from ref. 138. Copyright 2022, American Chemical Society. (g) Data storage. Reprinted with permission from ref. 139. Copyright 2020, American Chemical Society. (h) Ionic FET. Reprinted with permission from ref. 145. Copyright 2009, American Chemical Society. (i) Fluidic memristor. Reprinted with permission from ref. 146. Copyright 2023, American Association for the Advancement of Science. (j) Single metal nanowire growth. Reprinted with permission from ref. 147. Copyright 2015, American Chemical Society.

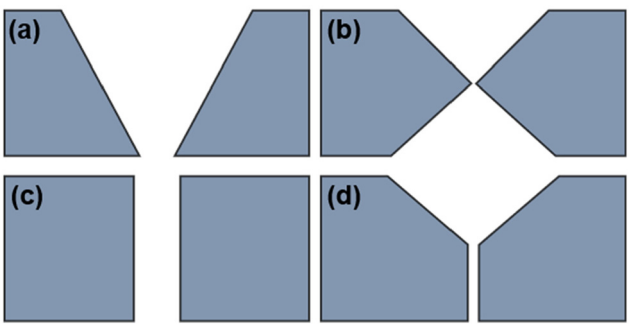

Fig. 3 Typical morphologies of solid-state nanopores (cross-sectional view). (a) Conical nanopore. (b) Biconical nanopore. (c) Cylindrical nanopore. (d) Funnel-shaped nanopore. Commonly, the diameters of pores range from sub-nanometers to a few hundreds of nanometers. The thickness of the membrane lies in the range of sub-10 nm to a few tens of micrometers.

As described above, nanopores can be fabricated by various methods, as shown in Fig. 4. Fig. 4(a) shows the preparation of a nanopore by ion-and electron-beam sculpting methods, which can accurately control the position, size and geometry of the nanopore. Utilizing this approach, nanopores with diameters less than 1 nm can be successfully fabricated with a degree of repeatability. Furthermore, nanopore preparation can be conducted on a variety of materials, such as SiO_2 membrane, SiN_x membrane, metal membrane, two-dimensional material membrane, and so on. However, this approach requires expensive instruments, is high cost, with low fabrication efficiency, and cannot be used for large-scale preparation.[152] The EBL method shares similarities with the above approaches and is also capable of fabricating nanopores on various membrane materials with relatively good repeatability. However, this method suffers from low fabrication efficiency, requires expensive equipment, and the minimum pore size achievable is heavily dependent on the equipment, so it has certain limitations.[153] In addition, these tools are not accessible to many research groups and are poorly suited for mass production. Alternatively, laser-assisted pulling of quartz capillaries is more efficient and less expensive than ion- and electron-beam drilling of a solid-state membrane,[154] as shown in Fig. 4(b). Quartz nanopipettes can be fabricated by the laser-assisted pulling method easily, which only needs two steps: the laser beam locally heats the material and it is pulled. Moreover, two identical nanopipettes can be obtained by this method in one experiment, which is reproducible to a certain extent. However, the materials used for fabricating nanopipettes are relatively limited; this restricts the further development of this method. The controlled electrical breakdown method shown in Fig. 4(c) is a fast and simple way to fabricate a single nanopore, which mainly relies on local electrical breakdown at the scale of nanometers in solution. By applying

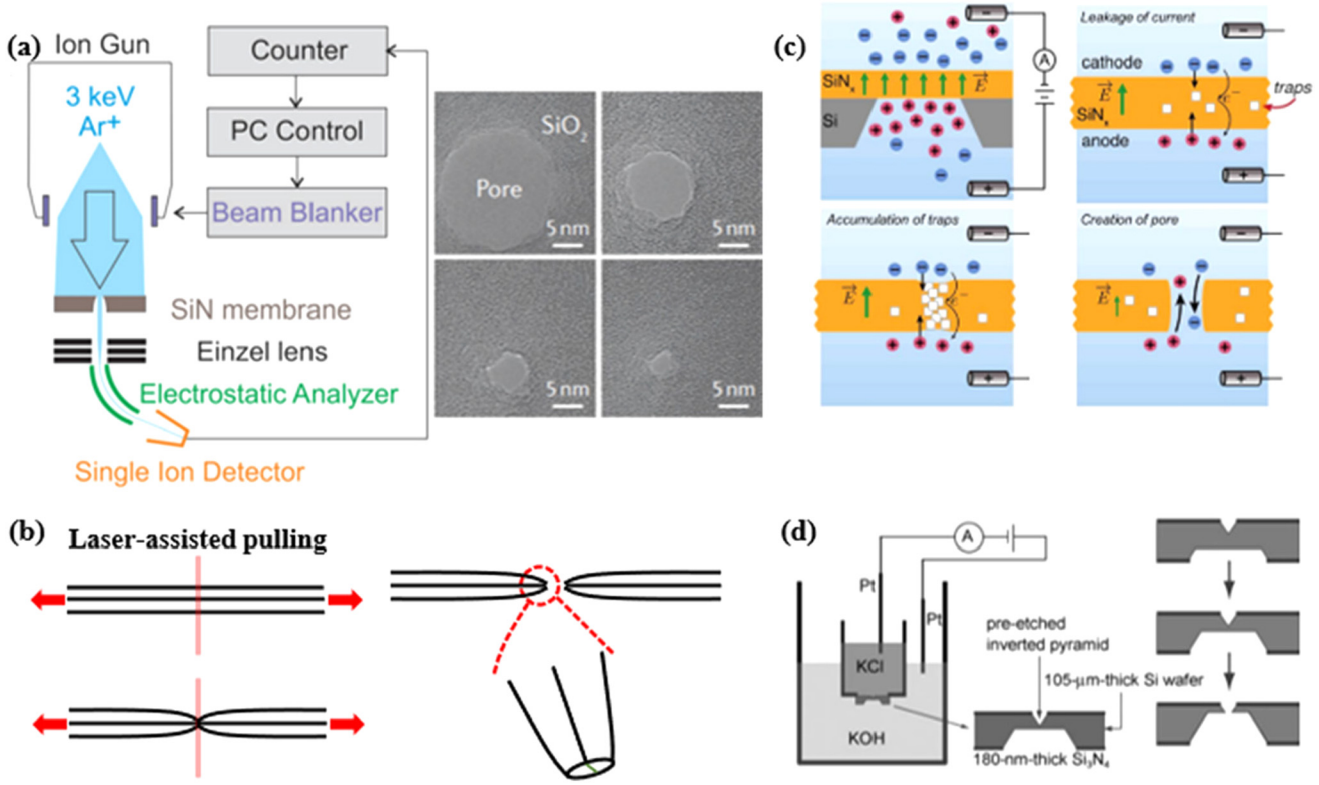

Fig. 4 Different methods for fabricating nanopores. (a) Schematic of an ion sculpting system (left). TEM images show nanopore formation in silicon dioxide using an electron beam; the size of the nanopore gradually decreases to about 3 nm under electron irradiation (right). Reprinted with permission from ref. 66. Copyright 2020, Springer Nature. Reprinted with permission from ref. 152. Copyright 2012, AIP Publishing. (b) Nanopores were prepared by laser-assisted pulling. (c) Entire process of nanopore formation by dielectric breakdown. Firstly, the transmembrane voltage forms an electric field inside SiN_x, then the leakage current of the film is formed through the trap-assisted tunneling mechanism; after that, the accumulation of charge traps leads to a highly localized conductive path and a discrete dielectric breakdown event. Finally, the defects are removed to form nanopores. Reprinted with permission from ref. 35. Copyright 2014, Public Library Science. (d) Fabrication of silicon nanopores with feedback electrochemical etching. Schematic of the experimental setup (left). Over time, Si on the back is continuously etched until the nanopore is formed. By controlling the amplitude of the monitoring current, nanopores of different sizes can be obtained. Reprinted with permission from ref. 117. Copyright 2007, Wiley-VCH.

a voltage across an insulating membrane to generate a high electric field, while recording the transmembrane current, by controlling the magnitude of the current, we can monitor the formation of nanopores in real time and precisely control their diameters. In this way, a single nanopore down to 1 nm in size with sub-nm precision can be fabricated at low cost and on a large scale. At present, the controlled electrical breakdown method already has the corresponding products, and can be purchased in the market. This method avoids the need for costly equipment and a complex preparation process, has universal applicability, and provides a convenient path towards the manufacture of nanopore-based biotechnologies.[109]

In addition to the physical electrical breakdown mentioned above, solution based nanopore preparation methods also include chemical etching. During the fabrication process, the membrane material undergoes a chemical reaction with the solution, and nanopores with expected diameters and shapes can be easily and affordably obtained.[38] For example, conically shaped nanopores with an effective diameter down to ~2 nm can be prepared by ion tracking and chemical etching. This method mainly includes two steps: high energy ion implantation (total kinetic energy of several hundred MeV to several GeV) and preferential chemical etching of the ion track.[148] Specifically, by regulating the chemical etching process, various geometries can be obtained including hourglass, funnel, and dumbbell. This method needs high-energy ion implantation and is therefore more expensive than physical electrical breakdown. In addition, the preparation materials are based on polymers, mainly including polyethylene terephthalate (PET), polycarbonate (PC), polyimide (PI), polyvinylidene fluoride (PVDF), and polypropylene (PP). The thickness of the prepared nanopore is from 5 μm to 50 μm, depending on the energy of the fast heavy ions and the type of polymer used,[155] so this method has certain limitations.

The track-etching technique described above cannot be monitored in real-time, in order to further understand the formation process of nanopores and achieve finer control of the sizes of nanopores. In 2007, the feedback chemical etching method was proposed by Park *et al.* This method takes advantage of the well-known anisotropic etching behavior of silicon

in alkaline solutions, so nanoscale pores are accessible in this way, as shown in Fig. 4(d).[117] During the preparation process, the formation of nanopores can be monitored in real time by detecting the transmembrane current. Theoretically, nanopores of any diameter can be obtained by controlling the opening current. However, when the nanopore opens, the transmembrane current is only at the picoampere (pA) level. The signal of this opening current is easily overshadowed by noise, preventing timely cessation of the process. So, the theoretical limit of the nanopore size being less than 1 nm cannot be obtained presently. Nowadays, the smallest pore size achievable on silicon material with this method is approximately 3 nm, and this can only be achieved in one dimension.[106] This method is cheap, easy and enables large-scale preparation, but the materials suitable for nanopore fabrication are subject to strict limitations (silicon). Each of the fabrication methods described above has merits and disadvantages. Research groups can select appropriate nanopore fabrication methods based on the conditions of their laboratories. Conducting more in-depth research on nanopores, aiming to advance SSNs towards the ultimate goal of DNA sequencing in a fast and low-cost manner.

As previously mentioned, over the past 20 years, SSNs have undergone rapid development in terms of both materials and fabrication methods. Table 1 provides a detailed summary of the advancements in SSNs, covering six aspects: methods, materials, shapes, sizes, costs, and the feasibility of large-scale production.

3. Built on but beyond ionic sensing

After more than 20 years of development, SSNs have played an important role in many fields, such as energy, chemistry, gas molecular screening, protein detection, micro-turbines *etc*. At the moment, biological nanopores have been successfully used for DNA sequencing due to their special structures,[104] but DNA sequencing with SSNs has not yet been achieved, as several challenges remain to be overcome, as shown below:

(1) Control of the translocation speed of DNA molecules: DNA molecules are too fast for the translocation process, resulting in the loss of some effective signals, although there are other methods to reduce the translocation speed, but this is contrary to the goal of rapid DNA sequencing; the DNA strand that threads through the pore moves back-and-forth in the nanopore, which will wash out any possible signals associated with the sequence.

(2) Noise: the SNR of traditional SSNs is too low to carry out high-bandwidth tests, and the translocation signal is obscured by noise.[163] In detail, when DNA molecules translocate through the nanopore, the translocation signal is ~pA in magnitude; it is very difficult to record very small (~pA) ionic currents at a bandwidth consistent with fast translocation speeds.

(3) Poor repeatability of SSNs: it is impossible to fabricate two SSNs that are atomically identical even under the same conditions, so it is very hard to reproduce experimental results exactly. Thus, DNA sequencing currents cannot be accurately calibrated since every nanopore device might have slightly different values.

As detailed before, SSNs still cannot be used to achieve DNA sequencing due to high translocation speeds, low SNR and poor reproducibility. In addition, it is very hard to record ionic current from an individual nanopore in a highly parallel multiplexed nanopore array, because it is not possible to address the nanopores where translocation events occur. At present, most experiments with SSNs are still based on single nanopores. To solve the problems faced by SSNs, many innovative detection methods have been proposed, which mainly rely on the combination of ion sensing and new sensing mechanisms.

As it is well known, nanopores can deliver detection molecules to a special location due to the electric field concentrated in the nanopores' vicinity. Once the detection molecules are brought to the special location, a new principle, rather than nanopore-based ion sensing, is used to complete detection; throughout the whole process, the nanopore only plays a transmitting role. In the ionic current blocking experiment, the test solution system between each nanopore must be separated to avoid averaging the signal over all nanopores present, which increases the difficulty of parallel testing. But, with the new method, it will become easy to achieve highly parallel multiplexed detection; ion-current-independent measurements would enable densely packed sensors with nanopores to work in parallel in a single detecting system. Furthermore, integrating an electrical sensor into the membrane itself could overcome the resolution problem due to the access resistance of the nanopore. Because the sensing length of a nanopore in a membrane material does not correspond to the physical thickness of the membrane due to a significant effect of access resistance, leading to the sensing of multiple nucleotides at a time,[164] even with the thickness of the membrane down to 1 nm, sequencing of DNA still cannot be achieved.[165]

So far, the new detection mechanisms mainly include optical detection, tunnel current detection and transverse current detection (nanopore FET). Next, three new mechanisms are introduced, but with a particular focus on nanopore FET detection.

3.1 Optical detection

In a nanopore array, by an optical measurement method, without electrically insulating each nanopore, the ionic current of many nanopores can be read at the same time, as shown in Fig. 5. Basically, there are two different optical approaches: detect the translocation of fluorescently tagged analytes[166] or visualize the ion flow through the nanopore optically. The latter is better, because it does not require any modifications of the analytes; this method originates from optical patch-clamping. The main theory is that Ca^{2+} sensitive dyes are added to the experimental buffer, and then by using total internal reflection fluorescence (TIRF) microscopy to obtain simultaneous and independent recordings from numerous ion channels *via* imaging of single-channel Ca^{2+} flux, the number of photons emitted by the dyes is proportional to the ionic

Table 1 Development of traditional solid-state nanopores over the past 20 years

Methods	Materials	Types of nanopores	Diameter (nm)	Scale preparation	Applications	Cost
Ion-beam sculpting[94]	Si_3N_4 nanopore	Bowl-shaped cavity	1.8 nm	No	Single DNA molecule detection	High
TEM drilling[95]	Si_3N_4 nanopore	Cylindrical	3 nm	No	DNA folding behavior	High
EBL and wet etching and thermally oxidized[156]	Silicon oxide	Conical	3 nm	Middle	Distinguish the lengths of DNA fragments	High
Laser pulling[97,157]	Glass capillary	Conical	37 nm	Ok	Protein	Middle
EBL and RIE[158]	Si_3N_4/SiO_2 and TiN	Elliptical shape	20 nm	Middle	Control the movement of DNA	Middle
Electro-chemical deposition[96]	Pt		Below 20 nm	Ok	λ-DNA	Low
Controlled dielectric breakdown[35,159]	Silicon nitride	Cylindrical	1 nm	Ok		Low
TEM[160]	Silicon nitride	Cylindrical	4 nm	Middle	Identifying the location of a single protein	High
Solution-phase nanofabrication[161]	Silicon nitride	Cylindrical/double-conical/conical cylindrical/hyperbolic nanopore profiles	6.4 nm/3.1 nm/ 5.5 nm/4.0 nm	Ok		Low
Focused laser beam[162]	Silicon nitride	Hourglass-shaped	6.5 nm	Middle	DNA and protein translocations	Middle
Laser-assisted controlled breakdown[36]	Silicon nitride		~20 nm	Middle	Estimating the approximate molecular shape of IgG proteins	Middle
Atomic force microscope[37]	Silicon nitride		~2.5 nm	Middle	DNA translocation	Middle
Laser-drilling[99]	Silicon nitride	Gaussian-shaped etch profile	~5 nm	Ok	DNA translocation	Middle
Multilevel pulse-voltage injection[108]	Silicon nitride		~1.66 nm	Middle	DNA translocation	High
Feedback controlled laser processing[107]	SiN_x/TiO_2	Gaussian “bowls”	~5 nm	Ok	Translocation analysis of SDS-denatured carbonic anhydrase proteins	Middle
Electron beam lithography[100]	Silicon nitride	Cylindrical	~300 nm	Middle	Conical cylindrical	High
Chemical etching[38]	Silicon nitride		<10 nm	Ok	DNA translocations	Low
Transmission electron microscope[24]	Silicon nitride		~10 nm	Middle	Protein sensing	High
Single swift heavy ions[25]	WO_3 nanosheet		~1.8 nm	Middle		Low

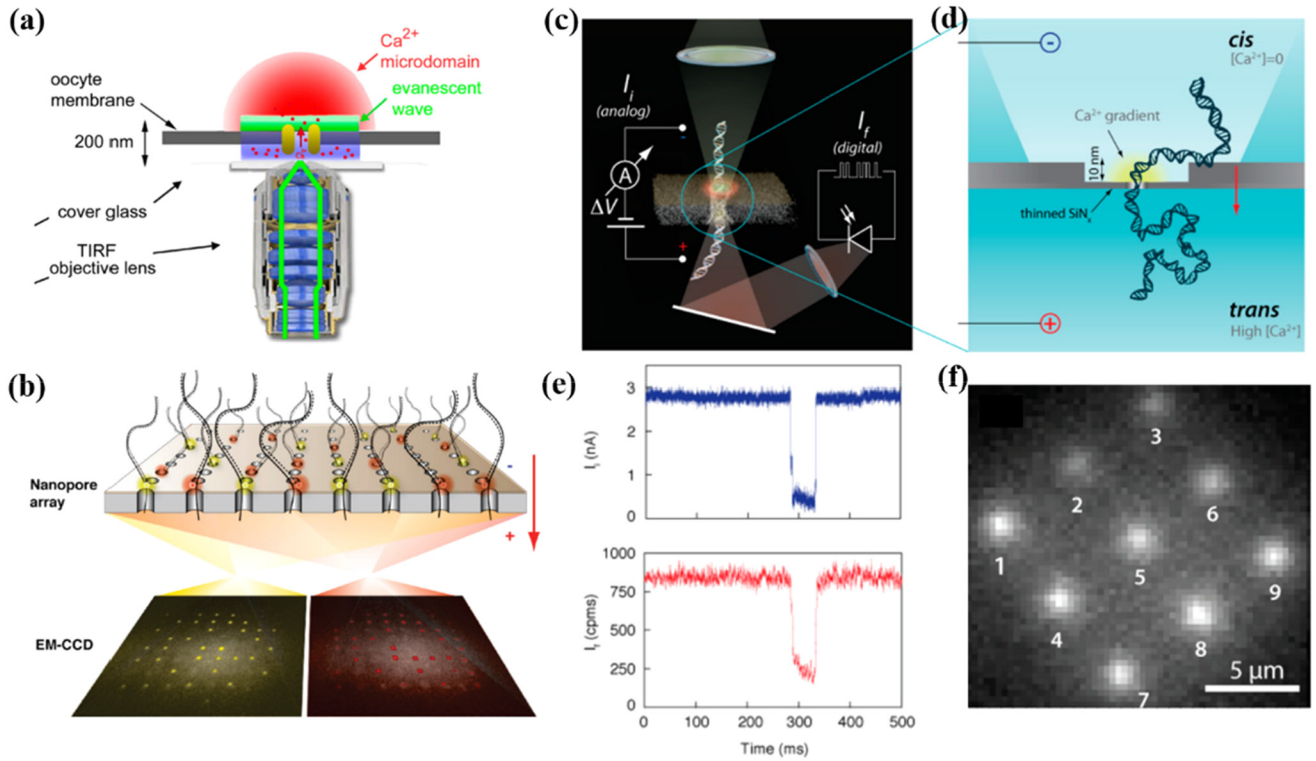

Fig. 5 Detection of molecule translocation by an optical method. (a) Imaging of Ca^{2+} microdomain (red) around a single channel by the evanescent wave (green) formed by the TIRF objective lens. Reprinted with permission from ref. 167. Copyright 2005, Rockefeller University Press. (b) Detecting the translocation of fluorescently tagged analytes simultaneously at an array of nanopores by using an electron multiplying charge coupled device (EM-CCD) camera. Reprinted with permission from ref. 166. Copyright 2010, American Chemical Society. (c) Schematic illustration of the unlabeled analytes being detected electrically (analog) and optically (digital) in a synchronous manner. Reprinted with permission from ref. 168. Copyright 2014, American Chemical Society. (d) Close-up view of (c), a Ca^{2+} ion gradient formed in the vicinity of the nanopore at the *cis* side, in which a low concentration of Ca^{2+} activated fluorophores are present. The DNA molecule can modulate the ionic current by the pore and hence the fluorescence intensity. Reprinted with permission from ref. 168. Copyright 2014, American Chemical Society. (e) A typical DNA translocation event (8 kbp) measured simultaneously electrically (top) and optically (red) in the confocal mode (V = 0.3 V, 1 M KCl and 0.5 M $CaCl_2$ in *trans* side, data filtered at 10 kHz; cpms = counts per ms). Reprinted with permission from ref. 168. Copyright 2014, American Chemical Society. (f) An image of 9 closely spaced nanopores with 20 μM Fluo-4 on the *cis* side at 300 mV under 488 nm illumination. Reprinted with permission from ref. 168. Copyright 2014, American Chemical Society.

current.[167] By this method, 9 closely spaced nanopores in a SiN_x membrane (thickness = 60 nm) are measured simultaneously, as shown in Fig. 5(f).[168] A prominent advantage of optical detection compared with electrical detection is the ability to optically address an array of nanopores without requiring the complex fabrication of individual sets of electrodes and the electrical isolation of each nanopore channel. This feature is crucial for applications requiring massive parallelization, such as high-throughput sequencing. With optical measurements, we can decouple these individually and detect which pores are open and translocating, which are partially opened, and which are partially blocked.[168]

3.2 Tunneling current detection

Electrodes sensing the conductance changes when nucleotides pass were first theoretically investigated by Di Ventra *et al.*[169] They found that when DNA was sandwiched between electrodes with an appropriate spatial width, each nucleotide would induce a different conductance change due to the different electronic and chemical structures of the four bases, as shown in Fig. 6(a) and (b). Fig. 6(b) shows relative changes in current when nucleotides rotate and translate through the electrodes. Clearly, even considering the rotation condition, there is still a large distinction between the nucleotides A and T and C and G. But C and G have similar electrical signatures and cannot be easily distinguished, so we need other methods to identify them, such as shot noise.[170] In 2006, Zwolak *et al.* theoretically showed that the transverse current could differentiate between nucleotides of ssDNA threading through a nanopore by coupling molecular dynamics simulations and quantum-mechanical current calculations, as shown in Fig. 6(c). The electrodes (the spacing of the electrodes is 12.5 Å) were embedded in the SSN wall, which could be used to measure the electrical current of each base while threading through the nanopore (ssDNA), as shown in the inset of Fig. 6(c), by combining transverse field control in the nanopore, and the distributions of current values for each nucleotide would be sufficiently different to enable rapid sequencing.[171]

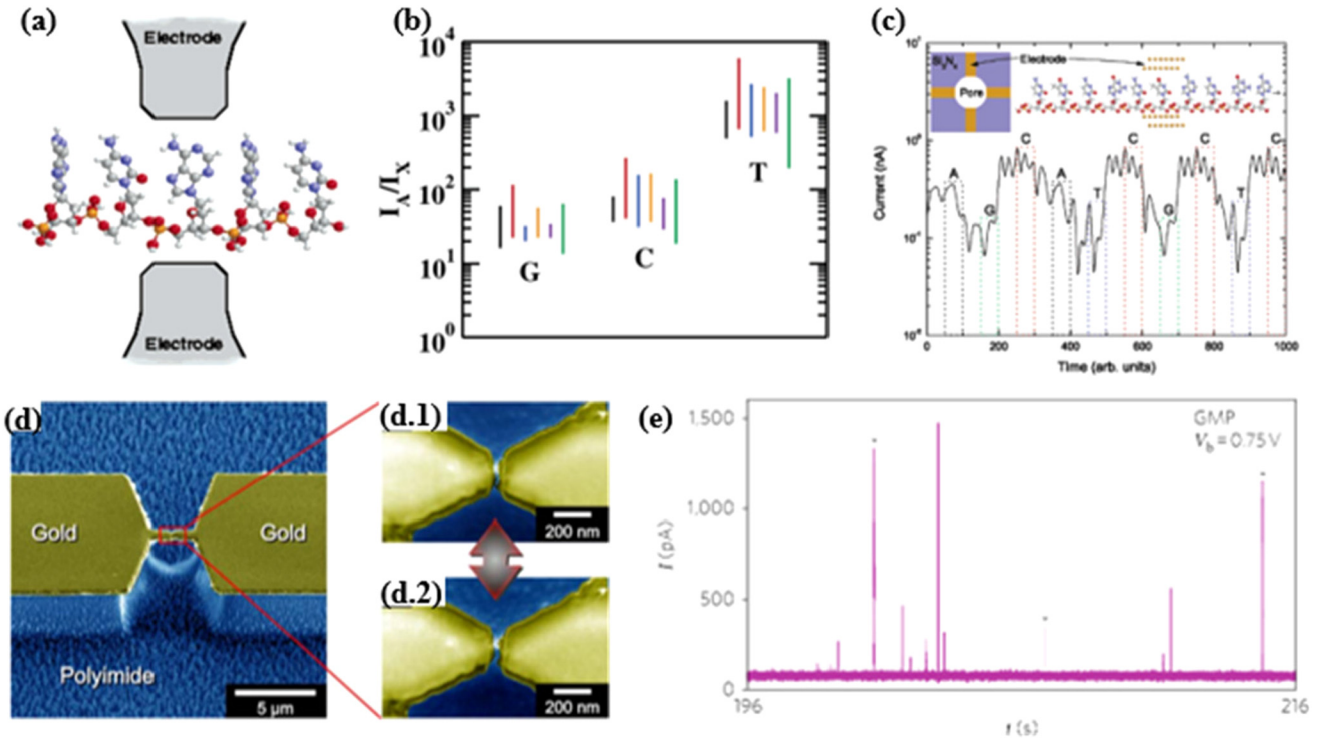

Fig. 6 Schematic of the tunneling current detection method. (a) Diagram of a polynucleotide between two nanoelectrodes; a single nucleotide was detected at a time. Reprinted with permission from ref. 169. Copyright 2005, American Chemical Society. (b) Current ratios of A to the other nucleotides G, C, and T at a bias of 0.1 V. The original configuration of A is denoted as I_A, but the directions of other nucleotides are not fixed. The six lines in the picture for each nucleotide, from left to right, correspond to rotation about the *x*-, *y*-, and *z*-axes and translation in the *x*-, *y*-, and *z*-directions. Reprinted with permission from ref. 169. Copyright 2005, American Chemical Society. (c) Transverse current *versus* time for a single strand of DNA translocating through a nanopore. The left inset represents metal electrodes embedded in a nanopore. The right inset shows a single strand of DNA passing through a set of nanoelectrodes, a unique signal from each of the bases can be obtained. Reprinted with permission from ref. 171. Copyright 2006, American Chemical Society. (d) SEM images of the close nanoelectrodes; (d.1 and d.2) magnified views of the narrowest constriction of the nanojunction in (d); the inter-electrode gap between the nanoelectrodes can be changed by bending the substrate. Reprinted with permission from ref. 172. Copyright 2010, Nature Research. (e) *I*–*t* curves obtained for GMP at V_b = 0.75 V with an electrode gap of ~1 nm, several pulse-like signals with different heights occur randomly with time. Reprinted with permission from ref. 172. Copyright 2010, Nature Research.

In 2010, Tsutsui *et al.* experimentally demonstrated the electrical detection of a single nucleotide using two configurable nanoelectrodes and found that electron transport through the single nucleotide occurred by a tunnelling mechanism.[172] Scanning electron microscopy (SEM) images of the nanogap electrode pairs are shown in Fig. 6(d). To get these characteristic signals of detection molecules, the nanoelectrode gaps must close to an average nucleotide molecule length, ~1.0 nm. Because the nanoelectrodes were fabricated on the polyimide substrate, the inter-electrode gap between the nanoelectrodes could be finely tuned to arbitrary values at sub-picometer resolution through adjusting substrate bending, as shown in Fig. 6(d.1) and (d.2). From Fig. 6(e), we can see that by using an appropriate nanoelectrode gap, guanosine 5′-monophosphate (GMP) tunneling current signals can be detected clearly.

From what has been described, the tunneling current readout method combined with a nanopore would allow one to identify individual bases while threading DNA through the nanopore, as shown in Fig. 7(a)–(c). But it is verified experimentally that, in order to obtain true tunneling detection, the gap between the electrode pairs needs to be smaller than 2.5 nm; it remains extremely challenging to obtain this narrow gap in experiments. The other important element of the tunneling current method is the thickness of the metal: if the metal is too thick, more than one base at a time would be detected. So ultrathin two-dimensional materials are used as the nanogap electrode pairs to detect the tunneling current when DNA is passing through the nanopore, as shown in Fig. 7(d). Single-atom thick graphene could be used as the membrane material as well as the electrode, so the tunnelling current would be recorded by two graphene electrode pairs; this special feature automatically solves the problem of having to fabricate nanoelectrode pairs with a nanogap that are exactly aligned with the nanopore.[39,173–178] Fig. 7(e) and (f) shows the results of the all-atom molecular dynamics (MD) simulations of different graphene nanogap sizes of 1.4 nm and 2.0 nm, respectively. Fig. 7(e) shows that the ssDNA nucleotides take comparatively more time when translocated through the 1.4 nm nanogap than the 2.0 nm nanogap. And when passing through the nanogap, the translocation time follows

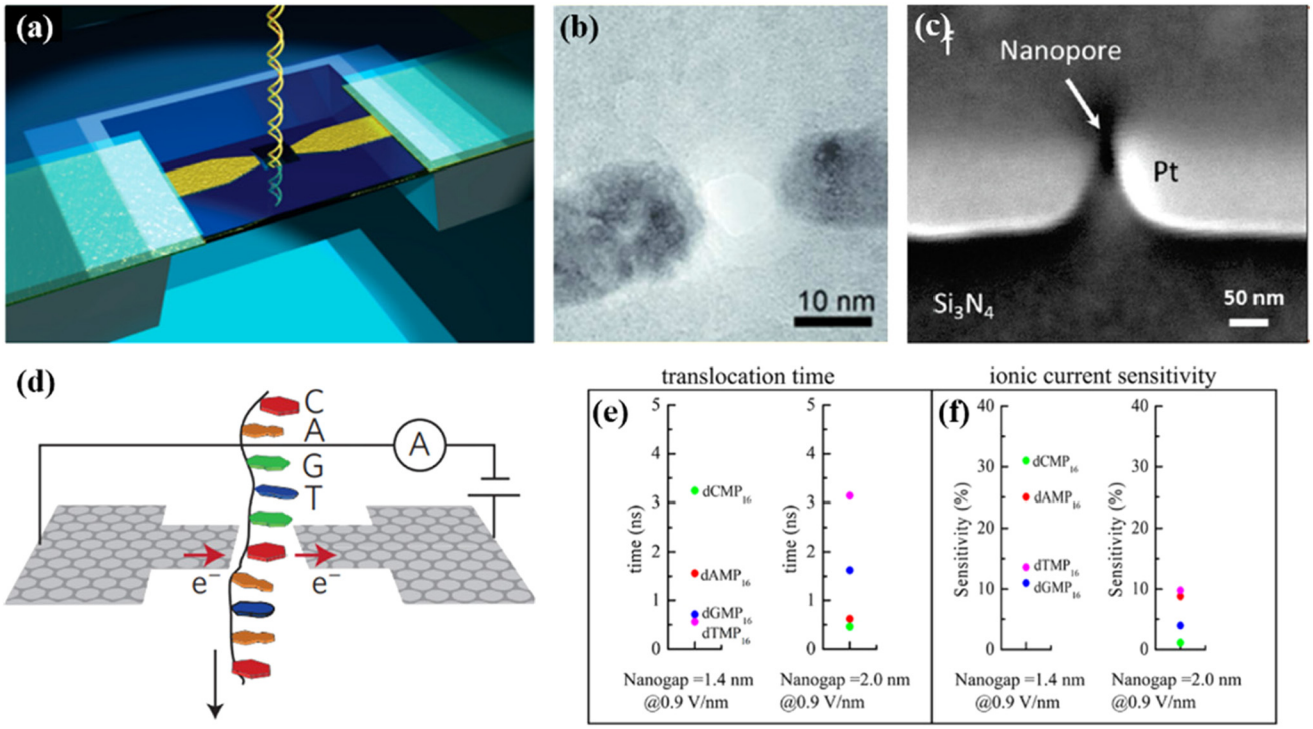

Fig. 7 (a) Schematic diagram for sequencing by combining the tunneling electrodes and nanopore. Reprinted with permission from ref. 177. Copyright 2014, American Chemical Society. (b) TEM micrograph of a nanopore drilled between two nanoelectrodes that form a nanogap of sub-10 nm. Reprinted with permission from ref. 177. Copyright 2014, American Chemical Society. (c) SEM image showing the nanopore aligned to the Pt nanoelectrodes that form a nanogap. Reprinted with permission from ref. 178. Copyright 2011, American Chemical Society. (d) Tunnelling current modulation based on different bases. Reprinted with permission from ref. 173. Copyright 2016, Nature Research. (e and f) Translocation times and ionic current sensitivity under a 0.9 V nm^{-1} electric field for all four ssDNA nucleotides when passed through different graphene nanogap sizes of 1.4 and 2.0 nm. Reprinted with permission from ref. 176. Copyright 2022, American Chemical Society.

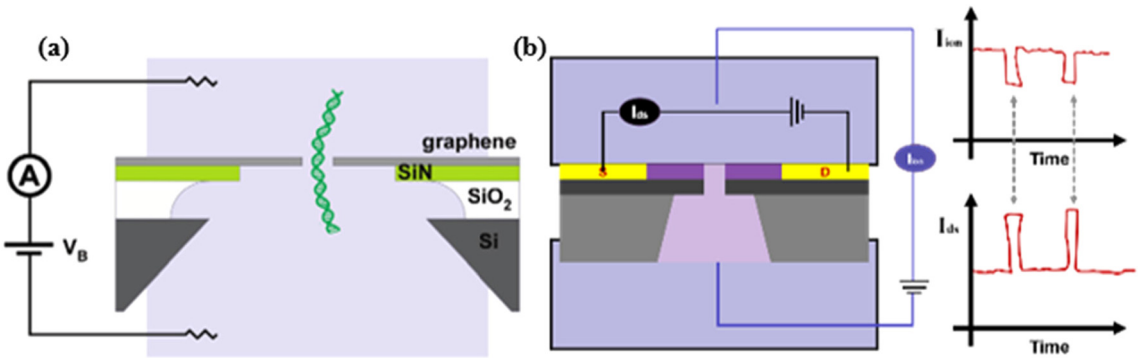

Fig. 8 Schematic diagram of the detection principle. (a) Few-layer graphene (1–5 nm thick) is located over a 40 nm thick suspended SiN_x membrane with a 1 μm diameter hole, and a transmembrane voltage, V_B, is applied between the reservoirs to drive the DNA thread through the nanopore. Reprinted with permission from ref. 179. Copyright 2010, American Chemical Society. (b) Schematic diagram of the detection principle for FET sensors (left figure); transverse current and ionic current were detected simultaneously and it was found that they changed at the same time.

the following order: dCMP16 (3.25 ns) > dAMP16 (1.60 ns) > dGMP16 (0.75 ns) > dTMP16 (0.56 ns) due to the difference in the interactions between nucleobases and nanogap edges. Fig. 7(f) shows that for a 1.4 nm nanogap, the sensitivity values are quite high, about 25.03%, 11.01%, 13.59%, and 31.01% for dAMP16, dGMP16, dTMP16, and dCMP16 nucleotides, respectively.[176] It is further verified that graphene electrode pairs can be used to realize DNA sequencing based on tunneling current detection.

3.3 Field-effect-transistor sensing detection

3.3.1 Nanopore FET sensor detection theory. Apart from tunneling current detection and optical detection described above in combination with nanopores, a new detection mecha-

nism by using FET combined with nanopores was also created. In 2010, graphene membranes were first used to detect DNA translocations through their own nanopores (5 to 10 nm in diameter) formed by electron-beam sculpting, as shown in Fig. 8(a).[179] Graphene is an excellent electrical conductor compared with traditional SSN materials (such as SiO_2, Si_xN_y, Al_2O_3, HfO_2 and so on). The use of graphene as a membrane material opens the door to a novel class of nanopore devices, in which transverse current sensing and ionic sensing are achieved directly in the same pore.

In 2010, Nelson *et al.* predicted that the transverse current signal through a graphene nanoribbon (GNR) with a nanopore could discriminate between different nucleotides by *ab initio* density functional theory.[180] A schematic of nanopore FET sensor detection theory is shown in Fig. 8(b) (left panel): a voltage between the source and drain of the nanowire/nanoribbon (Si, graphene, MoS_2, transition-metal dichalcogenide membranes, carbon nanotubes and other semiconductor materials) was applied to record the change of the current signal between the source and drain in real time, and the transmembrane voltage was also applied simultaneously to record the change of the ionic current. In theory, the transverse current and ionic current would change simultaneously, as shown in Fig. 8(b) (right panel), because when DNA translocates through the nanopore, it would not only block the pore but also have a measurable influence on the conductivity of the channel.

When using nanopore FET sensors for DNA sequencing, both transverse current and ionic current trajectories are simultaneously recorded. In nanopore FET sensors, one of the roles of the nanopore is to act as a locator, guiding DNA molecules to thread through a pre-set channel region. In turn, translocation of DNA would cause changes in the channel current, enabling DNA sequencing. The detection mechanism of the ionic current is consistent with traditional SSNs; and the mechanism for detecting a transverse current is primarily divided into three different types of signal, as shown in Fig. 9. Firstly, the detected FET current signal is derived from capacitive coupling, its signal amplitude is independent of the bias voltage applied to both ends of the channel, and always has the same symbol, as shown in Fig. 9 (top panel). The signal can be defined as $I_c = C_c \times \frac{\Delta V_L}{\Delta t}$, where ΔV_L is the change in the local potential of the nanopore due to DNA translocation, Δt is the timescale for realizing this change, and C_c is the capacitance of the channel to the electrolyte at the nanopore. Secondly, the transverse current changes due to the electrostatic interaction modifying the Fermi level of the channel material, as shown in Fig. 9 (middle panel). This electrostatic signal can be defined as $I_e = g_m \times \Delta V_e$, where g_m is the transconductance of the FET device and ΔV_e is the potential change, with two possible sources. The first comes from the negative charge of the DNA backbone, $\Delta V_{e,1} = \Delta\Delta_Q = \frac{Q_{eff}}{C_g}$, where Q_{eff} is the effective charge of DNA; and the second comes from the local potential change caused by DNA translocation through the nanohole, $\Delta V_{e,2} = \Delta V_L$.[163] Thirdly, the variation in the FET current signal results from base-specific modulation caused by the non-electrostatic interaction between DNA and the channel material, as shown in Fig. 9 (bottom panel). Numerous theoretical calculations have shown that the presence of DNA bases results in substantial current modulation, and increases with the bias voltage applied to the channel material.[180–187] However, the magnitude and sign of the current changes depend on various factors, including the width of the structure, the location, size and shape of the nanopore, and the types of channel material, and therefore cannot be known *a priori*.[188]

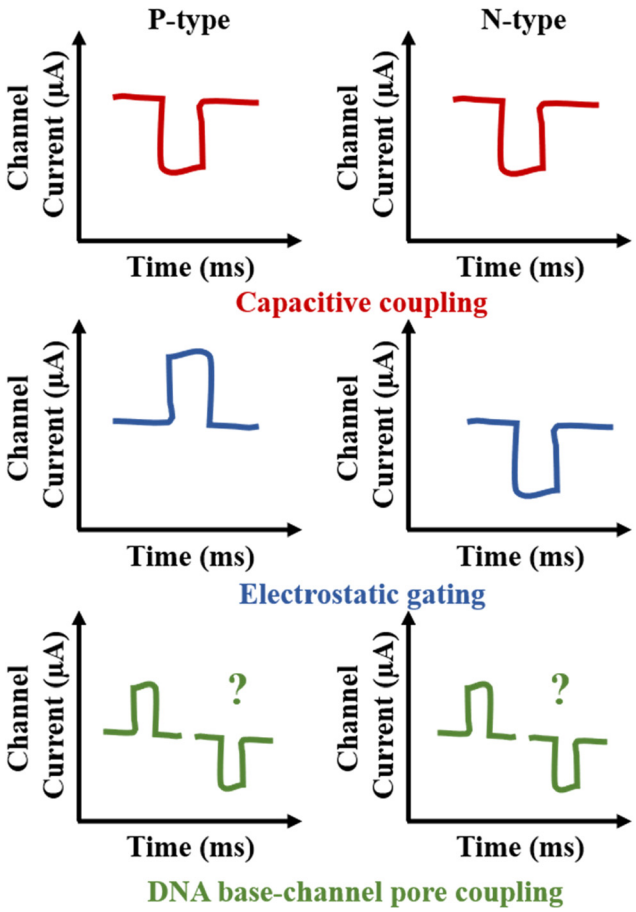

Fig. 9 Three different detection mechanisms for nanopore FET sensors. Reprinted with permission from ref. 188. Copyright 2018, American Chemical Society.

3.3.2 Si-based nanopore FET sensors. According to the above theoretical description, DNA sequencing can be achieved with nanopore FET sensors in a fast and low-cost manner. The preparation process for nanopore FET sensors is more complicated than that of traditional SSNs. However, with the advancement of semiconductor processing technology, it is possible to successfully prepare nanopore FET sensors. In 2012, Ping Xie *et al.* showed the first experimental realization of silicon nanowire–nanopore FET sensors,[163] as shown in Fig. 10.

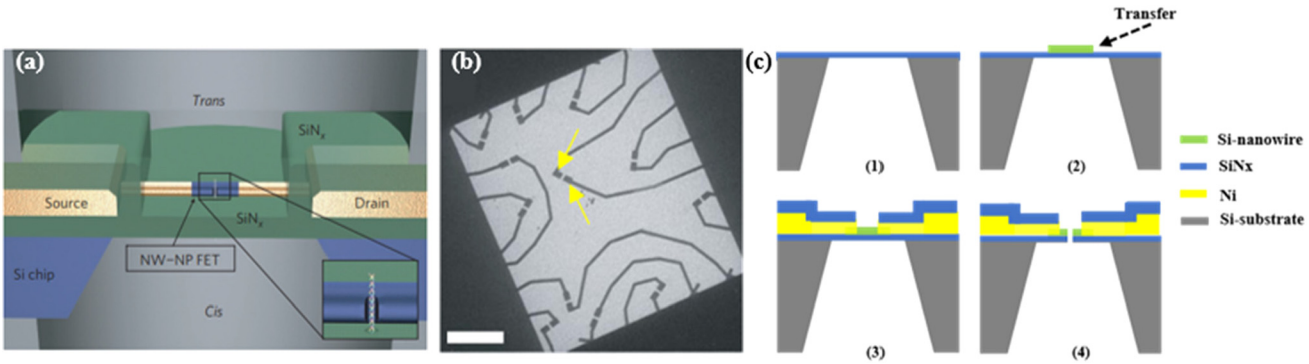

Fig. 10 (a) Schematic diagram of the nanowire–nanopore FET sensor. Inset: magnified view of the nanopore and nanowire–nanopore. Reprinted with permission from ref. 163. Copyright 2012, Nature Research. (b) Low resolution TEM image of the suspended SiN_x membrane part of a nanowire–nanopore FET chip. Scale bar = 20 μm. Dark lines on the membrane are metal leads and contacts. Yellow arrows point to the source and drain of a nanowire–nanopore FET. Reprinted with permission from ref. 163. Copyright 2012, Nature Research. (c) Preparation process for a Si based nanowire nanopore FET device.

The entire preparation process is shown in Fig. 10(c). The sensor on SiN_x membrane is integrated through a short-channel Si nanowire and a nanopore, and the nanopore extends through both the Si nanowire edge and the SiN_x membrane, as shown in the inset of Fig. 10(a). The p-type Si nanowires were synthesized by chemical vapor deposition (CVD) with diameters ranging from 30 to 50 nm, and then were dispersed onto 50 nm thick 100 μm × 100 μm SiN_x TEM membrane grids. EBL and electron beam evaporation (Ni = 60 nm) were applied to define the source and drain of the Si nanowire (the channel length was ~1 μm), and then 75–100 nm thick silicon nitride film was deposited by plasma enhanced CVD to passivate the Ni electrodes. In order to further improve the detection sensitivity of the nanopore FET sensor, it is necessary to reduce the channel length to reduce the series resistance of the channel. By annealing treatment in the formation gas ($H_2:N_2$, 10 : 90) at 380 °C for 135 s, the channel length was reduced from ~1 μm to less than 200 nm due to conversion to metallic NiSi.[189] After annealing, a nanopore of ~10 nm in diameter was obtained by TEM at the specific location for 2–5 min. Following TEM, devices were cleaned by UV-ozone stripping at 300 K for 25 min to remove carbon deposition. Finally, the device was annealed again in the formation gas at 250–350 °C for 30 s to restore or improve the transistor characteristics (the channel material was damaged during TEM).

The schematic test diagram and equivalent circuit diagram are shown in Fig. 11(a) and (b). The equivalent circuit separates the total solution resistance into three parts, including nanopore resistance (R_{pore}) and *cis* and *trans* chamber access resistances (R_{trans} and R_{cis}). The Si-based nanowire–nanopore FET sensor can be conceptually simplified as a point-like potential detector located at the nanopore opening on the *trans* side. This model facilitates our understanding of how the sensor operates in the process of DNA sequencing. The nanopore will be partially blocked during DNA translocation, which leads to a transient change in the nanopore's resistance as well as to the access resistances of both chambers involved. The electrical potential change around the nanopore opening in the *trans* chamber during DNA translocation can be quantitatively described by the following equation:[163]

$$\Delta V \approx \frac{2VA(4l+d)\left(\frac{C_{cis}}{C_{trans}}-1\right)}{\pi \ln\left(\frac{C_{cis}}{C_{trans}}\right)(2l+d)\left(d^2\left(\frac{C_{cis}}{C_{trans}}-1\right)+4(2l+d)r\right)} \quad (2)$$

Here, V, A, l, d, C_{cis}, C_{trans} and r are the voltage, cross-sectional area of DNA, membrane thickness, nanopore diameter, *cis* and *trans* chambers buffer salt concentrations, and distance to the nanopore opening, respectively. According to eqn (2), some simulation results are shown in Fig. 11(c) and (d). From Fig. 11(c), the potential changes increased with decreasing nanopore diameters, and the *cis*/*trans* concentration ratio would also influence the potential change. In addition, Fig. 11(d) shows the predicted distribution of the potential change in the *trans* chamber (diameter: 10 nm, voltage = 1 V); the potential changes were mainly concentrated within tens of nanometers of the nanopore, which further showed the possibility of high-density integration of nanowire–nanopore FET sensors without crosstalk. In experiments, the transverse current and ionic current were observed simultaneously at Si nanowire–nanopore FET sensors when DNA translocated through the pore, as shown in Fig. 11(e). The magnified pictures (right panel in Fig. 11(e)) showed the changes of ionic current and FET conductance clearly; the FET current change is ~30 nA compared with ~3 nA ionic current changes during DNA translocation. The relatively large translocation signal could provide higher bandwidth recording, which would be beneficial for rapid DNA sequencing and improved sequencing efficiency.

Multi-channel detection of DNA translocation signals with three nanowire–nanopore FET sensors are shown in Fig. 11(f). The three FET channels operate independently, so the total ionic current detection is related to the three nanowire–nanopore FET sensors, but every falling or rising edge in the total

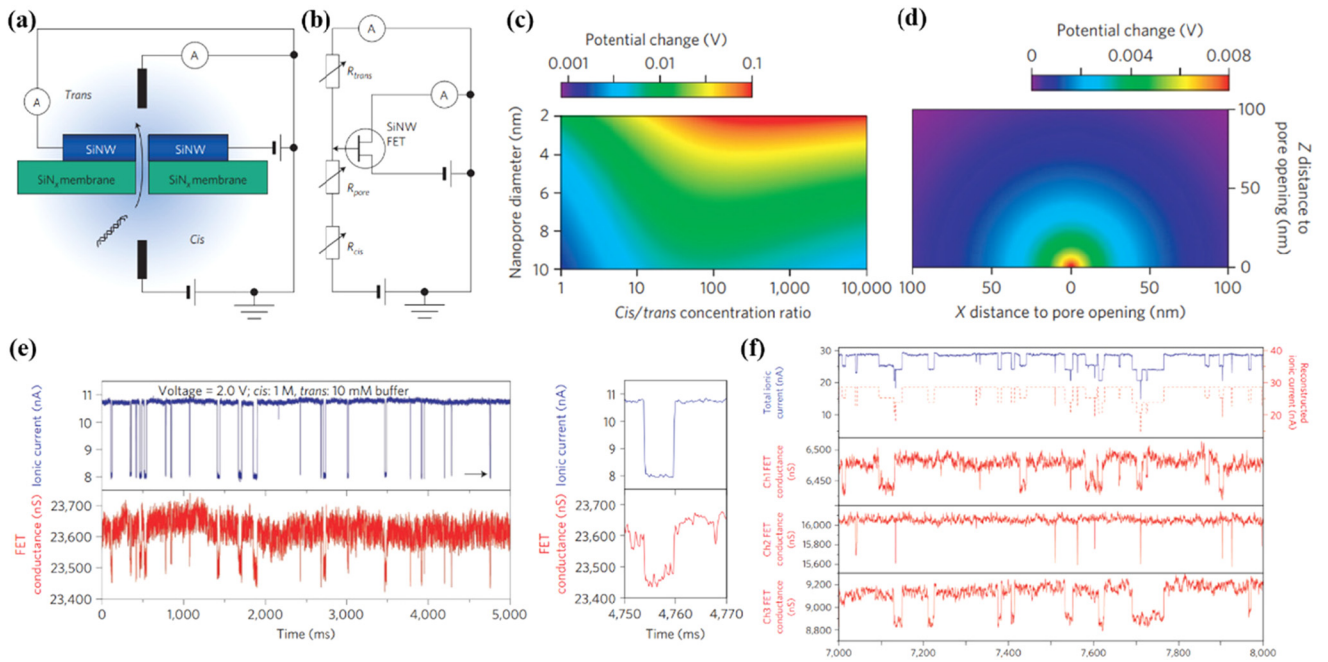

Fig. 11 Sensing mechanism and test results for Si nanowire–nanopore FET sensors. (a) Schematic diagram of the sensing circuit. (b) Equivalent circuit diagram of (a) silicon nanowire (SiNW). (c) The calculated change in potential at the nanopore opening in the *trans* chamber when one dsDNA molecule threads through the nanopore at 1 V as a function of nanopore diameter and *cis*/*trans* chamber buffer concentration ratio. (d) Calculated potential distribution in the *trans* chamber for a 10 nm diameter nanopore at 1 V obtained from eqn (2). (e) Simultaneously recorded ionic current and FET conductance signals at 2 V with a *trans* chamber KCl buffer concentration of 10 mM, *cis* chamber KCl buffer concentration of 1 M and 1.4 nM pUC19 DNA. (Right panel) Magnified view of single ionic current and FET conductance events, represented by a black arrow on the corresponding ionic current traces on the left panel. (f) Magnified view of the multiplexed recording. The dashed red trace in the top corresponds to the reconstructed ionic current trace calculated from the three FET traces. The measurements were made with 1 M KCl/10 mM KCl (*cis*/*trans*) buffer, 3 V voltage, and 1.4 nM pUC19 DNA. Reprinted with permission from ref. 163. Copyright 2012, Nature Research.

ionic current channel can be uniquely correlated to a corresponding edge in one of the three FET channels; this also further confirms the high-density integration and application of nanowire–nanopore FET sensors (signal decay ~ tens of nanometers). Combining simulation and experimental results, it was discovered that the FET signal detected in the Si-based nanowire–nanopore sensor did not originate from direct charge sensing. This conclusion is drawn from the observation that the negatively charged backbone of DNA does not increase the conductivity of the p-type channel during translocation as one might initially expect. Instead, a decrease in the FET channel conductivity is observed, as illustrated in Fig. 11(e) and (f). Besides, when both chambers were filled with 1 M KCl buffer, no noticeable FET signal was observed and there were only small and slow conductance baseline shifts; this is because under balanced buffer conditions, the nanopore dominates the solution resistance and the voltage drops mainly across the nanopore. So, when DNA translocated through the nanopore, there was no significant potential change near the nanopore, which could not cause a variation in FET conductance. By altering the concentrations in the chambers and the types of translocation molecule (neutral PEG: the ionic current and the FET conductance signals were observed simultaneously), it was further confirmed that the changes in FET conductivity originated from the highly localized potential changes in the vicinity of the nanopore rather than direct charge sensing, during DNA translocation.

In 2016, Yanagi *et al.* proposed novel side-gated Si-based ultrathin-channel nanopore FET sensors (thickness of the channel was ~2 or 4 nm) with high spatial resolution and sensitivity.[190] Compared with the structure proposed by Ping Xie *et al.*, the side-gated Si-based ultrathin-channel nanopore FET sensor is more complex; the biggest differences are that it has two side-gate electrodes and an ultrathin Si channel. In this configuration, the spatial resolution is significantly improved compared with the sensor of Ping Xie *et al.* The fabrication of the nanowires involved a top-down method, which was more controllable and repeatable compared with a chemical method. The detailed preparation process for the sensor is shown in Fig. 12, which includes 10 main steps.

Firstly, SiN_x/SiO_2/P- or N-doped amorphous-Si multilayer films were deposited on Si substrate by low-pressure chemical vapor deposition (LPCVD) and then patterning. Then, a multilayer of non-doped a-Si/SiO_2 was deposited onto the front and back sides of the wafer using LPCVD. The poly-Si/SiO_2 multilayer was then patterned to form the channel by RIE. After patterning, the SiO_2/Si_3N_4 multilayer was deposited using LPCVD. Then, the SiO_2 layer with a thickness of 500 nm was deposited and then planarized by chemical mechanical polishing (CMP) to precisely control the total stress of the membrane. After

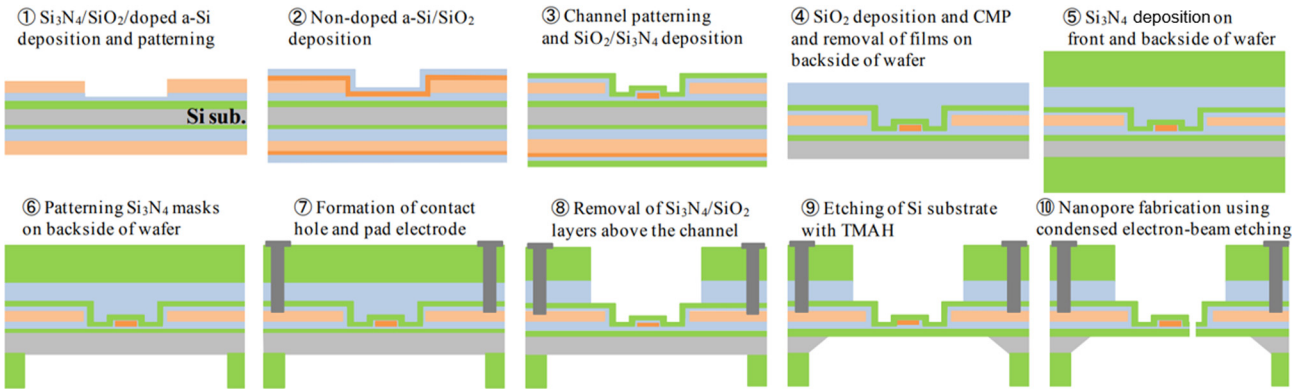

Fig. 12 Schematic diagram of the fabrication process for Si-based ultrathin-channel nanopore FET sensors. Reprinted with permission from ref. 190. Copyright 2016, IOP Publishing.

CMP, all films on the back side of the wafer were removed by RIE. After that, the Si_3N_4 layer was deposited by plasma-enhanced chemical vapor deposition (PECVD), followed by patterning SiN_x on the back, to form the etching mask of the Si substrate. The contact windows at source-drain-gate electrodes were formed by dry etching. Ti/Al (50/200 nm) was deposited by sputtering, and then patterned to form pad electrodes. After that, the SiO_2/Si_3N_4 layer above the channel was half-etched by RIE. Then, the Si substrate was etched with TMAH (85 °C, 9 h) to form a suspended structure; the remaining SiO_2 layer above the channel was removed with hydrofluoric acid. Finally, nanopores with diameters of ~5 to 8 nm were successfully prepared by TEM. The final structural diagram of the sensor is shown in Fig. 13(a). The sensor is above the suspended membrane and consists of the nanopore, source electrode, drain electrode, lightly doped channel, control gate and back gate.

A TEM image of the final sensor is shown in Fig. 13(b): a nanopore is located between the control gate (CG) and the Si nanowire channel, which is formed close to the channel by TEM; this can improve the detection sensitivity. A magnified view of the nanopore is shown in Fig. 13(c), with a diameter of about 5.3 nm. Since this structure has two side-gate electrodes,

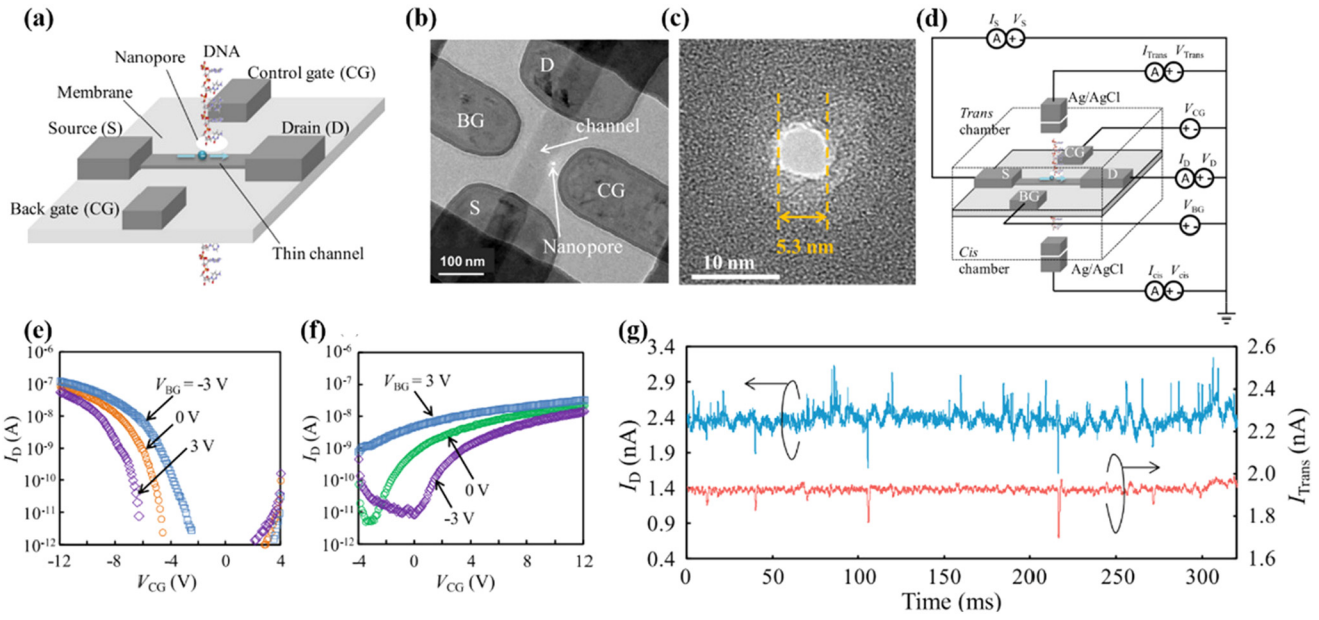

Fig. 13 Side-gate ultra-thin channel nanopore FET sensor for DNA translocation testing. (a) Schematic diagram of the side-gated, ultrathin-channel Si nanowire nanopore FET sensor. (b) A TEM image of the top view of a side-gate Si nanowire nanopore FET; the nanopore is between the channel and the control gate. (c) Magnified view of nanopores fabricated with a diameter of approximately 5.3 nm. (d) Circuit for the measurement of a FET nanopore sensor. (e and f) Back gate dependence of the V_{CG}–I_D characteristics of the p/n-type FETs before nanopore formation (p-type: t_{ch} = 4 nm, $V_{BG}/V_S/V_D$ = 0/0/−1 V, V_{CG} = −3, 0, 3 V; n-type: t_{ch} = 2 nm, V_S/V_D = 0/1 V and V_{BG} = −3, 0, 3 V). (g) Simultaneous recording of ionic current and p-type FET current with 1 M KCl/0.01 M KCl (*cis*/*trans*) buffer, $V_{cis}/V_{trans}/V_{CG}/V_{BG}/V_S/V_D$ = −4.7/−1/0/0/0/−1 V, and 5 nM 1 kbps ds DNA. Reprinted with permission from ref. 190. Copyright 2016, IOP Publishing.

the test circuit becomes more complex, as shown in Fig. 13(d). When it came to testing, the sensor was mounted onto a custom-built acrylic flow cell, and the two chambers were separated by the membrane. Electrical contact to the electrode of sensor was achieved by nickel contact probes. The transverse current and ionic current were measured using Axopatch 200B and homemade amplifiers, respectively. The measurement data were low-pass filtered with a cut-off frequency of 2 or 5 kHz by a four-pole Bessel filter. Fig. 13(e) and (f) shows the relationship between the source-drain current of p-type/n-type sensors and the applied gate voltage (V_{CG}, V_{BG}), respectively. The threshold voltage of the sensor could be controlled through the back gate. The two gates could work collaboratively to control the source-drain current and the magnitude of the transconductance ($d\Delta I/d\Delta V$), and then adjust the detection sensitivity of the nanopore FET sensor. The undoped amorphous Si nanowire channel material was prepared by LPCVD, which could control the growth thickness of the film, so 2 nm and 4 nm thick polycrystalline silicon films were successfully prepared. Due to the Coulomb scattering effect between carriers, when the thickness of the Si nanowire channel is 2 nm, the probability of only one carrier in the thickness direction is as high as 90%, which significantly improves the spatial resolution of the Si nanowire nanopore FET sensor. The high sensitivity and spatial resolution described above can facilitate DNA sequencing.

During testing, the source-drain voltage and the ion voltage were applied synchronously, and the transverse current and the ionic current would be recorded simultaneously during DNA translocation, as shown in Fig. 13(g). This result is similar to the behavior of p-type Si nanowire–nanopore prepared by Ping Xie *et al.*[163] Synchronized with ionic current blocking, Fig. 13(g) shows large spikes in transverse current I_D, indicating that I_D is able to detect DNA translocation through the nanopore. The change in transverse current I_D is still negative for a p-type transistor, which is not expected, because DNA carries negative charges, which should increase the transverse current, but this result is consistent with a previously reported result.[163] According to experimental analysis, this abnormal phenomenon is mainly due to the fact that the charges of DNA are shielded by counter-ions, and what the channel detects is a change in the electric potential near the exit of the nanopore in the *cis*-chamber. The potential change is caused by the increase of the series resistance of the nanopore and the *trans*-chamber in the solution during DNA translocation. The increase in series resistance leads to a drop in voltage near the exit of the nanopore, resulting in a negative change in the transverse current I_D.[190] In Fig. 13(g), the up-pointing signals in the channel current were random telegraph noise (RTN) due to the trapping and detrapping of carriers at the interface state between poly-Si and SiO_2. RTN can be inhibited by converting the channel material from polysilicon to single-crystalline silicon and preparing the channel with a specific crystal orientation, as well as by improving the manufacturing process to further reduce the interfacial state density.

The silicon-based nanowire–nanopore FET sensor, as described above, stands out for its ability to detect single molecules with high sensitivity. This technology, which integrates the precision of nanowire structures with the specificity of nanopore sensing, and can achieve miniaturization and multiplexing detection. A key advantage of Si-based FET nanopores is their compatibility with complementary-metal-oxide-semiconductor (CMOS) fabrication processes. This compatibility ensures high repeatability and reliability, benefiting from the standardized manufacturing processes in CMOS technology. Such standardization is a significant step forward in the fabrication of nano-biosensors, as it enables more consistent and scalable production. However, since the distance between DNA bases is only 3.4 Å, it is vital to further reduce the thickness of the Si channel material in order to achieve DNA sequencing, which poses a huge challenge for processing. Overall, the silicon-based nanowire–nanopore FET sensor offers a highly sensitive and integrable method for molecular detection, but there are still some technical and application limitations. Continued progress in nanofabrication techniques and material engineering is essential to overcome these challenges and fully realize the potential of this promising technology in applications such as DNA sequencing and molecular diagnostics.

3.3.3 Nanopore FET sensors based on two-dimensional materials. Firstly, two-dimensional materials are a special class of materials, the thickness of which is only a few atomic layers. For example, graphene film is only 3.35 Å thick (equivalent to the distance between two bases in the DNA strand, 3.4 Å), so it can provide a suitable film thickness for DNA sequencing. Secondly, graphene has very high electron mobility, which means that electrons can move through the material at very high speeds. This enables the graphene nanopore FET to operate at higher frequencies than the silicon-based nanopore FET, which facilitates rapid DNA sequencing.

GNR nanopore FET sensors were theoretically validated in 2010 with sufficient sensitivity to distinguish between different nucleotides, enabling large-scale parallel DNA sequencing.[180,191] Many theoretical and computational studies on the transport of GNR and graphene quantum dot contacts with a nanopore have shown that the presence of DNA bases inside the nanopore can lead to current changes in graphene nanostructures based on base-specific modulation. Therefore, in theory, DNA sequencing can be realized when the molecule passes through the nanopore.[180–187,192–196] A schematic diagram of the FET nanopore model is shown in Fig. 14(a). The four different bases produce very different current modulations in DNA translocation, mainly due to their different chemical compositions and different coupling strengths to GNR. During sequencing, base rotation would lead to expansion of the conductance modulation; the shaded regions representing overlapping regions are shown in Fig. 14(b). These studies show that non-electrostatic base-specific interactions between DNA bases and GNR could lead to changes in local state density around the nanopore, resulting in changes in the resistivity of the nanoribbons, which could be measured by the nanoribbon transverse current, as shown in Fig. 14(c).[192] Fig. 14(d) shows the simulation results of the density of states

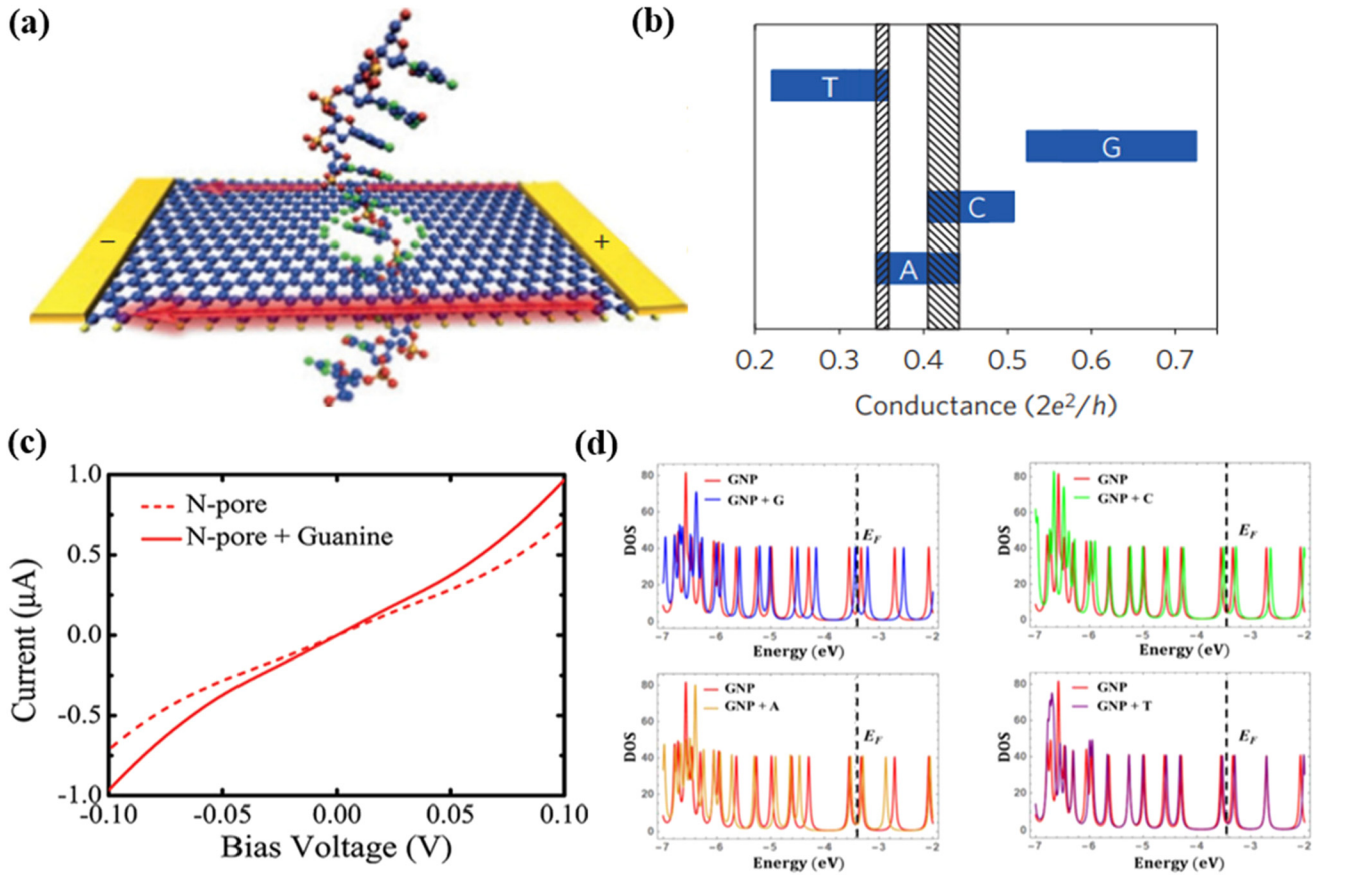

Fig. 14 (a) Schematic diagram of a metallic zigzag graphene nanoribbon with a nanopore, where current flows mainly around the zigzag edge (red arrow). Reprinted with permission from ref. 173. Copyright 2016, Springer Nature. (b) Conduction modulation was induced by four different bases; the rotation of the base causes a spread of the conductance modulation. The shaded areas represent overlap between different base conductance modulations. Reprinted with permission from ref. 181. Copyright 2012, American Chemical Society. (c) I–V_{sd} curves of the GNR nanopore FET sensor; the nanopore is located at the center of GNR. Reprinted with permission from ref. 181. Copyright 2012, American Chemical Society. (d) The presence of bases affects the density of states. Density of states of the pristine graphene nanopore and pristine graphene nanopore + base were described, and E_F is the Fermi energy of a pristine graphene nanopore. Reprinted with permission from ref. 196. Copyright 2021, AIP Publishing.

for the original graphene nanopore and the original graphene nanopore with DNA bases, indicating that the presence of DNA bases does cause changes to the local state density.[196] In addition to graphene, other 2D materials also prove to be suitable candidates for DNA translocation FET current detection, such as MoS_2,[184,197] phosphorene,[196] silicene,[196] $Ti_2C(OH)_2$ MXene,[187] borophene,[124,198–201] 2D C_xN_y,[122,123,202] *etc.*

Since 2010, two-dimensional material nanopore FET sensors have received sufficient attention and research. According to the above description, two-dimensional material nanopores have high spatial resolution due to only a few atomic layers; in addition, the conductive nature of the two-dimensional material enables it to precisely measure the tiny changes that occur in the transverse current as DNA threads through the nanopore, enabling rapid sequencing of DNA. In 2013, Traversi *et al.* showed the first experimental realization of a GNR nanopore FET sensor. GNR with a nanopore is located on a suspended 20 nm thick SiN_x membrane, and Cr/Au metal electrodes on both sides are used to detect changes in current between the source and drain when DNA is translocated through the graphene nanopore. The detailed preparation process and optical and TEM images of the GNR nanopore FET sensor are shown in Fig. 15.[203] Firstly, 60 nm/20 nm SiO_2 and low-stress SiN_x were grown on a B-doped 380 μm thick silicon wafer. Then, the SiO_2/SiN_x multilayer films on the back of the wafer were patterned by EBL and RIE. After patterning, the suspended SiN_x film was prepared by wet etching Si with KOH solution, as shown in Fig. 15(a). After that, monolayer graphene film grown by chemical vapor deposition was transferred above the suspended SiN_x film, as shown in Fig. 15(b). EBL and RIE (oxygen plasma) were used to define the size and corresponding positions of GNRs. Next, Cr/Au = 5 nm/50 nm double-layer metal contact electrodes were prepared by EBL, electron beam evaporation (EBE) and lift-off, as shown in Fig. 15(c). To minimize ionic cross-conductance, the atomic layer deposition (ALD) technique was used to deposit 5 nm thick aluminum oxide (Al_2O_3) on top of the electrodes, which would isolate the electrodes from the electrolyte. Finally, nanopores were successfully fabricated on GNRs using TEM operating in scanning mode, as shown in Fig. 15(d).

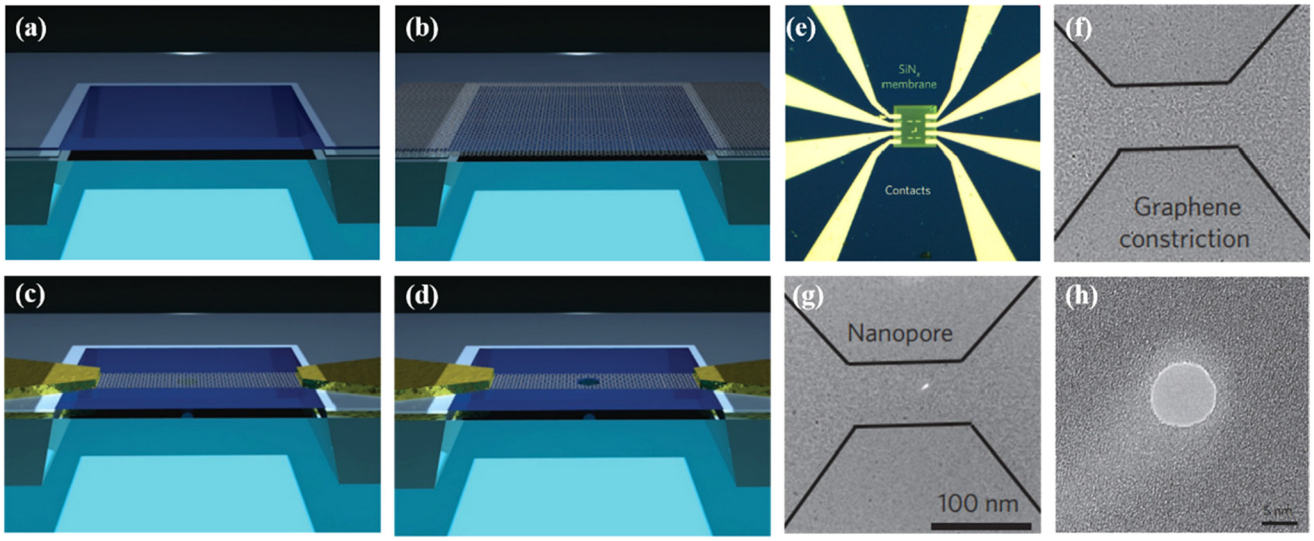

Fig. 15 Fabrication of a GNR nanopore FET sensor. (a–d) The entire fabrication process for the device. (e) Optical micrograph of Cr/Au electrodes in contact with four GNRs on a suspended SiN_x membrane. Image dimensions: 120 μm × 120 μm. (f and g) TEM images of GNR before and after nanopore drilling, respectively. (h) Magnified view of a TEM image of a nanopore. Reprinted with permission from ref. 203. Copyright 2013, Nature Research.

Fig. 15(e) shows the optical picture of the final sensor, where four GNR sensors are simultaneously fabricated on a suspended SiN_x film. Fig. 15(f) and (g) are TEM images of GNRs before and after drilling; the nanopore is basically located in the center of the GNR. The magnified view of the nanopore with a diameter of 10 nm is shown in Fig. 15(h).

The equivalent circuit model of the GNR nanopore FET sensor is shown in Fig. 16(a). The Al_2O_3 passivation layer is represented by a parallel resistor (R_{oxide}) and capacitance (C_{oxide}). The quality of the Al_2O_3 passivation layer is critical and the resistance needs to be as high as possible (in this case, 10 GΩ) to ensure good electrical isolation between the GNRs and the electrolyte solution to avoid current crosstalk. During the test, in order to maintain the quality of the Al_2O_3 passivation layer, low ionic strength (10 mM KCl) was maintained on one side of the sensor area. When the ionic strength was too high, degradation of the Al_2O_3 passivation layer would be caused during the test, which was not expected during the test.[164] In Fig. 16(g) and (h), the events of incoherent translocation of ionic current and GNR current are simulated by using an advanced design system (ADS). These images illustrated the distinct translocation events of ionic current and GNR current, thereby effectively demonstrating that the changes observed in the GNR channel current were not a result of crosstalk. This differentiation is crucial, as it stresses the specificity of the GNR channel in responding to molecular events, ensuring that the signal changes are attributed to the intended molecular interactions rather than unintended electrical crosstalk.

For DNA translocation experiments, the applied transmembrane voltage is in the range of 100–400 mV, and the source-drain voltage of the GNR is set to 20–100 mV. During the experiment, it was observed that the DNA molecule passing through the pore would cause a decrease in ionic current in 10 mM KCl solution (low salt concentrations), which was contrary to earlier reports,[204] mainly because of the positive charges on the side wall of Al_2O_3, which caused a decrease in ionic current even at very low salt strength, as shown in Fig. 16(b). Simultaneous events on the graphene transverse current and the ionic current were also observed from Fig. 16(b); this is similar to the results for the Si-based nanowire–nanopore FET sensor. Fig. 16(c) and (d) shows enlarged views of a single related event during DNA translocation. It can be seen that the graphene channel current both dips and spikes in the electrical current flowing through the GNR, which is different from the results of the Si-based nanowire–nanopore FET sensor; this is mainly due to the bipolar nature of graphene.

The scatter plots shown in Fig. 16(e) and (f) describe the translocation duration and current drop of the ionic current and graphene channel current, respectively. The scatter plots of translocation events detected by ionic currents and graphene channel currents can be divided into two types of event. One is a long translocation time and high current change events, and the other is a short translocation time and low current change events. It can be seen from the scatter diagrams that the ionic current and graphene channel current related events basically belong to the first class of translocation events with very few exceptions. For ionic currents, uncorrelated translocation events were characterized by rapid and shallow changes, mainly due to the fact that the DNA molecule only collides with the nanopore without translocation through it.[205] During these collision events, the blockage of the nanopore is too weak to effectively change the electrostatic potential near the nanopore, so GNR cannot be gate-controlled. The very fast translocation events detected in the graphene channel

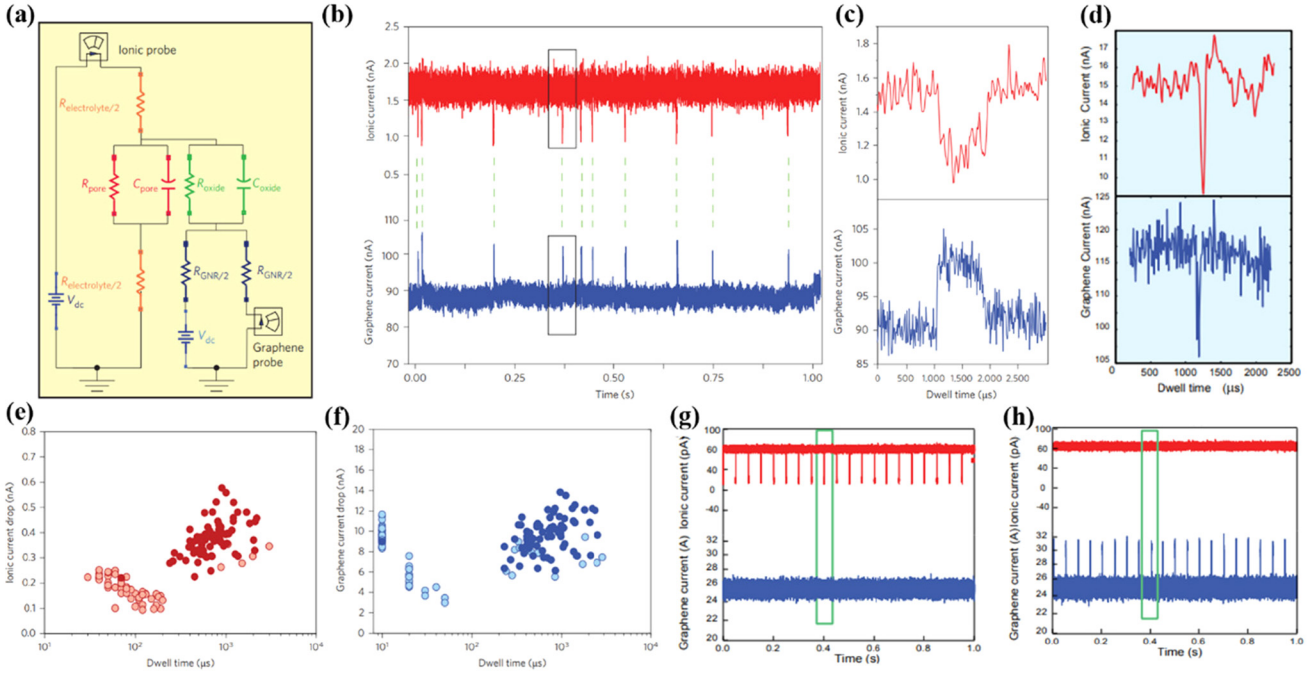

Fig. 16 Equivalent circuit diagram and analysis of test results. (a) Circuit diagram of a FET nanopore sensor. (b) Simultaneous recording of DNA translocations under an ionic current and graphene current (pNEB DNA in 10 mM KCl; transmembrane voltage, 200 mV; graphene source–drain voltage, 20 mV). (c and d) Different changes in GNR current upon DNA translocation, indicating p-type and n-type graphene transistor behavior, respectively. (e and f) Scatter plots of events detected under ionic currents and graphene currents, respectively, where relevant events are represented by filled colored circles and unrelated events are represented by partially transparent circles. (g and h) Incoherent translocation events of an ionic current and a GNR current (500 mV ionic bias and 10 mV graphene bias; 10 mM KCl buffer). Reprinted with permission from ref. 203. Copyright 2013, Nature Research.

current, but undetectable by the ionic current, may be attributed to local conductance changes in GNR caused by the presence of charged molecules in the solution far from the nanopore.

Unlike Traversi *et al.*,[203] Puster *et al.* prepared a nanopore at the edge of GNR by TEM operating in scanning mode.[206,207] The preparation diagram for the nanopore and the final results are shown in Fig. 17(a) and (b). In order to minimize damage to GNR induced by the electron beam during nanopore preparation, Puster *et al.* studied the damage to GNR caused by the electron beam under TEM and STEM imaging conditions. In particular, they measured *in situ* changes in GNR resistance with electron dose by using a TEM scaffold equipped with electrical measurements. Results under TEM and STEM imaging conditions are shown in Fig. 17(d) and (e), respectively. It can be seen from Fig. 17(d) that in TEM imaging mode, in order to locate the edge position of GNR, the GNR resistance increases linearly and irreversibly with an increase of the electron irradiation time, and even irreversible damage occurs before the beam is fully condensed to form the nanopore. In this mode, the extended electron beam is continuously illuminated over a large area of the sample being observed, as shown in the large red circle in the illustration in Fig. 17(d). The increase in GNR resistance is due to the continuous production of defects in graphene. In graphene, the resistance is linearly related to the defect density, $n_d = \sigma \times D$, where σ is the displacement cross section, D is the irradiation dose, and the dose is the product of current density (j) and time (t), so $R \approx n_d = \sigma \times D = \sigma \times t \times j$. These relationships are shown in Fig. 17(d). In TEM mode, these high magnification rates are required to position the nanopore next to GNR, which results in significant destruction of GNR in a short time.

Fig. 17(e) shows the change of GNR resistance over time in STEM imaging mode. As shown by the arrow in the figure, the resistance of GNR in each STEM image is increased in steps, and the damage occurs only in a short time when the beam scans GNR. In contrast to TEM mode, convergent beams illuminate the sample at discrete locations, as shown by the array of red dots in the illustration of Fig. 17(e). Unlike TEM nanopore preparation, any damage generated during STEM imaging is uniform on GNR and does not preferentially select the area around the nanopore, ensuring that the area of the device close to the nanopore is as sensitive as the rest of the device. In STEM mode, GNR can be imaged once, precisely controlling the dose to determine where the nanopore is formed. For a given Si_3N_4 film thickness, the size of the nanopore created in STEM mode can be calibrated and controlled by adjusting the electron probe residence time and monitoring the electron energy loss spectroscopy (EELS) signal. The EELS signal provides an accurate representation of the material composition within the electron probe region and enables real-time monitoring of the sputtering of atoms in the membrane

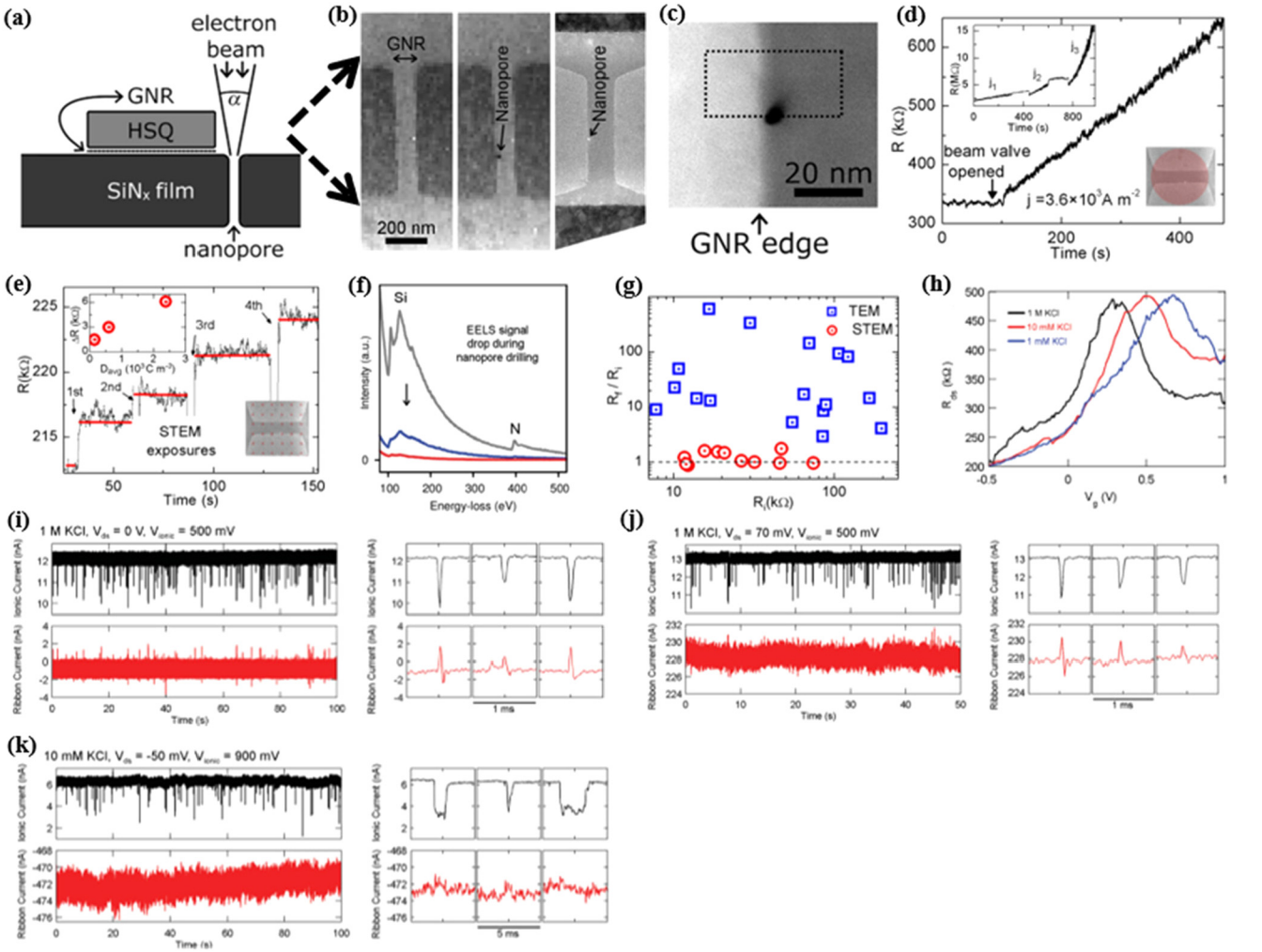

Fig. 17 (a) Cross-section of a GNR FET device with a nanopore through a SiN_x membrane close to GNR. Reprinted with permission from ref. 206. Copyright 2013, American Chemical Society. (b) High-angle annular dark field STEM images before (left) and after (middle) nanopore drilling with an electron probe, and a TEM image of GNR with a nanopore (right). Reprinted with permission from ref. 207. Copyright 2015, Wiley-VCH. (c) High-resolution high-angle annular dark field STEM image of the nanopore at the edge of GNR (this image was taken at 0.3 nm beam diameter). Reprinted with permission from ref. 206. Copyright 2013, American Chemical Society. (d and e) Variation of GNR resistance in TEM and STEM modes, respectively. Reprinted with permission from ref. 206. Copyright 2013, American Chemical Society. (f) EELS signals before (gray), during (blue), and after (red) nanopore formation. Si and N peaks at 100 and 400 eV, respectively. Reprinted with permission from ref. 207. Copyright 2015, Wiley-VCH. (g) Comparison of GNR resistance changes after nanopore preparation in TEM and STEM modes. Reprinted with permission from ref. 206. Copyright 2013, American Chemical Society. (h) Response of GNR to liquid gate voltage in KCl solutions with different concentrations. Reprinted with permission from ref. 207. Copyright 2015, Wiley-VCH. (i–k) The translocation of DNA with 15 000 base pairs measured under different ionic strengths, transmembrane voltages and source-drain voltages. Reprinted with permission from ref. 207. Copyright 2015, Wiley-VCH.

during nanopore formation. When the nanopore is fully formed and opened, the strength of the EELS Si peak would drop to zero, and if the residence time continues to increase, the nanopore size will further expand. EELS signals before (gray), during (blue), and after (red) nanopore formation are shown in Fig. 17(f).

Fig. 17(g) shows the relationship between the ratio of the final resistance to the initial resistance of GNRs (R_f/R_i) and the initial resistance (R_i) after nanopore preparation in two different modes (TEM and STEM). For nanopores prepared in TEM mode, the GNR resistance increases significantly, resulting in the abnormal use of most devices. Especially for GNR with a width of less than 50 nm, once the nanopore is formed, the device can no longer be conductive. In contrast, after nanopore preparation by STEM, the resistance of GNRs basically does not change, that is, $R_f/R_i \approx 1$, even for 50 nm wide GNRs. This huge difference is mainly due to the influence of irradiation dose during the preparation process. Fig. 17(c) shows a SEM image of the STEM prepared nanopore in an enlarged view. It can be seen that the nanopore was successfully prepared on the edge of GNR, and basically did not cause damage to GNR. The experiment also found that neither current annealing after the formation of the nanopore nor *in situ* annealing during the formation of the nanopore could

effectively regain or maintain the resistance of the initial GNR, which also occurred in the Si-based nanowire–nanopore FET sensor (after drilling, the formation gas annealing process is essential to restore the transistor characteristics). Fabrication of nanopores by sculpting causes irreversible damage to the channel material. Therefore, it is necessary to seek new methods for preparing nanopores to minimize or eliminate damage to channel materials.

The sensitivity (transconductance) of GNR can be characterized by measuring the response of GNR to the gate voltage of an ionic solution applied to the nanoribbon side of the SiN_x membrane. The bipolar gate response characteristics of GNR devices are shown in Fig. 17(h).[208] The detection sensitivity of GNR can be controlled by applying a gate voltage. In the region with the greatest GNR sensitivity, a uniform perturbation of ~10 mV applied to the nanoribbon would produce a current change of >50 nA (>1 μA baseline current); this is significantly higher than the GNR noise level ($I_{rms} \approx 12$ nA) at 1 MHz bandwidth in solution, indicating the GNR sensor has the ability to achieve DNA sequencing at high-bandwidth levels.

Fig. 17(i) and (k) shows the results of DNA translocation under different solution concentrations and source-drain voltage (V_{ds}), respectively. From Fig. 17(i), when V_{ds} is applied at 0 V, DNA translocation through the nanopore can still cause changes in the channel current of the nanoribbon, proving that crosstalk behavior occurs between GNR and the ionic current. With an increase of V_{ds}, both GNR current and noise increase, but the amplitude of crosstalk remains unchanged, that is, with an increase of V_{ds}, crosstalk becomes less obvious, as shown in Fig. 17(j). However, on the GNR side of the membrane, the SNR of crosstalk does not increase during the transition to low salt concentrations, and at a high nanoribbon baseline current, crosstalk is entangled with noise, as shown in Fig. 17(k). Combined with the experiments and circuit simulation results, it is found that the GNR crosstalk appears as the time derivative of the ionic current, $I_{electrode} = dq/dt = C_{electrode\text{-}soln} \times dV/dt$ (Fig. 17(i)–(k)). This crosstalk signals are independent of V_{ds} or ion concentration and are generated by capacitive coupling between GNR and ion measurement channels.

Although the capacitive coupling signal reveals the local presence of DNA in the nanopore, unlike the resistance modulation principle predicted by the simulation in GNR, the resulting current signals cause some interference to DNA sequencing, so these current signals are not desired. Based on previous research on GNR nanopore FET sensors,[203,206,207] in 2018, Heerema *et al.* made innovations with respect to two aspects,[188] to improve the detection sensitivity of the FET nanopore and to eliminate the influence of capacitive coupling signals of the FET nanopore. One is the characteristic size of GNR (previous theoretical work focused on GNR less than 10 nm wide, but previous experiments only explored the transmission characteristics of GNR that was 600 to 1000 nm long and 50 to 200 nm wide). In order to maintain the crystallinity of graphene and maximize the detection sensitivity, short and narrow (30 nm × 30 nm) nanoribbons with a 5 nm nanopore (the smaller the size, the more difficult to process, but the higher the detection sensitivity) were clearly defined on the suspended graphene membrane using high-temperature STEM. And the other is the GNR current signal measurement method. During testing, the capacitive current signal (capacitive coupling) and the resistive response (electrostatic gate voltage field effect control) in GNR were distinguished by using a custom differential current amplifier.

The whole preparation process for the GNR nanopore FET sensors is shown in Fig. 18(a). The substrate material for sensor preparation is a Si wafer with 500 nm thick SiN_x membrane, in which a platinum heater is embedded. Then, a 5 × 5 μm window of 100 nm thickness in the SiN_x membrane was obtained by through-membrane EBL and RIE.[209] Then, a 400 nm hole was prepared on the 100 nm thick SiN_x membrane and platinum electrodes were deposited near the hole (i). The hole is mainly used to suspend the graphene membrane so that suspended GNR can be obtained. The stripped graphene sheet (usually 10 × 10 μm) was transferred to the top of the SiN_x film (ii). After transfer, the graphene membrane was defined as a 200 × 200 nm square with four leads that were each in contact with a platinum electrode, by using EBL and oxygen plasma etching (iii). This structure ensures that the current can only pass through the graphene nanostructures. GNR of 30 × 30 nm in size was then prepared at 300–600 °C using high temperature STEM with high precision sculpting (iv). Heating is mainly used to prevent carbon deposition and maintain the crystallinity of graphene. The bottom row in Fig. 18(a) shows an example of performing the continuous sculpting steps in STEM. After STEM, a thin h-BN flake (3–7 layers) is transferred to the top of GNR as a support, more importantly, allowing DNA to translocate only through the nanopore (v). To prevent parasitic electrochemical currents during measurements, a thick (1.5 μm) polyimide layer is placed on top of the stack to cover the electrode, and then, a 10 μm uncovered area is opened by EBL (vi). If the electrode on the device were only partially coated, tens of nA of electrochemical leakage current would occur, while a complete polyimide layer on the chip would result in zero leakage current, as shown in Fig. 19(f). Finally, a 5 nm nanopore was drilled by STEM in the center of the GNR and h-BN multilayer film (vii). The final schematic diagram of the GNR nanopore FET sensor is shown in Fig. 18(b). Figure 18(c) and (d) shows the resistance and conductance distribution of GNRs (without nanopore) after sculpting, respectively. The relatively narrow GNRs after sculpting have lower conductivity than that of typical GNR, as shown in Fig. 18(d), probably because the graphene membrane is damaged during the nanopatterning process.[210]

After the successful preparation of the GNR nanopore FET, a custom differential current amplifier was used for experimental testing, which was able to distinguish between graphene current signals generated by capacitive coupling and signals generated by electrostatic gating or state density modulation. Fig. 19(b) and (c) explains the working principle of the differential current amplifier. GNR was divided into two symmetrical parts, centered around the nanopore, as shown in

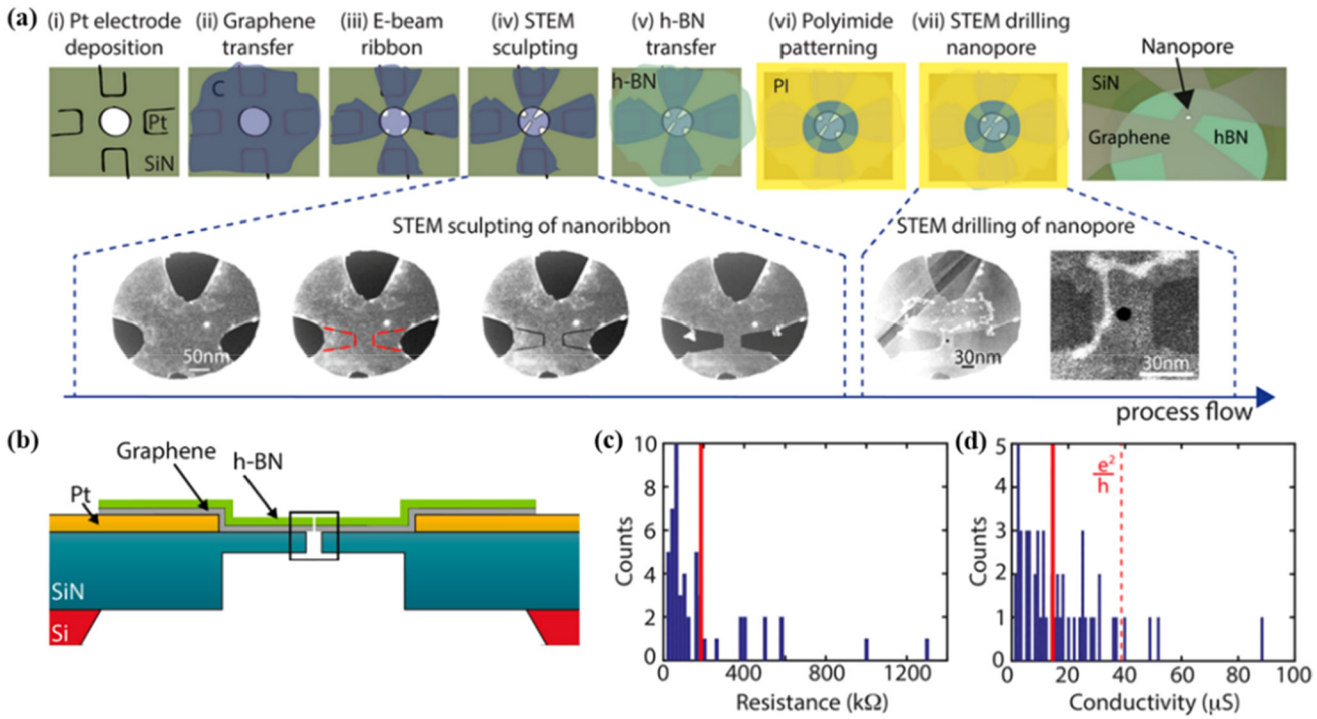

Fig. 18 Preparation process and characterization of a GNR nanopore FET sensor. (a) Detailed fabrication process for short and narrow GNR nanopore FET devices. (b) Schematic diagram of the GNR nanopore FET sensor. (c and d) Resistance and conductivity distributions of 51 GNRs before nanopore drilling. Reprinted with permission from ref. 188. Copyright 2018, American Chemical Society.

Fig. 19(b). The capacitance between the electrolyte and the graphene channel near the nanopore is denoted as C_g, and the capacitance coupled within a few microns of the nanopore is denoted as C_{lead}. Any local potential change at the nanopore ΔV_L is coupled with the capacitance C_g of the sensor to form the current $I_{c1,2} = C_g \times \frac{\Delta V_L}{\Delta t}$; potential changes that are not strongly localized at the nanopore, ΔV_{nl}, will generate a coupling current, $I_{c1,2} = (C_g + C_{lead}) \times \frac{\Delta V_L}{\Delta t}$. The coupling current is inherent in the nanopore FET sensor. During the test, the differential current amplifier applies opposite potentials to the two electrodes connected to GNR, as shown in Fig. 19(b). Because the capacitive current is independent of electrode potential, the sign is the same at both electrodes. In contrast, any resistance modulation results in the current signal being the opposite sign on each electrode. The differential current amplifier enables us to suppress common-mode signals and output differential mode signals during the test, as shown in Fig. 19(c). Thus, with this differential measurement, all capacitive contributions are eliminated, while retaining any contributions from resistance modulation.

In addition, Heerema *et al.* further explained the principle of differential current measurement through SPICE simulation, as shown in Fig. 19(g) and (h). In SPICE simulations, DNA events are simulated by 100 mV voltage steps lasting 1 ms, and the resistance modulation of GNR is simulated by a resistance increase lasting 1 ms. The current at each electrode is measured by a separate op-amp, each of which gives a unique signal. When the two current signals measured at the two electrodes are subtracted, the resulting differential current signal represents only the resistance modulation of GNR, while the addition of the two responses produces a capacitive signal, as shown in Fig. 19(h). These simulation results further verify the ability of the differential current amplifier to eliminate the coupled current signal during the experiment.

The equivalent circuit is shown in Fig. 19(a), the combination of V_{bias} (bias voltage of GNR) with V_{ion} and V_{lift} enables DNA sequencing to be performed at the highest transconductance (highest GNR sensitivity). At the same time, V_{com} readings can be used to monitor any leakage from the channel to the liquid. In DNA translocation experiments, 99.9% of translocation events were found to be fully synchronized in time, *i.e.* both the ion blocking signal and the GNR transverse current signal were detected, as shown in Fig. 19(d), and for most translocation events, no signal was detected in the common mode channel. The translocation of DNA leads to a temporary reduction in the resistance of GNR, because of electrostatic gate control, which includes two parts: the negative charges of the DNA backbone and the local potential change around the nanopore. Based on the transconductance and the magnitude of the graphene current change, the total potential change is estimated to be about −15 mV. The SNR in the GNR current is comparable to that in the ionic current (Fig. 19(e)); the SNRs of GNR current and ionic current are 4.2–4.5 and 3.8–5.4 respectively at 20–30 mV bias voltage.

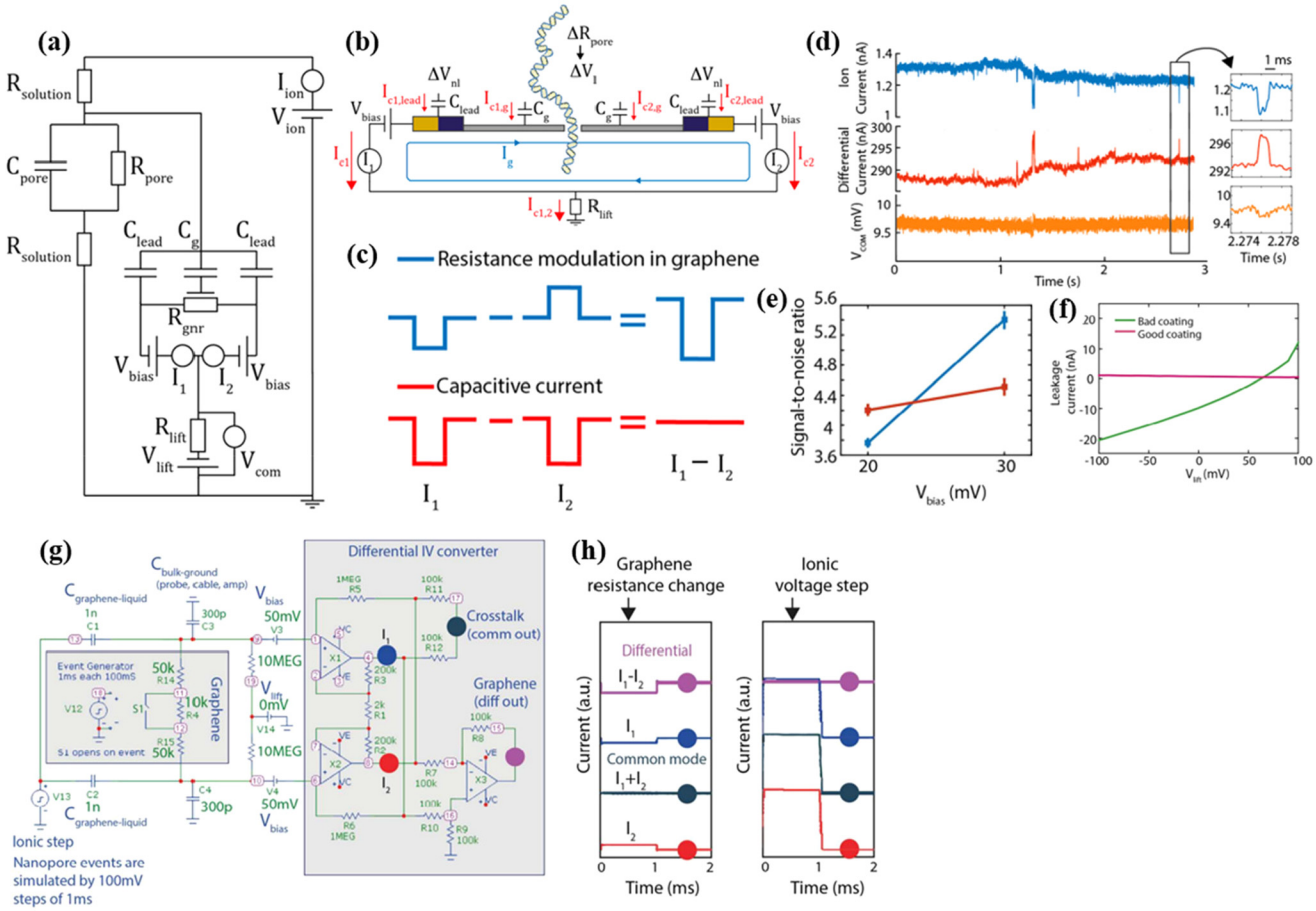

Fig. 19 Test circuit and analysis of test results. (a) Equivalent circuit of the setup. V_{lift} can be used to tune the gate voltage, V_{com} measures the direct current potential of graphene and monitors the leakage current. (b) During the test, the principles of capacitive coupling and electrostatic gate control, and how to exclude capacitive coupling signals. (c) Two kinds of signals are successfully distinguished based on the test in (b). (d) The simultaneous detection of three channels of ionic current (blue), graphene current (red) and common mode voltage (yellow); a magnified view of a DNA translocation event is shown in the right panel. (e) Signal-to-noise ratio *versus* bias voltage (red: graphene current; blue: ionic current). (f) The calculated leakage current *versus* V_{lift} after polyimide coating. (g and h) The working principle of a differential amplifier is demonstrated by Spice simulation, and further verifies the authenticity of eliminating coupling capacitance by a differential current amplifier in the experiment. Reprinted with permission from ref. 188. Copyright 2018, American Chemical Society.

As detailed previously, GNR nanopore FET sensors have led to significant advancements in the field of biomolecular detection. However, despite these successes, GNR nanopore FET sensors still encounter several critical challenges that need to be addressed.[40,80,173,211–215] For example, the graphene nanopore cannot be treated with oxygen plasma or piranha solution, so it is difficult to wet the nanopore during testing, resulting in base adhesion to the surface, causing blockage of the nanopore, and thus preventing DNA translocation. Luckily, there are some new two-dimensional materials such as MoS_2 and WS_2 that can be oxygen plasma treated to render the pore hydrophilic,[28,216] which do not cause blockage of the nanopore during testing. In 2014, Farimani *et al.* demonstrated the MoS_2 nanoribbon nanopore FET sensor as a promising sensor capable of transverse current detection and can be used for high-bandwidth DNA sequencing experiments, by MD and DFT simulations. The thickness of the single layer MoS_2 is ~1 nm, making it superior to the single layer graphene nanopore in terms of SNR, and the MoS_2 FET device is easy to prepare due to the presence of its inherent band gap.[186,197]

In 2019, Graf *et al.* prepared a MoS_2 nanoribbon nanopore FET sensor and successfully performed transverse current detection during DNA translocation.[164] The entire preparation process and final sensor structure of the MoS_2 nanoribbon nanopore FET sensor are shown in Fig. 20. Firstly, a 20 nm thick suspended SiN_x membrane was fabricated on a Si substrate by photolithography and wet etching with potassium hydroxide (KOH) solution (i). After that, a 50 nm–100 nm aperture was formed on the SiN_x membrane by EBL and RIE, which was used to suspend part of the MoS_2 (ii). The CVD grown single crystal MoS_2 layer was then wet-transferred to the hole of the SiN_x membrane (iii). After transfer, the Ti/Au contact electrode was prepared by EBL, electron beam assisted metal evaporation, and lift-off (iv). After that, the MoS_2 layer

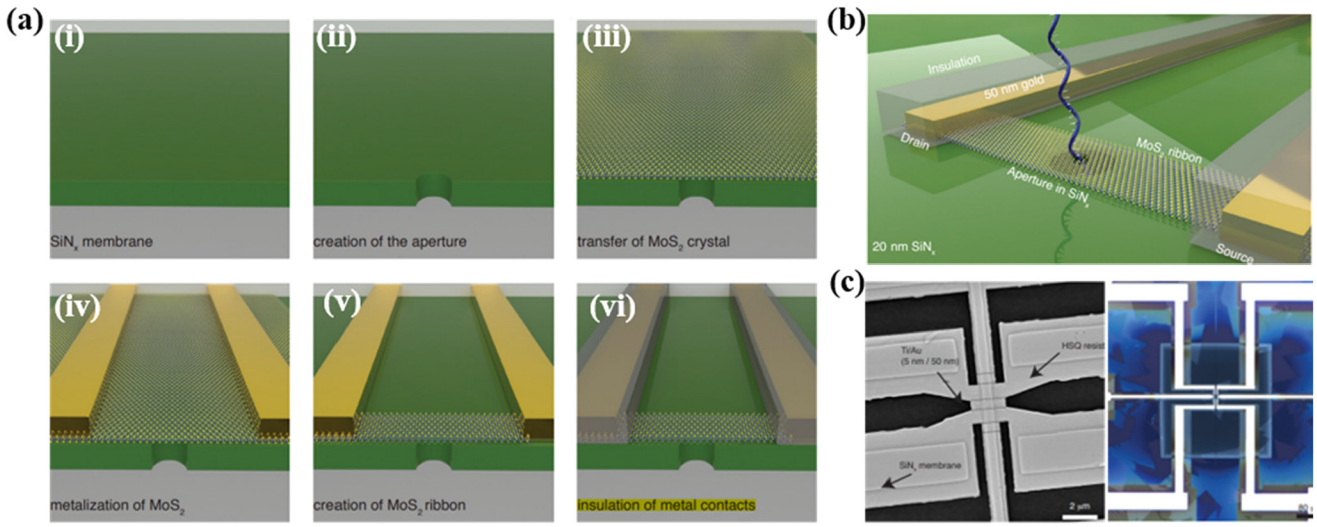

Fig. 20 Preparation process and final device structure of the MoS_2 nanoribbon nanopore FET sensor. (a) Detailed preparation process for the MoS_2 nanoribbon nanopore FET sensor. (i) A 20 nm thick suspended SiN_x membrane was fabricated. (ii) A 50 nm ~ 100 nm aperture was formed on the SiN_x membrane. (iii) MoS_2 layer was transferred. (iv) The Ti/Au contact electrode was prepared. (v) MoS_2 nanoribbons was prepared. (vi) A nanopore was formed by TEM. (b) Schematic of the proposed MoS_2 nanoribbon nanopore FET sensor. (c) TEM (left) and optical (right) images of the sensor. Reprinted with permission from ref. 164. Copyright 2019, American Chemical Society.

was patterned by EBL and RIE (O_2), and the characteristic size of the prepared MoS_2 nanoribbons was 50 nm wide and 2 μm long (v). EBL and ALD (20 nm thick HfO_2) were then used to selectively insulate the metal leads (vi). The 20 nm thick HfO_2 layer could limit crosstalk caused by capacitive coupling,[188] which has been described in detail previously. Insulating layer materials include but are not limited to Al_2O_3, HfO_2, SiN_x, and SiO_2.[163,190,203] Finally, TEM was used to drill a nanopore in the suspended portion of the MoS_2 nanoribbon, similar to the suspended graphene nanopore prepared by Heerema *et al.* This configuration can maximize the local potential change caused by DNA translocation.[217] The final schematic diagram of the MoS_2 nanoribbon nanopore FET sensor is shown in Fig. 20(b). Fig. 20(c) shows a TEM image and optical micrograph of the sensor.

The equivalent circuit of the MoS_2 nanoribbon nanopore FET sensor is shown in Fig. 21(a). Due to the limited stability of the freestanding MoS_2 nanoribbon, a nanopore was drilled in the MoS_2 nanoribbon supported by SiN_x for DNA molecular translocation testing. Fig. 21(b) shows the TEM image after nanopore preparation. To completely eliminate capacitance coupled crosstalk, a new test circuit based on differential amplifiers was proposed, as shown in Fig. 21(d), similar to the setup proposed by Heerema *et al.*,[188] but it was more complex, decoupling and electrically insulating the two circuits.

Translocation tests were performed on neutral, positively charged and negatively charged analytes in the nanopore with a diameter of ~2.5 nm. Fig. 21(e) shows DNA translocation, where relevant signals are simultaneously detected, and the negatively charged DNA molecule induces a decrease in the drain-source conductance of the n-type MoS_2 nanoribbon nanopore FET. When the neutral PEG molecule translocates, it causes a decrease in ionic conductance; however, most of the time no transverse signals are visible, as shown in Fig. 21(f). Finally, positively charged polylysine molecules were added, and it was found that positively charged polylysine translocation induced an increase in the drain-source conductance of the n-type MoS_2 nanoribbon nanopore FET, as shown in Fig. 21(g). As explained above, the crosstalk between the channel material and the ionic current generates a capacitive coupling signal; it is a time derivative signal that is disproportionate to the drop in ionic current.[207] And, electrostatic gating produces a field effect on the transistor that is proportional to the drop in ionic current.[163] Based on the analysis of translocations of three differently charged molecules, the changes to the FET channel current were caused by electrostatic gate control rather than capacitive coupling, moreover, direct charge sensing plays a dominant role,[188] as shown in Fig. 21(e)–(g).

The power spectral densities of ion channels and transverse channels under 1 M/1 M KCl and 10 mM/100 mM KCl test environments were plotted, as shown in Fig. 21(h). With a decrease in ion concentration, the noise on the transverse channels decreased. The median SNR for all 759 related events in Fig. 21(i) is 7.7 for the ionic current and 10.7 for the transverse current. The SNR of the transverse current is 40% higher than that of the ionic current, indicating the feasibility of transverse current measurement at higher bandwidth by using the MoS_2 nanoribbon nanopore FET sensor.

The two-dimensional material based FET nanopore sensor, as stated earlier, offers several compelling advantages for DNA translocation testing. Its high spatial resolution and sensitivity, coupled with a fast response time and high SNR, make it particularly suitable for DNA sequencing. In addition, its com-

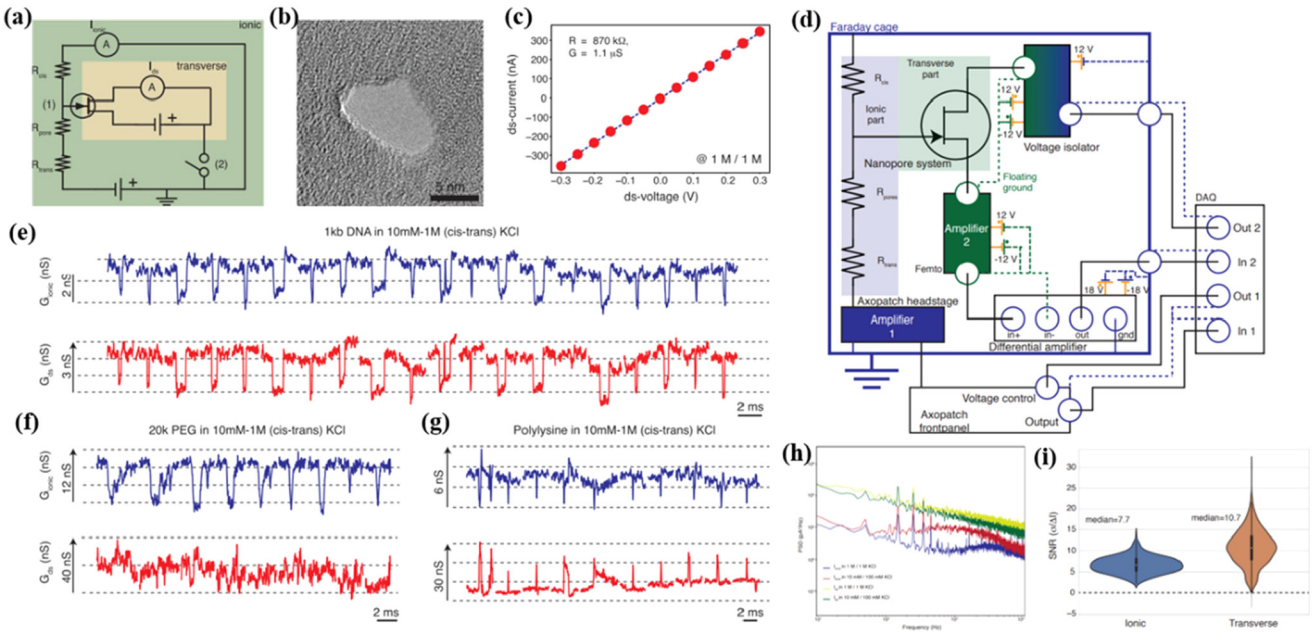

Fig. 21 Test circuit of the MoS_2 nanoribbon nanopore FET sensor and analysis of DNA translocation test results. (a) The equivalent electrical circuit of the MoS_2 nanoribbon nanopore FET sensor during DNA translocation. (b) A TEM image of the nanopore drilled through MoS_2 and the SiN_x membrane. (c) The *I*/*V* curve of the MoS_2 nanoribbon nanopore FET sensor in 1 M KCl solution. (d) Electrical setup. All components in this circuit are powered by a lead-acid battery placed in a Faraday cage. The core elements of the test circuit mainly include an amplifier, a differential amplifier and a voltage isolator. (e–g) Translocation detection of three differently charged molecules in 10 nM–1 M (*cis*–*trans*) solution (1 kbp dsDNA; PEG, mw = 20×10^3 g mol^{-1}; polylysine molecules). Both channels were sampled at 100 kHz and digitally low-pass filtered at 15 kHz. (h) Power spectral density of the ionic and transverse currents in 1 M/1 M KCl and 10 mM/100 mM KCl. (i) Boxplot of the signal to noise ratio of the ionic current and the transverse current. Reprinted with permission from ref. 164. Copyright 2019, American Chemical Society.

patibility with the CMOS process enhances its potential for integration into existing technologies. Furthermore, it is well suited for high-bandwidth testing during DNA translocations, enabling the analysis to be conducted without slowing down or limiting the speed of DNA molecules as they thread through the nanopore. Information about some representative FET nanopore sensors is summarized in Table 2, which contains the results of successfully prepared and successfully performed experimental DNA translocation tests. Several other 2D materials not listed below have been validated through first-principles density functional theory for DNA detection applications and hold promising prospects for nanopore FET sensors. Materials include borophene,[218] C_xN_y,[219] $Ti_2C(OH)_2$ MXene,[187] *etc*. Consequently, nanopore FET sensors based on these materials are not included in Table 2, mainly because they have not yet been experimentally verified.

Nanopore FET sensors, while highly promising for DNA sequencing compared with traditional solid-state nanopores, do face significant challenges that need to be addressed, mainly including preparation and detection. These challenges are critical to enhancing the robustness and reliability of nanopore FET sensors in practical applications.

Table 2 Summary of some representative experiments of FET nanopore sensors

Materials of the channel	Feature size	Mechanism	Multiplexing	Yield	SNR of FET	Gate electrode
Si nanowire prepared by CVD[163]	Length: <200 nm Width and thickness: ~30–50 nm	Local potential	Three channels	Low		No
Graphene[203]	Width: ~100 nm	DNA charge sensing	Single channel	22 devices (1/4)		No
Poly-crystalline Si[190]	Length: 260 nm Width: 50 nm Thickness: 2 nm/4 nm	Local potential	Single channel	Low		Side-gate
Graphene[207]	Length: 600 nm Width: 50–200 nm	Capacitive coupling	Single channel	Very low		No
Graphene[188]	Length: 30 nm Width: 30 nm	DNA charge sensing	Single channel	1/180	4.2–4.5	No
MoS_2 [164]	Length: 2 μm Width: 500 nm	DNA charge sensing	Single channel	3/200	4.2–4.5 (median)	No

The difficulties in preparation: (1) unlike traditional SSNs, which are characterized by simple fabrication processes and a short production period, the preparation of nanopore FET sensors involves a series of complex processes. These processes require multiple steps such as photolithography, EBL, ohmic contact formation, FIB, *etc*. As a result, the fabrication period is lengthy, the tolerance for errors is low, and thus the yield of devices is lower than that of traditional SSNs; (2) additionally, two-dimensional materials used in nanopore FET sensors, such as graphene, are susceptible to damage during the fabrication processes, necessitating extreme caution. For instance, graphene is sensitive to oxygen plasma, which complicates the process as avoiding oxygen plasma can lead to insufficient removal of organic contaminants, thereby further decreasing the yield of nanopore FET sensors. Currently, as described in Table 2, the yield of the device is very low; (3) furthermore, the use of FIB for nanopore preparation can cause irreversible damage to the channel material during nanopore formation, rendering the nanopore FET sensors incapable of exhibiting proper FET functionality. Even with post-processing treatments such as annealing, only partial restoration of FET performance is achievable. This significantly reduces the detection sensitivity of nanopore FET sensors.

The difficulties in detection: (1) as described above, the extremely low fabrication yield of nanopore FET sensors impedes sufficient testing data being obtained, thereby obstructing the accurate determination of the mechanisms of DNA translocation signals in nanopore FET sensors; (2) improving their signal-to-noise ratio and sensitivity; (3) and completely eliminating capacitive coupling.

Overcoming these issues is crucial for maximizing the performance and applicability of nanopore FET sensors in practical settings. Detailed strategies and methods for addressing these challenges are discussed in the following section, and insights into potential improvements and innovations in this field are offered.

3.3.4 Improved nanopore FET sensors. Many theoretical and computational studies on the transport of two-dimensional materials shaped as a constriction or quantum point contact (QPC) containing a nanopore show that the presence of DNA bases inside the nanopore can lead to current changes in the nanostructure of the two-dimensional material based on base-specific modulation, so DNA sequencing can be achieved as DNA threads through the nanopore.[180–187,192–196] However, during experimental testing, the operation of an actual biosensor will involve the underlying substrate (usually SiO_2 or SiN_x, suspended two-dimensional materials), a solvent, the DNA counterion,[220] and most importantly, fluctuation of the DNA structure, not all of these factors are taken into account in simulations. Although significant advancements have been made in the field of nanopore FET sensors, until now, nanopore FET experiments have not been able to detect transverse current changes caused by non-electrostatic base-specific interactions between DNA bases and nanostructures. To fully realize the potential of DNA sequencing using nanopore FET sensors, several issues need to be resolved. This involves improving the sensitivity and specificity of the interactions between the DNA bases and the nanostructures, ensuring accurate and reliable sequencing can be achieved as DNA molecules pass through the nanopores.

3.3.4.1 Improve the yield of the nanopore FET sensors. Nanopore FET sensors face major challenges due to their low fabrication yield. As a result, the detection mechanism of nanopore FET sensors cannot be explored in detail. To address this problem, there is an urgent need to develop and explore new preparation processes or optimize existing preparation processes, explore new two-dimensional materials that are easy to process and of high quality,[187] improve nanopore fabrication methods and precision, and prevent contamination during the sensor preparation process. These steps are essential for enhancing the yield and effectiveness of nanopore FET sensors.

3.3.4.2 Improve SNR and detection sensitivity. FET nanopores with high SNR are critical in DNA sequencing. A high SNR can notably improve the ability to identify single molecule events, reduce misjudgments and omissions, reduce experimental errors, and improve detection sensitivity. Until now, DNA sequencing has not been possible with SSNs, a major obstacle being the low SNR due to the thermal fluctuations of DNA bases, ions, and water inside SSNs. In particular, the noise from conformational changes in the DNA structure within the nanopore may overshadow the signal induced by each nucleotide, thus significantly diminishing the detection sensitivity of nanopore FET sensors.

In 2016, Hu Qiu *et al.* proposed a new nanopore FET sensor structure that could be used for electrical regulation, and verified by molecular dynamics simulations; this can further enhance the SNR and detection sensitivity of nanopore FET sensors. The device structure is shown in Fig. 22(a).[221] Compared with the original nanopore FET sensor, the structure has an additional metal layer, which can be used to control DNA molecular motion, and the metal layer is isolated from the channel sensing material by an insulating layer (SiO_2, SiN_x, Al_2O_3, HfO_2, *etc*.). When the control voltage (V_c) is applied to the metal layer (−0.75 V to 0.75 V), it creates an electrostatic field within the nanopore (Fig. 22(c)), which in turn affects the conformation and random fluctuations of the DNA molecule, as shown in Fig. 22(b). At different V_c, the centroid positions of DNA passing through the nanopore were recorded as shown in Fig. 22(d) and (e). According to Fig. 22(d), it can be seen that with an increase of the applied positive bias, the centroid position of DNA becomes more localized around a specific position in the pore, indicating damping of the DNA motion around a stable conformation. The larger positive voltage more strongly reduces the movement of the DNA molecule, mainly because of electrostatic attraction between the positively charged pore surface and the negatively charged DNA backbone. When a negative voltage is applied, the fluctuation of DNA is still large, as shown in Fig. 22(e). Mainly due to the strong repulsion between the negatively charged pore surface and the DNA backbone, DNA is significantly compressed in the lateral direction, as shown in Fig. 22(b) (right panel).

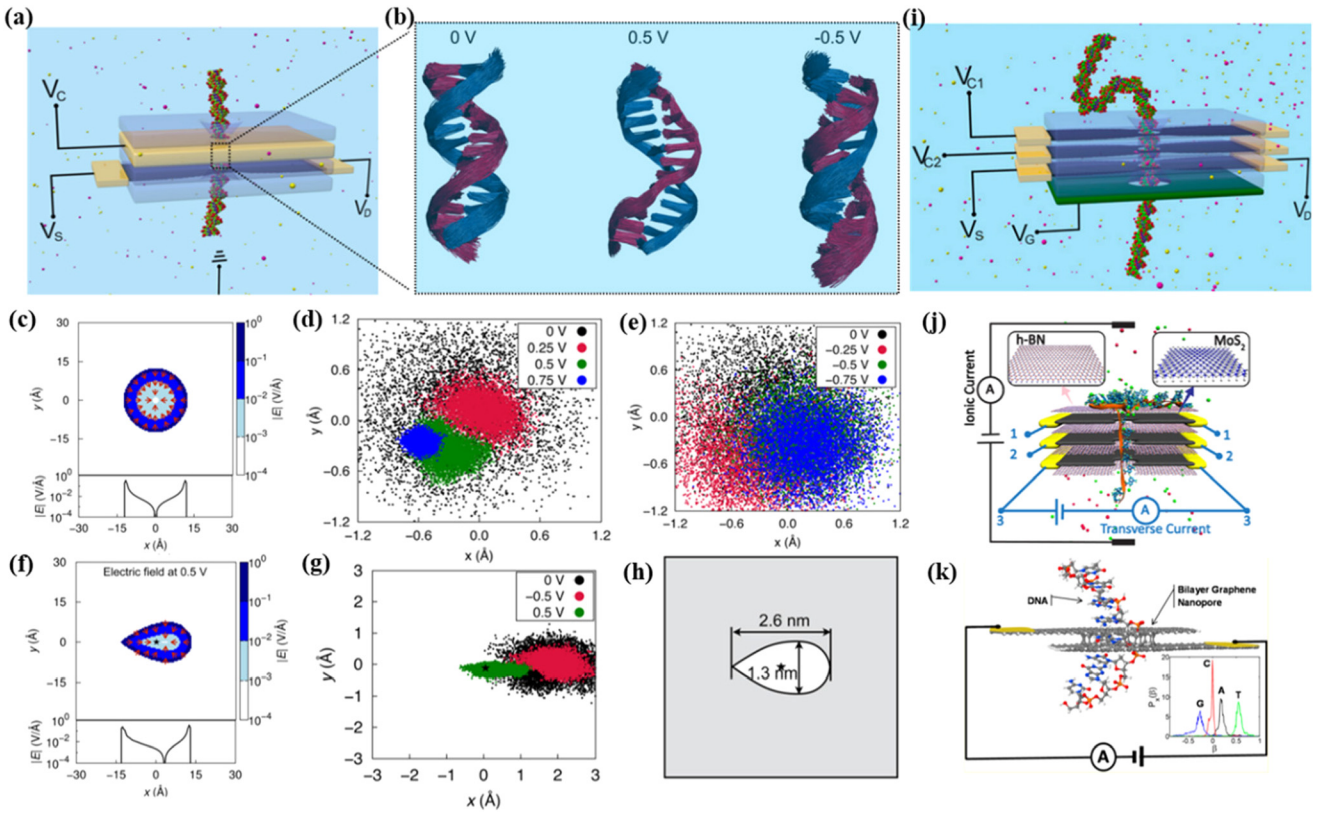

Fig. 22 (a) Schematic of a multilayer FET prototype with a nanopore for DNA translocation control and detection. The metal control layer is used to apply the control voltage (V_c, yellow) and is isolated from the channel material by an insulating oxide layer (blue). Channel bias at V_D and V_S is used to detect translocations of DNA molecules. The system is biased with respect to a common ground. Reprinted with permission from ref. 221. Copyright 2016, American Chemical Society. (b) Overlapping DNA conformations at 10 ps intervals on 5 ns MD tracks at 0 (left), 0.5 (middle), −0.5 V (right) voltage bias. Reprinted with permission from ref. 221. Copyright 2016, American Chemical Society. (c) The magnitude of the electric field of a cylindrical nanopore at a bias voltage of 0.5 V. Reprinted with permission from ref. 221. Copyright 2016, American Chemical Society. (d and e) Scatter plots of mass positions of dsDNA under different applied control voltages. Reprinted with permission from ref. 221. Copyright 2016, American Chemical Society. (f) The magnitude of the electric field of a teardrop-shaped nanopore at a bias voltage of 0.5 V. Reprinted with permission from ref. 221. Copyright 2016, American Chemical Society. (g) Scatter plot of mass positions of dsDNA under different applied control voltages upon translocation through the teardrop-shaped nanopore. Reprinted with permission from ref. 221. Copyright 2016, American Chemical Society. (h) The geometry and size of the teardrop nanopore. Reprinted with permission from ref. 221. Copyright 2016, American Chemical Society. (i) More complex four-layer FET nanopore structure. The top layer V_{c1} is used to control the translocation speed of DNA, the second layer V_{c2} is used to control the lateral confinement of DNA, and the third layer V_{ds} is used to detect the transverse current. Finally, the gate voltage (V_g) is used to regulate the detection sensitivity. Reprinted with permission from ref. 194. Copyright 2013, National Academy of Sciences. (j) FET nanopore sensors are stacked with three-layer MoS_2 insulated by an h-BN monolayer. Reprinted with permission from ref. 195. Copyright 2023, American Chemical Society. (k) Vertical bilayer graphene nanopores; DNA translocation through carbon atomic orbitals causes a change in the source-drain current. Reprinted with permission from ref. 222. Copyright 2014, American Chemical Society.

By applying V_c and changing the shape of the nanopore, it is found that the distribution of electric field in the nanopore can be coordinated to control the thermal fluctuation of DNA. A teardrop-shaped nanopore, as depicted in Fig. 22(h), demonstrated a unique electric field distribution (Fig. 22(f)), with a slower decay of field intensity at the teardrop tip. This structure influenced DNA's centroid position during translocation under different V_c conditions (Fig. 22(g)). Notably, under positive bias, DNA exhibited a slight shift towards the pore tip. This movement is largely attributed to the higher electric field intensity and slower decay at the tip, suggesting a synergistic interplay between the nanopore shape and electric field in controlling DNA behavior.

The synergistic utilization of gate voltage and control voltage can also further enhance detection sensitivity on the basis of improving the SNR. By applying a gate voltage to change the Fermi level of the channel material, and then change the carrier concentration, finally, the transconductance of the channel is controlled, achieving the highest sensitivity detection;[184,187,211] the sensor structure is shown in Fig. 22(i). In the experiment, in addition to adjusting the detection sensitivity of the nanopore FET sensor by applying a gate voltage, the detection sensitivity can also be improved by reducing the characteristic size (width and length) of the FET channel and the diameter of the nanopore. Currently, the minimum characteristic sizes of the nanopore FET sensor is width = 30 nm (ref.

188) and L = 10 nm.[41] With the maturation and continuous development of processing technology, there is still plenty of room for further reduction. Besides size, the SNR and detection sensitivity can also be improved through more complex vertical multilayer nanopore FET structures, as shown in Fig. 22(j) and (k).[222] Different from the conformational fluctuations of translocation molecules quenched through electrical control by Qiu *et al.*, when biomolecules translocate through multilayer membranes, conformational fluctuations will naturally be quenched and the SNR will be greatly improved.[221] This approach offers a promising and simple alternative to voltage control. Furthermore, it is not necessary to precisely control the electric field inside the nanopore to quench the DNA molecular configuration fluctuations.

3.3.4.3 Eliminating capacitive coupling. When nanopore FET sensors are used for DNA translocation testing, part of the transverse current signal comes from the capacitive coupling effect between the channel material and the ion channel, and the capacitive coupling signal is independent of the source-drain voltage and ion concentration. Unluckily, during the test process, the capacitive coupling signal is inherent and can only be eliminated by subsequent test circuits. Although the capacitive coupling signal reveals the local presence of DNA around the nanopore, unlike the resistance modulation principle predicted by the simulations for GNR, the resulting current signal has an adverse effect on DNA sequencing. In order to completely eliminate the effect of the capacitive current during DNA sequencing, a differential current amplifier needs to be used for translocation testing. During translocation, the differential current amplifier is able to distinguish between a capacitive current signal generated by capacitive coupling and a resistive current signal generated by electrostatic gating or state density modulation.[164,188] Therefore, to completely eliminate the effect of capacitive coupling, more complex differential current amplifiers and test circuits should be explored and used.[223,224]

4. Conclusion and outlook

In this review, the development history, detection principle, preparation methods and application scenarios of traditional SSNs were first discussed. The ultimate goal of traditional SSNs is to enable rapid, low-cost DNA sequencing for individuals. Nevertheless, traditional SSNs still encounter substantial challenges in DNA sequencing. Firstly, compared with biological nanopores, the pore size of traditional SSNs cannot be engineered as accurately or manufactured as reproducibly, because variations in the dimensions and geometrical characteristics of SSNs arise when employing different fabrication methods. Secondly, the SNR of traditional SSNs is considerably low, which seriously hinders high-bandwidth testing during translocation, resulting in some effective signal loss. Thirdly, to achieve parallel addressable DNA translocation experiments with traditional SSNs, an extremely complex microfluidic system is required. These challenges significantly restrict the practical application of traditional SSNs in DNA sequencing.

To overcome the obstacles faced by traditional SSNs, some innovative detection mechanisms have been proposed, including optical detection, tunneling current detection, and nanopore FET detection. Optical detection, while effective, requires complex optical systems, which hinder the portability of DNA sequencing. Tunneling current detection demands high precision in device fabrication, requiring the accurate placement of metal electrode pairs near the nanopore, which is challenging for mass production. The nanopore FET method, being CMOS compatible, offers advantages in terms of miniaturization and large-scale integration, making it a promising approach for DNA sequencing. The nanopore FET sensor, combining nanopore technology with FET sensing, is an advanced biological detection tool. The development of a nanopore FET sensor is mainly focused on traditional Si materials and novel two-dimensional materials like graphene and MoS_2. Compared to traditional ionic current blocking detection, nanopore FET detection offers tremendous advantages. To begin with, nanopore FET sensors exhibit a relatively high baseline current (μA) during testing, with a flat high-frequency response and superior SNR, facilitating high-bandwidth testing that traditional SSNs cannot realize. Next, the fabrication of nanopore FET sensors is compatible with CMOS processes, enabling integration and miniaturization to be achieved. Furthermore, nanopore FET sensors can be used for multiplexing within a single analytical chamber, removing the need for complex microfluidic systems.

Despite the fact that nanopore FET sensors have addressed several limitations inherent to traditional SSN DNA sequencing, nanopore FET sensors still face considerable challenges in terms of fabrication and testing. Firstly, the preparation process for nanopore FET sensors is much more difficult than that of SSNs, leading to the extremely low yield of nanopore FET sensors, so it is impossible to investigate the DNA sequencing mechanism in detail under these conditions. Secondly, in the testing process, the changes in transverse current induced by capacitive coupling result in interference during DNA sequencing, impacting the accuracy and reliability of the results. Thirdly, the SNR of nanopore FET sensors needs to be further enhanced. Finally, it is imperative to further diminish the dimensions of the channel, aiming to achieve a size of less than 10 nm in both length and width, to further enhance the detection sensitivity of the sensor.

Recent investigations combined with molecular dynamics simulations have elucidated that the type, shape, and feature size (width, length, and thickness) of the channel material, as well as the size, position, and shape of the nanopore, coupled with the presence of any defects at the nanopore boundary, substantially influence the sensitivity of the sensor.[194,211,225] Consequently, future developments of nanopore FET sensors are anticipated to follow these directions:

(1) Improving the fabrication methods for two-dimensional material based nanopore FET sensors to elevate the yield. And further facilitate more comprehensive exploration of the detection mechanisms of these sensors.

(2) Investigating novel two-dimensional materials that are not only easier to process but also enhance detection sensi-

tivity. Establishing a foundation for the large-scale integration and preparation of nanopore FET sensors.

(3) By using more complex differential current amplifiers and low noise test circuit systems to entirely eliminate capacitive coupled signals and improve resistance modulated signals.

(4) Developing nanopore FET sensors with innovative structures such as vertical multi-channel configurations, multiple gate voltage regulation, two-dimensional material heterojunctions and so on.

(5) Continued optimization of traditional silicon-based nanopore FET sensors is essential, mainly to enhance their spatial resolution and SNRs. Utilizing the maturity of fabrication processes for improved yield, miniaturization, and integration with other advanced devices.

(6) During the manufacturing process, the characteristic dimensions of the channel material, including width, length, and thickness, as well as the diameter of the nanopore, should be reduced to match the simulated dimensions to optimize and maximize the detection sensitivity of the sensors.

In conclusion, nanopore FET technology is increasingly recognized as a powerful platform for achieving DNA sequencing. With the swift progression in micro- and nanofabrication technologies, coupled with ongoing enhancements in detection theories, the feasibility for rapid, economical DNA sequencing *via* nanopore FET sensors is progressively attainable. This approach promises to fundamentally transform DNA sequencing, providing high-speed and cost-efficient solutions.

Author contributions

Jiangtao Wei: writing – the original draft. Xing Wang and Hao Hong: writing review and editing. Xin Lei and Minjie Ye: investigation and writing – review and editing. Zewen Liu: conceptualization, supervision and writing – review and editing.

Data availability

No primary research results, software or code have been included and no new data were generated or analysed as part of this review.

Conflicts of interest

The authors declare no conflict of interest.

Acknowledgements

This research was supported by the Beijing Innovation Center for Future Chips, Beijing National Research Center for Information, and the National Key R&D Program (2019YFA0707002).

References

1 M. Wanunu, Nanopores: A Journey Towards DNA Sequencing, *Phys. Life Rev.*, 2012, **9**, 125–158.
2 A. Parsegian, Energy of an Ion Crossing a Low Dielectric Membrane: Solutions to Four Relevant Electrostatic Problems, *Nature*, 1969, **221**, 844–846.
3 J. Hurley, Sizing Particles with a Coulter Counter, *Biophys. J.*, 1970, **10**, 74–79.
4 J. E. Hall, Access Resistance of a Small Circular Pore, *J. Gen. Physiol.*, 1975, **66**, 531–532.
5 R. W. DeBlois, C. P. Bean and R. K. A. Wesley, Electrokinetic Measurements with Submicron Particles and Pores by the Resistive Pulse Technique, *J. Colloid Interface Sci.*, 1977, **61**, 323–335.
6 W. Sung and P. J. Park, Polymer Translocation through a Pore in a Membrane, *Phys. Rev. Lett.*, 1996, **77**, 783–786.
7 C. Wei, A. J. Bard and S. W. Feldberg, Current Rectification at Quartz Nanopipet Electrodes, *Anal. Chem.*, 1997, **69**, 4627–4633.
8 P. J. Park and W. Sung, Polymer Translocation Induced by Adsorption, *J. Chem. Phys.*, 1998, **108**, 3013–3018.
9 J. Han, S. W. Turner and H. G. Craighead, Entropic Trapping and Escape of Long DNA Molecules at Submicron Size Constriction, *Phys. Rev. Lett.*, 1999, **83**, 1688–1691.
10 M. Muthukumar, Polymer Translocation through a Hole, *J. Chem. Phys.*, 1999, **111**, 10371–10374.
11 J. J. Nakane, M. Akeson and A. Marziali, Nanopore Sensors for Nucleic Acid Analysis, *J. Phys.: Condens. Matter*, 2003, **15**, R1365–R93.
12 A. J. Storm, J. H. Chen, X. S. Ling, H. W. Zandbergen and C. Dekker, Fabrication of Solid-State Nanopores with Single-Nanometre Precision, *Nat. Mater.*, 2003, **2**, 537–540.
13 J. B. Heng, C. Ho, T. Kim, R. Timp, A. Aksimentiev, Y. V. Grinkova, *et al.*, Sizing DNA Using a Nanometer-Diameter Pore, *Biophys. J.*, 2004, **87**, 2905–2911.
14 M. Tsutsui, K. Yokota, T. Nakada, A. Arima, W. Tonomura, M. Taniguchi, *et al.*, Silicon Substrate Effects on Ionic Current Blockade in Solid-State Nanopores, *Nanoscale*, 2019, **11**, 4190–4197.
15 D. Verschueren, X. Shi and C. Dekker, Nano-Optical Tweezing of Single Proteins in Plasmonic Nanopores, *Small Methods*, 2019, **3**, 1800465.
16 J. D. Spitzberg, A. Zrehen, X. F. van Kooten and A. Meller, Plasmonic-Nanopore Biosensors for Superior Single-Molecule Detection, *Adv. Mater.*, 2019, **31**, 1900422.
17 J. Buchheim, K.-P. Schlichting, R. M. Wyss and H. G. Park, Assessing the Thickness–Permeation Paradigm in Nanoporous Membranes, *ACS Nano*, 2019, **13**, 134–142.
18 K. Chen, J. Kong, J. Zhu, N. Ermann, P. Predki and U. F. Keyser, Digital Data Storage Using DNA Nanostructures and Solid-State Nanopores, *Nano Lett.*, 2019, **19**, 1210–1215.
19 N. Athreya, A. Khandelwal, X. Li and J.-P. Leburton, Electrically Controlled Nanofluidic DNA Sluice for Data

Storage Applications, *ACS Appl. Nano Mater.*, 2021, **4**, 11063–11069.
20 D. Pandey, P. K. Mondal and S. Wongwises, Chemiosomotic Flow in a Soft Conical Nanopore: Harvesting Enhanced Blue Energy, *Soft Matter*, 2023, **19**, 1152–1163.
21 M. Tsutsui, K. Yokota, I. W. Leong, Y. He and T. Kawai, Sparse Multi-Nanopore Osmotic Power Generators, *Cell Rep. Phys. Sci.*, 2022, **3**, 101065.
22 M. C. Acharjee, H. Li, R. Rollings, B. Ma, S. Tung and J. Li, Tau and Tubulin Protein Aggregation Characterization by Solid-State Nanopore Method and Atomic Force Microscopy, *J. Appl. Phys.*, 2023, **133**, 024701.
23 A. Rutkowska, K. Freedman, J. Skalkowska, M. J. Kim, J. B. Edel and T. Albrecht, Electrodeposition and Bipolar Effects in Metallized Nanopores and Their Use in the Detection of Insulin, *Anal. Chem.*, 2015, **87**, 2337–2344.
24 P. Xia, M. A. Rahman Laskar and C. Wang, Wafer-Scale Fabrication of Uniform, Micrometer-Sized, Triangular Membranes on Sapphire for High-Speed Protein Sensing in a Nanopore, *ACS Appl. Mater. Interfaces*, 2023, **15**, 2656–2664.
25 L. Xu, R. A. Rymzhanov, P. Zhai, S. Zhang, P. Hu, X. Meng, *et al.*, Direct Fabrication of Sub-10 nm Nanopores in WO_3 Nanosheets Using Single Swift Heavy Ions, *Nano Lett.*, 2023, **23**, 4502–4509.
26 C. Huang, Z. Li, X. Zhu, X. Ma, N. Li and J. Fan, Two Detection Modes of Nanoslit Sensing Based on Planar Heterostructure of Graphene/Hexagonal Boron Nitride, *ACS Nano*, 2023, **17**, 3301–3312.
27 L. F. Villalobos, D. J. Babu, K.-J. Hsu, C. Van Goethem and K. V. Agrawal, Gas Separation Membranes with Atom-Thick Nanopores: The Potential of Nanoporous Single-Layer Graphene, *Acc. Mater. Res.*, 2022, **3**, 1073–1087.
28 M. Macha, S. Marion, M. Tripathi, M. Thakur, M. Lihter, A. Kis, *et al.*, High-Throughput Nanopore Fabrication and Classification Using Xe-Ion Irradiation and Automated Pore-Edge Analysis, *ACS Nano*, 2022, **16**, 16249–16259.
29 Z. Cao, P. Yadav and A. Barati Farimani, Which 2D Material is Better for DNA Detection: Graphene, MoS_2, or MXene?, *Nano Lett.*, 2022, **22**, 7874–7881.
30 S. Pal, A. Naik, A. Rao, B. Chakraborty and M. M. Varma, Aptamer-DNA Origami-Functionalized Solid-State Nanopores for Single-Molecule Sensing of G-Quadruplex Formation, *ACS Appl. Nano Mater.*, 2022, **5**, 8804–8810.
31 T. Ding, J. Yang, J. Wang, V. Pan, Z. Lu, Y. Ke, *et al.*, Shaped DNA Origami Carrier Nanopore Translocation Influenced by Aptamer Based Surface Modification, *Biosens. Bioelectron.*, 2022, **195**, 113658.
32 M.-Y. Wu, D. Krapf, M. Zandbergen, H. Zandbergen and P. E. Batson, Formation of Nanopores in a SiN/SiO_2 Membrane with an Electron Beam, *Appl. Phys. Lett.*, 2005, **87**, 113106.
33 M. J. Kim, B. McNally, K. Murata and A. Meller, Characteristics of Solid-State Nanometre Pores Fabricated Using a Transmission Electron Microscope, *Nanotechnology*, 2007, **18**, 205302.
34 D. G. Howitt, S. J. Chen, B. C. Gierhart, R. L. Smith and S. D. Collins, The Electron Beam Hole Drilling of Silicon Nitride Thin Films, *J. Appl. Phys.*, 2008, **103**, 024310.
35 H. Kwok, K. Briggs and V. Tabard-Cossa, Nanopore Fabrication by Controlled Dielectric Breakdown, *PLoS One*, 2014, **9**, e92880.
36 C. Ying, J. Houghtaling, O. M. Eggenberger, A. Guha, P. Nirmalraj, S. Awasthi, *et al.*, Formation of Single Nanopores with Diameters of 20–50 nm in Silicon Nitride Membranes Using Laser-Assisted Controlled Breakdown, *ACS Nano*, 2018, **12**, 11458–11470.
37 Y. Zhang, Y. Miyahara, N. Derriche, W. Yang, K. Yazda, X. Capaldi, *et al.*, Nanopore Formation via Tip-Controlled Local Breakdown Using an Atomic Force Microscope, *Small Methods*, 2019, **3**, 1900147.
38 Z. Xia, A. Scott, R. Keneipp, J. Chen, D. J. Niedzwiecki, B. DiPaolo, *et al.*, Silicon Nitride Nanopores Formed by Simple Chemical Etching: DNA Translocations and TEM Imaging, *ACS Nano*, 2022, **16**, 18648–18657.
39 S. Mittal, M. K. Jena and B. Pathak, Amplifying Quantum Tunneling Current Sensitivity through Labeling Nucleotides Using Graphene Nanogap Electrodes, *ACS Appl. Nano Mater.*, 2022, **5**, 9356–9366.
40 A. S. Verhulst, D. Ruić, K. Willems and P. V. Dorpe, Boosting the Sensitivity of the Nanopore Field-Effect Transistor to Translocating Single Molecules, *IEEE Sens. J.*, 2022, **22**, 5732–5742.
41 X. Zhu, X. Li, C. Gu, Z. Ye, Z. Cao, X. Zhang, *et al.*, Monolithic Integration of Vertical Thin-Film Transistors in Nanopores for Charge Sensing of Single Biomolecules, *ACS Nano*, 2021, **15**, 9882–9889.
42 J. P. Fried, Y. Wu, R. D. Tilley and J. J. Gooding, Optical Nanopore Sensors for Quantitative Analysis, *Nano Lett.*, 2022, **22**, 869–880.
43 J. Wang, L. Luo, Y. Li, L. Chen, C. Gui, J. Zhu, *et al.*, A Signal on–off Strategy Based on the Digestion of DNA Cubes Assisted by the CRISPR–Cas12a System for Ultrasensitive HBV Detection in Solid-State Nanopores, *Analyst*, 2022, **147**, 5623–5632.
44 H. Kang, H. Joo, J. Choi, Y.-J. Kim, Y. Lee, S.-Y. Cho, *et al.*, Top-Down Approaches for 10 nm-Scale Nanochannel: Toward Exceptional H_2S Detection, *ACS Nano*, 2022, **16**, 17210–17219.
45 G. Di Muccio, B. Morozzo della Rocca and M. Chinappi, Geometrically Induced Selectivity and Unidirectional Electroosmosis in Uncharged Nanopores, *ACS Nano*, 2022, **16**, 8716–8728.
46 A. Gubbiotti, M. Chinappi and C. M. Casciola, Confinement Effects on the Dynamics of a Rigid Particle in a Nanochannel, *Phys. Rev. E*, 2019, **100**, 053307.
47 B. Cao, E. Xu and T. Li, Anomalous Stability of Two-Dimensional Ice Confined in Hydrophobic Nanopores, *ACS Nano*, 2019, **13**, 4712–4719.
48 Y. Xu, R. Yazbeck and C. Duan, Anomalous Mechanosensitive Ion Transport in Nanoparticle-Blocked Nanopores, *J. Chem. Phys.*, 2021, **154**, 224702.

49 X. Shi, A.-K. Pumm, J. Isensee, W. Zhao, D. Verschueren, A. Martin-Gonzalez, *et al.*, Sustained Unidirectional Rotation of a Self-Organized DNA Rotor on a Nanopore, *Nat. Phys.*, 2022, **18**, 1105–1111.
50 C. Ding and J. Su, Promoting Desalination Performance of Carbon Nanotubes Through Cationic and Anionic Surface Modifications, *Appl. Surf. Sci.*, 2023, **607**, 154971.
51 D. Song, L. Li, C. Huang and K. Wang, Synergy Between Ionic Thermoelectric Conversion and Nanofluidic Reverse Electrodialysis for High Power Density Generation, *Appl. Energy*, 2023, **334**, 120681.
52 S. Paul, W.-L. Hsu, Y. Ito and H. Daiguji, Boiling in Nanopores through Localized Joule Heating: Transition between Nucleate and Film Boiling, *Phys. Rev. Res.*, 2022, **4**, 043110.
53 L. Liang, F. Qin, S. Wang, J. Wu, R. Li, Z. Wang, *et al.*, Overview of the Materials Design And Sensing Strategies of Nanopore Devices, *Coord. Chem. Rev.*, 2023, **478**, 214998.
54 Z. Zhao, Z. Guo, Z. Zhang, X. Gui, Z. Liang, J. Liu, *et al.*, Single Graphene Nanopore for Biomimetic Ion Channel Via Tunably Voltage-Modulated Ion Transport, *Carbon*, 2023, **203**, 172–180.
55 Y.-S. Su, W.-H. Hung, A. R. Fauziah, Z. S. Siwy and L.-H. Yeh, A pH Gradient Induced Rectification Inversion in Asymmetric Nanochannels Leads to Remarkably Improved Osmotic Power, *Chem. Eng. J.*, 2023, **456**, 141064.
56 R. Song, H. Zeng, S. Zhang, Y. Wang, X. Han, X. Chen, *et al.*, Low-Frequency Flicker Noise in Stochastic Ionic Transport Across Atomically Thin Graphene Nanopores, *Cell Rep. Phys. Sci.*, 2023, **4**, 101210.
57 X. Guan, H. Li, L. Chen, G. Qi and Y. Jin, Glass Capillary-Based Nanopores for Single Molecule/Single Cell Detection, *ACS Sens.*, 2023, **8**, 427–442.
58 J. Zhu, F. Bošković and U. F. Keyser, Split G-Quadruplexes Enhance Nanopore Signals for Simultaneous Identification of Multiple Nucleic Acids, *Nano Lett.*, 2022, **22**, 4993–4998.
59 Y. Zhao, M. Iarossi, A. F. De Fazio, J.-A. Huang and F. D. Angelis, Label-Free Optical Analysis of Biomolecules in Solid-State Nanopores: Toward Single-Molecule Protein Sequencing, *ACS Photonics*, 2022, **9**, 730–742.
60 X. Zhang, M. Xu, J. Yang and N. Hu, Ion Transport in pH-Regulated Double-Barreled Nanopores, *Anal. Chem.*, 2022, **94**, 5642–5650.
61 X. Zhang, D. Luo, Y.-W. Zheng, X.-Q. Li, J. Song, W.-W. Zhao, *et al.*, Translocation of Specific DNA Nanocarrier through an Ultrasmall Nanopipette: Toward Single-Protein-Molecule Detection with Superior Signal-to-Noise Ratio, *ACS Nano*, 2022, **16**, 15108–15114.
62 X. Zhang, Y. Liu, M. Xu, Z. Zhang, W. Xie, S. He, *et al.*, Ultrahigh Spatial Resolution Cross-Disjoint Mortise-Confined Solid-State Nanopores with an Ultrathin Middle Layer, *J. Phys. Chem. C*, 2022, **126**, 8158–8164.
63 M. Zhang, Z. D. Harms, T. Greibe, C. A. Starr, A. Zlotnick and S. C. Jacobson, In-Plane, In-Series Nanopores with Circular Cross Sections for Resistive-Pulse Sensing, *ACS Nano*, 2022, **16**, 7352–7360.
64 C. Dekker, Solid-State Nanopores, *Nat. Nanotechnol.*, 2007, **2**, 209–215.
65 A. Pal and M. M. Varma, Nanopore Translocation Measurement Methods: A Review, *IEEE Sens. J.*, 2022, **22**, 14686–14695.
66 L. Xue, H. Yamazaki, R. Ren, M. Wanunu, A. P. Ivanov and J. B. Edel, Solid-State Nanopore Sensors, *Nat. Rev. Mater.*, 2020, **5**, 931–951.
67 E. A. Manrao, I. M. Derrington, A. H. Laszlo, K. W. Langford, M. K. Hopper, N. Gillgren, *et al.*, Reading DNA at Single-Nucleotide Resolution with a Mutant MspA Nanopore and phi29 DNA Polymerase, *Nat. Biotechnol.*, 2012, **30**, 349–353.
68 G. M. Cherf, K. R. Lieberman, H. Rashid, C. E. Lam, K. Karplus and M. Akeson, Automated Forward and Reverse Ratcheting of DNA in a Nanopore at 5 Å Precision, *Nat. Biotechnol.*, 2012, **30**, 344–348.
69 S. Howorka, S. Cheley and H. Bayley, Sequence-Specific Detection of Individual DNA Strands Using Engineered Nanopores, *Nat. Biotechnol.*, 2001, **19**, 636–639.
70 S. Su, X. Guo, Y. Fu, Y. Xie, X. Wang and J. Xue, Origin of Nonequilibrium 1/f Noise in Solid-State Nanopores, *Nanoscale*, 2020, **12**, 8975–8981.
71 C. Hsu, C.-Y. Lin, A. Alizadeh, H. Daiguji and W.-L. Hsu, Investigation of Entrance Effects on Particle Electrophoretic Behavior Near a Nanopore for Resistive Pulse Sensing, *Electrophoresis*, 2021, **42**, 2206–2214.
72 S. Kishimoto, S. Murayama, M. Tsutsui and M. Taniguchi, Crucial Role of Out-of-Pore Resistance on Temporal Response of Ionic Current in Nanopore Sensors, *ACS Sens.*, 2020, **5**, 1597–1603.
73 Z. Gu, Z. He, F. Chen, L. Meng, J. Feng and R. Zhou, Ionic Liquid Decelerates Single-Stranded DNA Transport through Molybdenum Disulfide Nanopores, *ACS Appl. Mater. Interfaces*, 2022, **14**, 32618–32624.
74 A. Gupta, P. J. Zuk and H. A. Stone, Charging Dynamics of Overlapping Double Layers in a Cylindrical Nanopore, *Phys. Rev. Lett.*, 2020, **125**, 076001.
75 C. Gu, Z. Yu, X. Li, X. Zhu, C. Jin, Z. Cao, *et al.*, Experimental Study on Single Biomolecules Sensing using MoS_2-Graphene Heterostructure Nanopores, *Nanoscale*, 2022, **15**, 266–274.
76 R. Wang, T. Gilboa, J. Song, D. Huttner, M. W. Grinstaff and A. Meller, Single-Molecule Discrimination of Labeled DNAs and Polypeptides Using Photoluminescent-Free TiO_2 Nanopores, *ACS Nano*, 2018, **12**, 11648–11656.
77 A. Smolyanitsky, B. I. Yakobson, T. A. Wassenaar, E. Paulechka and K. Kroenlein, A MoS_2-Based Capacitive Displacement Sensor for DNA Sequencing, *ACS Nano*, 2016, **10**, 9009–9016.
78 T. Ohshiro, M. Konno, A. Asai, Y. Komoto, A. Yamagata, Y. Doki, *et al.*, Single-Molecule RNA Sequencing for Simultaneous Detection of m6A and 5mC, *Sci. Rep.*, 2021, **11**, 19304.

79 L. Tang, L. Yi, T. Jiang, R. Ren, B. P. Nadappuram, B. Zhang, *et al.*, Measuring Conductance Switching in Single Proteins Using Quantum Tunneling, *Sci. Adv.*, 2022, **8**, eabm8149.
80 L. Meng, J. Huang, Z. He and R. Zhou, Single Nucleobase Identification for Transversally-Confined ssDNA Using Longitudinal Ionic Currents, *Nanoscale*, 2022, **14**, 6922–6929.
81 I. Djurišić, M. S. Dražić, A. Ž. Tomović, M. Spasenović, Ž Šljivančanin, V. P. Jovanović, *et al.*, DNA Sequencing with Single-Stranded DNA Rectification in a Nanogap Gated by N-Terminated Carbon Nanotube Electrodes, *ACS Appl. Nano Mater.*, 2020, **3**, 3034–3043.
82 A. Voorspoels, J. Gevers, S. Santermans, N. Akkan, K. Martens, K. Willems, *et al.*, Design Principles of DNA-Barcodes for Nanopore-FET Readout, Based on Molecular Dynamics and TCAD Simulations, *J. Phys. Chem. A*, 2024, **128**, 3926–3933.
83 S. Schmid, P. Stömmer, H. Dietz and C. Dekker, Nanopore Electro-Osmotic Trap for the Label-Free Study of Single Proteins and Their Conformations, *Nat. Nanotechnol.*, 2021, **16**, 1244–1250.
84 N. Burck, T. Gilboa, A. Gadi, M. Patkin Nehrer, R. J. Schneider and A. Meller, Nanopore Identification of Single Nucleotide Mutations in Circulating Tumor DNA by Multiplexed Ligation, *Clin. Chem.*, 2021, **67**, 753–762.
85 Q. Li, Y.-L. Ying, S.-C. Liu, Y. Lin and Y.-T. Long, Detection of Single Proteins with a General Nanopore Sensor, *ACS Sens.*, 2019, **4**, 1185–1189.
86 A. Arima, M. Tsutsui, T. Washio, Y. Baba and T. Kawai, Solid-State Nanopore Platform Integrated with Machine Learning for Digital Diagnosis of Virus Infection, *Anal. Chem.*, 2021, **93**, 215–227.
87 K.-J. Hsu, L. F. Villalobos, S. Huang, H.-Y. Chi, M. Dakhchoune, W.-C. Lee, *et al.*, Multipulsed Millisecond Ozone Gasification for Predictable Tuning of Nucleation and Nucleation-Decoupled Nanopore Expansion in Graphene for Carbon Capture, *ACS Nano*, 2021, **15**, 13230–13239.
88 A. Karmi, H. Dachlika, G. P. Sakala, D. Rotem, M. Reches and D. Porath, Detection of Au Nanoparticles Using Peptide-Modified Si_3N_4 Nanopores, *ACS Appl. Nano Mater.*, 2021, **4**, 1000–1008.
89 X. F. van Kooten, Y. Rozevsky, Y. Marom, E. Ben Sadeh and A. Meller, Purely Electrical SARS-CoV-2 Sensing Based on Single-Molecule Counting, *Nanoscale*, 2022, **14**, 4977–4986.
90 E. B. Farrell, D. Duleba and R. P. Johnson, Aprotic Solvent Accumulation Amplifies Ion Current Rectification in Conical Nanopores, *J. Phys. Chem. B*, 2022, **126**, 5689–5694.
91 W. Si, Z. Zhu, G. Wu, Y. Zhang, Y. Chen and J. Sha, Encoding Manipulation of DNA-Nanoparticle Assembled Nanorobot Using Independently Charged Array Nanopores, *Small Methods*, 2022, **6**, 2200318.
92 P. Zhang, M. Xia, F. Zhuge, Y. Zhou, Z. Wang, B. Dong, *et al.*, Nanochannel-Based Transport in an Interfacial Memristor Can Emulate the Analog Weight Modulation of Synapses, *Nano Lett.*, 2019, **19**, 4279–4286.
93 P. Priya, T. C. Nguyen, A. Saxena and N. R. Aluru, Machine Learning Assisted Screening of Two-Dimensional Materials for Water Desalination, *ACS Nano*, 2022, **16**, 1929–1939.
94 J. Li, D. Stein, C. McMullan, D. Branton, M. J. Aziz and J. A. Golovchenko, Ion-Beam Sculpting at Nanometre Length Scales, *Nature*, 2001, **412**, 166–169.
95 J. Li, M. Gershow, D. Stein, E. Brandin and J. A. Golovchenko, DNA Molecules and Configurations in a Solid-State Nanopore Microscope, *Nat. Mater.*, 2003, **2**, 611–615.
96 M. Ayub, A. Ivanov, J. Hong, P. Kuhn, E. Instuli, J. B. Edel, *et al.*, Precise Electrochemical Fabrication of Sub-20 nm Solid-State Nanopores for Single-Molecule Biosensing, *J. Phys.: Condens. Matter*, 2010, **22**, 454128.
97 J. Sha, Z. Ni, L. Liu, H. Yi and Y. Chen, A Novel Method of Fabricating a Nanopore Based on a Glass Tube for Single-Molecule Detection, *Nanotechnology*, 2011, **22**, 175304.
98 I. Yanagi, R. Akahori and K.-i. Takeda, Stable Fabrication of a Large Nanopore by Controlled Dielectric Breakdown in a High-pH Solution for the Detection of Various-Sized Molecules, *Sci. Rep.*, 2019, **9**, 13143.
99 T. Gilboa, E. Zvuloni, A. Zrehen, A. H. Squires and A. Meller, Automated, Ultra-Fast Laser-Drilling of Nanometer Scale Pores and Nanopore Arrays in Aqueous Solutions, *Adv. Funct. Mater.*, 2020, **30**, 1900642.
100 S. Kishimoto, I. W. Leong, S. Murayama, T. Nakada, Y. Komoto, M. Tsutsui, *et al.*, 3D Designing of Resist Membrane Pores via Direct Electron Beam Lithography, *Sens. Actuators, B*, 2022, **357**, 131380.
101 J. J. Kasianowicz, E. Brandin, D. Branton and D. W. Deamer, Characterization of Individual Polynucleotide Molecules Using a Membrane Channel, *Proc. Natl. Acad. Sci. U. S. A.*, 1996, **93**, 13770–13773.
102 J. T. Benton and C. Bayly-Jones, Challenges and Approaches to Studying Pore-Forming Proteins, *Biochem. Soc. Trans.*, 2021, **49**, 2749–2765.
103 W. Li, Y. Wang, Y. Xiao, M. Li, Q. Liu, L. Liang, *et al.*, Simultaneous Dual-Site Identification of 5mC/8oG in DNA Triplex Using a Nanopore Sensor, *ACS Appl. Mater. Interfaces*, 2022, **14**, 32948–32959.
104 M. T. Noakes, H. Brinkerhoff, A. H. Laszlo, I. M. Derrington, K. W. Langford, J. W. Mount, *et al.*, Increasing the Accuracy of Nanopore DNA Sequencing Using a Time-Varying Cross Membrane Voltage, *Nat. Biotechnol.*, 2019, **37**, 651–656.
105 S. Benner, R. J. A. Chen, N. A. Wilson, R. Abu-Shumays, N. Hurt, K. R. Lieberman, *et al.*, Sequence-Specific Detection of Individual DNA Polymerase Complexes in Real Time Using a Nanopore, *Nat. Nanotechnol.*, 2007, **2**, 718–724.
106 H. Hong, J. Wei, X. Lei, H. Chen, P. M. Sarro, G. Zhang, *et al.*, Study on the Controllability of the Fabrication of Single-Crystal Silicon Nanopores/Nanoslits with a Fast-

Stop Ionic Current-Monitored TSWE Method, *Microsyst. Nanoeng.*, 2023, **9**, 63.
107 E. Zvuloni, A. Zrehen, T. Gilboa and A. Meller, Fast and Deterministic Fabrication of Sub-5 Nanometer Solid-State Pores by Feedback-Controlled Laser Processing, *ACS Nano*, 2021, **15**, 12189–12200.
108 I. Yanagi and K.-i. Takeda, Sub-10 nm-Thick SiN Nanopore Membranes Fabricated Using the SiO_2 Sacrificial Layer Process, *Nanotechnology*, 2021, **32**, 415301.
109 J. P. Fried, J. L. Swett, B. P. Nadappuram, J. A. Mol, J. B. Edel, A. P. Ivanov, *et al.*, In Situ Solid-State Nanopore Fabrication, *Chem. Soc. Rev.*, 2021, **50**, 4974–4992.
110 S. Hernández-Ainsa, K. Misiunas, V. V. Thacker, E. A. Hemmig and U. F. Keyser, Voltage-Dependent Properties of DNA Origami Nanopores, *Nano Lett.*, 2014, **14**, 1270–1274.
111 T. J. Liu and J.-P. Hsu, Electrokinetic Behavior of Conical Nanopores Functionalized with Two Polyelectrolyte Layers: Effect of pH Gradient, *Soft Matter*, 2022, **18**, 8427–8435.
112 H. Kaur, S. Nandivada, M. C. Acharjee, D. S. McNabb and J. Li, Estimating RNA Polymerase Protein Binding Sites on λ DNA Using Solid-State Nanopores, *ACS Sens.*, 2019, **4**, 100–109.
113 J. Zhou, A. Zlotnick and S. C. Jacobson, Disassembly of Single Virus Capsids Monitored in Real Time with Multicycle Resistive-Pulse Sensing, *Anal. Chem.*, 2022, **94**, 985–992.
114 J. Zhou, P. Kondylis, D. G. Haywood, Z. D. Harms, L. S. Lee, A. Zlotnick, *et al.*, Characterization of Virus Capsids and Their Assembly Intermediates by Multicycle Resistive-Pulse Sensing with Four Pores in Series, *Anal. Chem.*, 2018, **90**, 7267–7274.
115 N. Meyer, N. Arroyo, M. Baldelli, N. Coquart, J. M. Janot, V. Perrier, *et al.*, Conical Nanopores Highlight the Pro-aggregating Effects of Pyrimethanil Fungicide on Aβ(1–42) Peptides and Dimeric Splitting Phenomena, *Chemosphere*, 2022, **291**, 132733.
116 J. A. Rodriguez-Manzo, Z. J. Qi, M. Puster, A. Balan, A. T. Charlie Johnson and M. Drndic, Fabrication and Simultaneous Electrical Measurement of Graphene Nanoribbon Devices Inside a S/TEM, *Microsc. Microanal.*, 2015, **21**, 1155–1156.
117 S. R. Park, H. Peng and X. S. Ling, Fabrication of Nanopores in Silicon Chips Using Feedback Chemical Etching, *Small*, 2007, **3**, 116–119.
118 A. P. Ivanov, P. Actis, P. Jönsson, D. Klenerman, Y. Korchev and J. B. Edel, On-Demand Delivery of Single DNA Molecules Using Nanopipets, *ACS Nano*, 2015, **9**, 3587–3595.
119 J. Choi, C. C. Lee and S. Park, Scalable Fabrication of Sub-10 nm Polymer Nanopores for DNA Analysis, *Microsyst. Nanoeng.*, 2019, **5**, 12.
120 J. Wang, Y. Zhou and L. Jiang, Bio-inspired Track-Etched Polymeric Nanochannels: Steady-State Biosensors for Detection of Analytes, *ACS Nano*, 2021, **15**, 18974–19013.
121 N. Sakai and S. Matile, Synthetic Ion Channels, *Langmuir*, 2013, **29**, 9031–9040.
122 F. Liu, J. Zhao, X. Liu, X. Zhen, Q. Feng, Y. Gu, *et al.*, PEC-SERS Dual-Mode Detection of Foodborne Pathogens Based on Binding-Induced DNA Walker and C_3N_4/MXene-Au NPs Accelerator, *Anal. Chem.*, 2023, **95**, 14297–14307.
123 Q. Guan and Y. Cai, Nanopore Rigidity as an Atomic Descriptor of Ion-Transfer Kinetics in Sieving Membranes: Insights from Two-Dimensional g-C_3N_4, *Mater. Today Nano*, 2024, **25**, 100437.
124 G. Tai, T. Hu, Y. Zhou, X. Wang, J. Kong, T. Zeng, *et al.*, Synthesis of Atomically Thin Boron Films on Copper Foils, *Angew. Chem., Int. Ed.*, 2015, **54**, 15473–15477.
125 C. Lee, L. Joly, A. Siria, A.-L. Biance, R. Fulcrand and L. Bocquet, Large Apparent Electric Size of Solid-State Nanopores Due to Spatially Extended Surface Conduction, *Nano Lett.*, 2012, **12**, 4037–4044.
126 J. Feng, K. Liu, R. D. Bulushev, S. Khlybov, D. Dumcenco, A. Kis, *et al.*, Identification of Single Nucleotides in MoS_2 Nanopores, *Nat. Nanotechnol.*, 2015, **10**, 1070–1076.
127 Y. Wu and J. J. Gooding, The Application of Single Molecule Nanopore Sensing for Quantitative Analysis, *Chem. Soc. Rev.*, 2022, **51**, 3862–3885.
128 J. Larkin, R. Henley, D. C. Bell, T. Cohen-Karni, J. K. Rosenstein and M. Wanunu, Slow DNA Transport through Nanopores in Hafnium Oxide Membranes, *ACS Nano*, 2013, **7**, 10121–10128.
129 J. Larkin, R. Y. Henley, M. Muthukumar, J. K. Rosenstein and M. Wanunu, High-Bandwidth Protein Analysis Using Solid-State Nanopores, *Biophys. J.*, 2014, **106**, 696–704.
130 S. Carson, S. T. Wick, P. A. Carr, M. Wanunu and C. A. Aguilar, Direct Analysis of Gene Synthesis Reactions Using Solid-State Nanopores, *ACS Nano*, 2015, **9**, 12417–12424.
131 H. Yamazaki, R. Hu, R. Y. Henley, J. Halman, K. A. Afonin, D. Yu, *et al.*, Label-Free Single-Molecule Thermoscopy Using a Laser-Heated Nanopore, *Nano Lett.*, 2017, **17**, 7067–7074.
132 L. Cantley, J. L. Swett, D. Lloyd, D. A. Cullen, K. Zhou, P. V. Bedworth, *et al.*, Voltage Gated Inter-Cation Selective Ion Channels from Graphene Nanopores, *Nanoscale*, 2019, **11**, 9856–9861.
133 Y. Qiu, Z. S. Siwy and M. Wanunu, Abnormal Ionic-Current Rectification Caused by Reversed Electroosmotic Flow under Viscosity Gradients across Thin Nanopores, *Anal. Chem.*, 2019, **91**, 996–1004.
134 S. R. German, T. S. Hurd, H. S. White and T. L. Mega, Sizing Individual Au Nanoparticles in Solution with Sub-Nanometer Resolution, *ACS Nano*, 2015, **9**, 7186–7194.
135 M. Krems, Y. V. Pershin and M. Di Ventra, Ionic Memcapacitive Effects in Nanopores, *Nano Lett.*, 2010, **10**, 2674–2678.
136 R. Yazbeck, Y. Xu, T. Porter and C. Duan, Nanoparticle-Blockage-Enabled Rapid and Reversible Nanopore Gating with Tunable Memory, *Proc. Natl. Acad. Sci. U. S. A.*, 2022, **119**, e2200845119.

137 S. Huang, M. Dakhchoune, W. Luo, E. Oveisi, G. He, M. Rezaei, *et al.*, Single-Layer Graphene Membranes by Crack-Free Transfer for Gas Mixture Separation, *Nat. Commun.*, 2018, **9**, 2632.

138 B. B. Sharma and A. Govind Rajan, How Grain Boundaries and Interfacial Electrostatic Interactions Modulate Water Desalination via Nanoporous Hexagonal Boron Nitride, *J. Phys. Chem. B*, 2022, **126**, 1284–1300.

139 K. Chen, J. Zhu, F. Bošković and U. F. Keyser, Nanopore-Based DNA Hard Drives for Rewritable and Secure Data Storage, *Nano Lett.*, 2020, **20**, 3754–3760.

140 T. Zhou, X. He, J. Zhao, L. Shi and L. Wen, Electrokinetic Transport of Nanoparticles in Functional Group Modified Nanopores, *Chin. Chem. Lett.*, 2022, **34**, 107667.

141 F. A. L. de Souza, R. G. Amorim, W. L. Scopel and R. H. Scheicher, Controlled Current Confinement in Interfaced 2D Nanosensor for Electrical Identification of DNA, *Phys. Chem. Chem. Phys.*, 2019, **21**, 24884–24890.

142 D. Garoli, H. Yamazaki, N. Maccaferri and M. Wanunu, Plasmonic Nanopores for Single-Molecule Detection and Manipulation: Toward Sequencing Applications, *Nano Lett.*, 2019, **19**, 7553–7562.

143 X. Shi, A.-K. Pumm, C. Maffeo, F. Kohler, E. Feigl, W. Zhao, *et al.*, A DNA Turbine Powered by a Transmembrane Potential Across a Nanopore, *Nat. Nanotechnol.*, 2023, **19**, 338–344.

144 J. Feng, M. Graf, K. Liu, D. Ovchinnikov, D. Dumcenco, M. Heiranian, *et al.*, Single-Layer MoS_2 Nanopores as Nanopower Generators, *Nature*, 2016, **536**, 197–200.

145 S.-W. Nam, M. J. Rooks, K.-B. Kim and S. M. Rossnagel, Ionic Field Effect Transistors with Sub-10 nm Multiple Nanopores, *Nano Lett.*, 2009, **9**, 2044–2048.

146 T. Xiong, C. Li, X. He, B. Xie, J. Zong, Y. Jiang, *et al.*, Neuromorphic Functions with a Polyelectrolyte-Confined Fluidic Memristor, *Science*, 2023, **379**, 156–161.

147 M. Wood and B. Zhang, Bipolar Electrochemical Method for Dynamic In Situ Control of Single Metal Nanowire Growth, *ACS Nano*, 2015, **9**, 2454–2464.

148 T. Ma, J.-M. Janot and S. Balme, Track-Etched Nanopore/Membrane: From Fundamental to Applications, *Small Methods*, 2020, **4**, 2000366.

149 M. Waugh, K. Briggs, D. Gunn, M. Gibeault, S. King, Q. Ingram, *et al.*, Solid-State Nanopore Fabrication by Automated Controlled Breakdown, *Nat. Protoc.*, 2020, **15**, 122–143.

150 P. Waduge, I. Bilgin, J. Larkin, R. Y. Henley, K. Goodfellow, A. C. Graham, *et al.*, Direct and Scalable Deposition of Atomically Thin Low-Noise MoS_2 Membranes on Apertures, *ACS Nano*, 2015, **9**, 7352–7359.

151 S. Zeng, C. Wen, P. Solomon, S.-L. Zhang and Z. Zhang, Rectification of Protein Translocation in Truncated Pyramidal Nanopores, *Nat. Nanotechnol.*, 2019, **14**, 1056–1062.

152 A. T. Kuan and J. A. Golovchenko, Nanometer-Thin Solid-State Nanopores by Cold Ion Beam Sculpting, *Appl. Phys. Lett.*, 2012, **100**, 213104.

153 J. Bai, D. Wang, S.-w. Nam, H. Peng, R. Bruce, L. Gignac, *et al.*, Fabrication of Sub-20 nm Nanopore Arrays in Membranes with Embedded Metal Electrodes at Wafer Scales, *Nanoscale*, 2014, **6**, 8900–8906.

154 L. Xue, P. Cadinu, B. Paulose Nadappuram, M. Kang, Y. Ma, Y. Korchev, *et al.*, Gated Single-Molecule Transport in Double-Barreled Nanopores, *ACS Appl. Mater. Interfaces*, 2018, **10**, 38621–38629.

155 P. Apel, A. Schulz, R. Spohr, C. Trautmann and V. Vutsadakis, Track Size and Track Structure in Polymer Irradiated by Heavy Ions, *Nucl. Instrum. Methods Phys. Res., Sect. B*, 1998, **146**, 468–474.

156 A. J. Storm, J. H. Chen, H. W. Zandbergen and C. Dekker, Translocation of Double-Strand DNA Through a Silicon Oxide Nanopore, *Phys. Rev. E: Stat., Nonlinear, Soft Matter Phys.*, 2005, **71**, 051903.

157 M. Karhanek, J. T. Kemp, N. Pourmand, R. W. Davis and C. D. Webb, Single DNA Molecule Detection Using Nanopipettes and Nanoparticles, *Nano Lett.*, 2005, **5**, 403–407.

158 A. Han, G. Schürmann, G. Mondin, R. A. Bitterli, N. G. Hegelbach, N. F. d. Rooij, *et al.*, Sensing Protein Molecules Using Nanofabricated Pores, *Appl. Phys. Lett.*, 2006, **88**, 093901.

159 J. P. Fried, J. L. Swett, B. P. Nadappuram, A. Fedosyuk, A. Gee, O. E. Dyck, *et al.*, Localised Solid-State Nanopore Fabrication via Controlled Breakdown using On-Chip Electrodes, *Nano Res.*, 2022, **15**, 9881–9889.

160 J.-S. Yu, M.-C. Lim, D. T. N. Huynh, H.-J. Kim, H.-M. Kim, Y.-R. Kim, *et al.*, Identifying the Location of a Single Protein along the DNA Strand Using Solid-State Nanopores, *ACS Nano*, 2015, **9**, 5289–5298.

161 Y. M. N. D. Y. Bandara, B. I. Karawdeniya and J. R. Dwyer, Real-Time Profiling of Solid-State Nanopores During Solution-Phase Nanofabrication, *ACS Appl. Mater. Interfaces*, 2016, **8**, 30583–30589.

162 T. Gilboa, A. Zrehen, A. Girsault and A. Meller, Optically-Monitored Nanopore Fabrication Using a Focused Laser Beam, *Sci. Rep.*, 2018, **8**, 9765.

163 P. Xie, Q. Xiong, Y. Fang, Q. Qing and C. M. Lieber, Local Electrical Potential Detection of DNA by Nanowire–Nanopore Sensors, *Nat. Nanotechnol.*, 2012, **7**, 119–125.

164 M. Graf, M. Lihter, D. Altus, S. Marion and A. Radenovic, Transverse Detection of DNA Using a MoS(2) Nanopore, *Nano Lett.*, 2019, **19**, 9075–9083.

165 S. Garaj, W. Hubbard, A. Reina, J. Kong, D. Branton and J. A. Golovchenko, Graphene as a Subnanometre Trans-Electrode Membrane, *Nature*, 2010, **467**, 190–193.

166 B. McNally, A. Singer, Z. Yu, Y. Sun, Z. Weng and A. Meller, Optical Recognition of Converted DNA Nucleotides for Single-Molecule DNA Sequencing Using Nanopore Arrays, *Nano Lett.*, 2010, **10**, 2237–2244.

167 A. Demuro and I. Parker, "Optical Patch-clamping": Single-channel Recording by Imaging Ca^{2+} Flux through Individual Muscle Acetylcholine Receptor Channels, *J. Gen. Physiol.*, 2005, **126**, 179–192.

168 B. N. Anderson, O. N. Assad, T. Gilboa, A. H. Squires, D. Bar and A. Meller, Probing Solid-State Nanopores with Light for the Detection of Unlabeled Analytes, *ACS Nano*, 2014, **8**, 11836–11845.

169 M. Zwolak and M. Di Ventra, Electronic Signature of DNA Nucleotides via Transverse Transport, *Nano Lett.*, 2005, **5**, 421–424.

170 Y.-C. Chen and M. D. Ventra, Shot Noise in Nanoscale Conductors from First Principles, *Phys. Rev. B: Condens. Matter Mater. Phys.*, 2003, **67**, 153304.

171 J. Lagerqvist, M. Zwolak and M. D. Ventra, Fast DNA Sequencing via Transverse Electronic Transport, *Nano Lett.*, 2006, **6**, 779–782.

172 M. Tsutsui, M. Taniguchi, K. Yokota and T. Kawai, Identifying Single Nucleotides by Tunnelling Current, *Nat. Nanotechnol.*, 2010, **5**, 286–290.

173 S. J. Heerema and C. Dekker, Graphene Nanodevices for DNA Sequencing, *Nat. Nanotechnol.*, 2016, **11**, 127–136.

174 R. G. Amorim, A. R. Rocha and R. H. Scheicher, Boosting DNA Recognition Sensitivity of Graphene Nanogaps through Nitrogen Edge Functionalization, *J. Phys. Chem. C*, 2016, **120**, 19384–19388.

175 H. W. C. Postma, Rapid Sequencing of Individual DNA Molecules in Graphene Nanogaps, *Nano Lett.*, 2010, **10**, 420–425.

176 R. L. Kumawat and B. Pathak, Identifying Single-Stranded DNA by Tuning the Graphene Nanogap Size: An Ionic Current Approach, *J. Phys. Chem. B*, 2022, **126**, 1178–1187.

177 A. Fanget, F. Traversi, S. Khlybov, P. Granjon, A. Magrez, L. Forró, *et al.*, Nanopore Integrated Nanogaps for DNA Detection, *Nano Lett.*, 2014, **14**, 244–249.

178 A. P. Ivanov, E. Instuli, C. M. McGilvery, G. Baldwin, D. W. McComb, T. Albrecht, *et al.*, DNA Tunneling Detector Embedded in a Nanopore, *Nano Lett.*, 2011, **11**, 279–285.

179 C. A. Merchant, K. Healy, M. Wanunu, V. Ray, N. Peterman, J. Bartel, *et al.*, DNA Translocation through Graphene Nanopores, *Nano Lett.*, 2010, **10**, 2915–2921.

180 T. Nelson, B. Zhang and O. V. Prezhdo, Detection of Nucleic Acids with Graphene Nanopores: Ab Initio Characterization of a Novel Sequencing Device, *Nano Lett.*, 2010, **10**, 3237–3242.

181 K. K. Saha, M. Drndić and B. K. Nikolić, DNA Base-Specific Modulation of Microampere Transverse Edge Currents through a Metallic Graphene Nanoribbon with a Nanopore, *Nano Lett.*, 2012, **12**, 50–55.

182 T. Ahmed, J. T. Haraldsen, J. J. Rehr, M. D. Ventra, I. Schuller and A. V. Balatsky, Correlation Dynamics and Enhanced Signals for the Identification of Serial Biomolecules and DNA Bases, *Nanotechnology*, 2014, **25**, 125705.

183 T. Ahmed, J. T. Haraldsen, J.-X. Zhu and A. V. Balatsky, Next-Generation Epigenetic Detection Technique: Identifying Methylated Cytosine Using Graphene Nanopore, *J. Phys. Chem. Lett.*, 2014, **5**, 2601–2607.

184 A. Wasfi, F. Awwad and M. Atef, DNA Bases Detection via MoS_2 Field Effect Transistor with a Nanopore: First-Principles Modeling, *Analog Integr. Circuits Signal Process.*, 2023, **114**, 253–264.

185 R. Chakraborty, M. Xiong, N. Athreya, S. K. Tabatabaei, O. Milenkovic and J.-P. Leburton, Solid-State MoS_2 Nanopore Membranes for Discriminating among the Lengths of RNA Tails on a Double-Stranded DNA: A New Simulation-Based Differentiating Algorithm, *ACS Appl. Nano Mater.*, 2023, **6**, 4651–4660.

186 A. B. Farimani, K. Min and N. R. Aluru, DNA Base Detection Using a Single-Layer MoS_2, *ACS Nano*, 2014, **8**, 7914–7922.

187 J. Prasongkit, S. Jungthawan, R. G. Amorim and R. H. Scheicher, Single-Molecule DNA Sequencing Using Two-Dimensional $Ti_2C(OH)_2$ MXene Nanopores: A First-Principles Investigation, *Nano Res.*, 2022, **15**, 9843–9849.

188 S. J. Heerema, L. Vicarelli, S. Pud, R. N. Schouten, H. W. Zandbergen and C. Dekker, Probing DNA Translocations with Inplane Current Signals in a Graphene Nanoribbon with a Nanopore, *ACS Nano*, 2018, **12**, 2623–2633.

189 L. Mu, Y. Chang, S. D. Sawtelle, M. Wipf, X. Duan and M. A. Reed, Silicon Nanowire Field-Effect Transistors—A Versatile Class of Potentiometric Nanobiosensors, *IEEE Access*, 2015, **3**, 287–302.

190 I. Yanagi, T. Oura, T. Haga, M. Ando, J. Yamamoto, T. Mine, *et al.*, Side-Gated Ultrathin-Channel Nanopore FET Sensors, *Nanotechnology*, 2016, **27**, 115501.

191 N. B. M. Athreya, A. Sarathy and J.-P. Leburton, Large Scale Parallel DNA Detection by Two-Dimensional Solid-State Multipore Systems, *ACS Sens.*, 2018, **3**, 1032–1039.

192 F.-P. Ouyang, S.-L. Peng, H. Zhang, L.-B. Weng and H. Xu, A Biosensor Based on Graphene Nanoribbon with Nanopores: A First-Principles Devices-Design, *Chin. Phys. B*, 2011, **20**, 058504.

193 S. M. Avdoshenko, D. Nozaki, C. Gomes da Rocha, J. W. González, M. H. Lee, R. Gutierrez, *et al.*, Dynamic and Electronic Transport Properties of DNA Translocation through Graphene Nanopores, *Nano Lett.*, 2013, **13**, 1969–1976.

194 A. Girdhar, C. Sathe, K. Schulten and J. P. Leburton, Graphene Quantum Point Contact Transistor for DNA Sensing, *Proc. Natl. Acad. Sci. U. S. A.*, 2013, **110**, 16748–16753.

195 N. B. M. Athreya, M. Xiong, R. Chakraborty, H. T. Crawford-Eng and J.-P. Leburton, Molecular Dynamics and Electrical Modeling of Multi-Layered Nanopores of MoS_2 and Hexagonal Boron Nitride for Biosensing of DNA, *ACS Appl. Nano Mater.*, 2023, **6**, 4406–4416.

196 M. B. Henry, M. Tumbapo and B. O. Tayo, Identification of DNA Bases Using Nanopores Created in Finite-Size Nanoribbons from Graphene, Phosphorene, and Silicene, *AIP Adv.*, 2021, **11**, 035324.

197 A. Sarathy and J.-P. Leburton, Electronic Conductance Model in Constricted MoS_2 with Nanopores, *Appl. Phys. Lett.*, 2016, **108**, 053701.

198 C. Hou, G. Tai, J. Hao, L. Sheng, B. Liu and Z. Wu, Ultrastable Crystalline Semiconducting Hydrogenated Borophene, *Angew. Chem., Int. Ed.*, 2020, **59**, 10819–10825.

199 C. Hou, G. Tai, Y. Liu, R. Liu, X. Liang, Z. Wu, *et al.*, Borophene Pressure Sensing for Electronic Skin and Human-Machine Interface, *Nano Energy*, 2022, **97**, 107189.
200 C. Hou, G. Tai, Y. Liu and X. Liu, Borophene Gas Sensor, *Nano Res.*, 2022, **15**, 2537–2544.
201 C. Hou, G. Tai, Y. Liu, Z. Wu, X. Liang and X. Liu, Borophene-based Materials for Energy, Sensors and Information Storage Applications, *Nano Res. Energy*, 2023, **2**, e9120051.
202 A. Wang, C. Wang, L. Fu, W. Wong-Ng and Y. Lan, Recent Advances of Graphitic Carbon Nitride-Based Structures and Applications in Catalyst, Sensing, Imaging, and LEDs, *Nano-Micro Lett.*, 2017, **9**, 47.
203 F. Traversi, C. Raillon, S. M. Benameur, K. Liu, S. Khlybov, M. Tosun, *et al.*, Detecting the Translocation of DNA Through a Nanopore Using Graphene Nanoribbons, *Nat. Nanotechnol.*, 2013, **8**, 939–945.
204 R. M. M. Smeets, N. H. Dekker and C. Dekker, Low-Frequency Noise in Solid-State Nanopores, *Nanotechnology*, 2009, **20**, 095501.
205 C. C. Harrell, Y. Choi, L. P. Horne, L. A. Baker, Z. S. Siwy and C. R. Martin, Resistive-Pulse DNA Detection with a Conical Nanopore Sensor, *Langmuir*, 2006, **22**, 10837–10843.
206 M. Puster, J. A. Rodríguez-Manzo, A. Balan and M. Drndić, Toward Sensitive Graphene Nanoribbon–Nanopore Devices by Preventing Electron Beam-Induced Damage, *ACS Nano*, 2013, **7**, 11283–11289.
207 M. Puster, A. Balan, J. A. Rodríguez-Manzo, G. Danda, J.-H. Ahn, W. Parkin, *et al.*, Cross-Talk Between Ionic and Nanoribbon Current Signals in Graphene Nanoribbon-Nanopore Sensors for Single-Molecule Detection, *Small*, 2015, **11**, 6309–6316.
208 F. Schwierz, Graphene Transistors, *Nat. Nanotechnol.*, 2010, **5**, 487–496.
209 M. Neklyudova, A. K. Erdamar, L. Vicarelli, S. J. Heerema, T. Rehfeldt, G. Pandraud, *et al.*, Through-Membrane Electron-Beam Lithography for Ultrathin Membrane Applications, *Appl. Phys. Lett.*, 2017, **111**, 063105.
210 J. A. Rodríguez-Manzo, Z. J. Qi, A. Crook, J.-H. Ahn, A. T. C. Johnson and M. Drndić, In Situ Transmission Electron Microscopy Modulation of Transport in Graphene Nanoribbons, *ACS Nano*, 2016, **10**, 4004–4010.
211 A. Sarathy, H. Qiu and J.-P. Leburton, Graphene Nanopores for Electronic Recognition of DNA Methylation, *J. Phys. Chem. B*, 2017, **121**, 3757–3763.
212 H. Qiu, A. Sarathy, J.-P. Leburton and K. Schulten, Intrinsic Stepwise Translocation of Stretched ssDNA in Graphene Nanopores, *Nano Lett.*, 2015, **15**, 8322–8330.
213 F. Al-Dirini, M. A. Mohammed, M. S. Hossain, F. M. Hossain, A. Nirmalathas and E. Skafidas, Tuneable Graphene Nanopores for Single Biomolecule Detection, *Nanoscale*, 2016, **8**, 10066–10077.
214 H. Arjmandi-Tash, L. A. Belyaeva and G. F. Schneider, Single Molecule Detection with Graphene and Other Two-Dimensional Materials: Nanopores and Beyond, *Chem. Soc. Rev.*, 2016, **45**, 476–493.
215 E. Paulechka, T. A. Wassenaar, K. Kroenlein, A. Kazakov and A. Smolyanitsky, Nucleobase-Functionalized Graphene Nanoribbons for Accurate High-Speed DNA Sequencing, *Nanoscale*, 2016, **8**, 1861–1867.
216 G. Danda, P. Masih Das, Y.-C. Chou, J. T. Mlack, W. M. Parkin, C. H. Naylor, *et al.*, Monolayer WS_2 Nanopores for DNA Translocation with Light-Adjustable Sizes, *ACS Nano*, 2017, **11**, 1937–1945.
217 W. M. Parkin and M. Drndić, Signal and Noise in FET-Nanopore Devices, *ACS Sens.*, 2018, **3**, 313–319.
218 M. K. Jena, R. L. Kumawat and B. Pathak, First-Principles Density Functional Theory Study on Graphene and Borophene Nanopores for Individual Identification of DNA Nucleotides, *ACS Appl. Nano Mater.*, 2021, **4**, 13573–13586.
219 L. Tan, C. Nie, Z. Ao, H. Sun, T. An and S. Wang, Novel Two-dimensional Crystalline Carbon Nitrides Beyond g-C_3N_4: Structure and Applications, *J. Mater. Chem. A*, 2021, **9**, 17–33.
220 J. Lagerqvist, M. Zwolak and M. D. Ventra, Influence of the Environment and Probes on Rapid DNA Sequencing via Transverse Electronic Transport, *Biophys. J.*, 2007, **93**, 2384–2390.
221 H. Qiu, A. Girdhar, K. Schulten and J.-P. Leburton, Electrically Tunable Quenching of DNA Fluctuations in Biased Solid-State Nanopores, *ACS Nano*, 2016, **10**, 4482–4488.
222 H. Sadeghi, L. Algaragholy, T. Pope, S. Bailey, D. Visontai, D. Manrique, *et al.*, Graphene Sculpturene Nanopores for DNA Nucleobase Sensing, *J. Phys. Chem. B*, 2014, **118**, 6908–6914.
223 S. Shekar, D. J. Niedzwiecki, C.-C. Chien, P. Ong, D. A. Fleischer, J. Lin, *et al.*, Measurement of DNA Translocation Dynamics in a Solid-State Nanopore at 100 ns Temporal Resolution, *Nano Lett.*, 2016, **16**, 4483–4489.
224 S. Magierowski, Y. Huang, C. Wang and E. Ghafar-Zadeh, Nanopore-CMOS Interfaces for DNA Sequencing, *Biosensors*, 2016, **6**, 42.
225 A. Girdhar, C. Sathe, K. Schulten and J.-P. Leburton, Gate-Modulated Graphene Quantum Point Contact Device for DNA Sensing, *J. Comput. Electron.*, 2014, **13**, 839–846.